RESTORATION OF SCENE INFORMATION REFLECTED FROM NON-SPECULAR MEDIA

DISSERTATION

Mark G. Hoelscher, Lieutenant Colonel, USAF

AFIT/DS/ENP/11-M03

DEPARTMENT OF THE AIR FORCE
AIR UNIVERSITY

AIR FORCE INSTITUTE OF TECHNOLOGY

Wright-Patterson Air Force Base, Ohio

RESTORATION OF SCENE INFORMATION REFLECTED FROM
NON-SPECULAR MEDIA

DISSERTATION

Presented to the Faculty

Graduate School of Engineering and Management

Air Force Institute of Technology

Air University

Air Education and Training Command

In Partial Fulfillment of the Requirements for the

Degree of Doctor of Philosophy
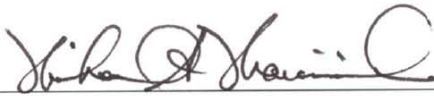

Mark G. Hoelscher, BS, MS

Lieutenant Colonel, USAF

March 2011

RESTORATION OF SCENE INFORMATION REFLECTED FROM
NON-SPECULAR MEDIA

Mark G. Hoelscher, BS, MS
Lieutenant Colonel, USAF

Approved:

_____   8 Mar 11
Michael A. Marciniak, PhD (Chairman)   Date

_____   8 Mar 11
David E. Weeks, PhD (Member)   Date

_____   8 Mar 11
Mark E. Oxley, PhD (Member)   Date

Accepted:

_____   10 Mar 11
M. U. Thomas   Date
Dean, Graduate School of Engineering
  and Management

AFIT/DS/ENP/11-M03

Abstract

A recently published experiment called "dual photography" exploits Helmholtz reciprocity by illuminating a scene with a pixilated light source and imaging other parts of that scene with a camera so that light transport between every pair of source-to-camera pixels is measured. The positions of the source and camera are then computationally interchanged to generate a "dual image" of the scene from the viewpoint of the source illuminated from the position of the camera. Although information from parts of the scene normally hidden from the camera are made available, this technique is rather contrived and therefore limited in practical applications since it requires access to the path from the source to the scene for the pixilated illumination.

By radiometrically modeling the experiment described above and expanding it to the concept of *indirect photography*, it has been shown theoretically, by simulation and through experimentation that information in parts of the scene not directly visible to either the camera or the controlling light source can be recovered. To that end, the camera and light source (now a laser) have been collocated. The laser is reflected from a visible surface in the scene onto hidden surfaces in the scene and the camera images collect how the light is reflected from the hidden surfaces back to the visible surface. The camera images are then used to reconstruct the information from the hidden surfaces in the scene. This document discusses the theory of indirect photography, describes the simulation and experiment and used to verify the theory and describes techniques used to improve the image quality, as measured by modified modulation transfer function.

To my wife and daughter

Acknowledgments

I would like to express my sincerest appreciation to my faculty advisor, Dr. Michael Marciniak, for his guidance and support throughout the course of my research. I would also like to thank Dr. David Weeks and Dr. Mark Oxley for their patience and support over the past several years. Reflection measurements made by Dr. Stephen Nauyoks and Mr. Michael Benson on the materials used in the experimental phase of this research were instrumental in verifying the assumptions of the mathematical models. Additionally, Mr. Mike Ranft and Mr. Greg Smith were indispensable during the experimental phase of this research for their technical and laboratory support, without their help, I would not have been able to finish.

Mark. G. Hoelscher

Table of Contents

List of Figures

xi

Figure | Page

List of Tables

Table 1. List of Acronyms

Acronym	Description
AFIT	Air Force Institute of Technology
AU	Air University
BRDF	Bi-directional Reflectance Distribution Function
CASI	Complete Angle Scatter Instrument
LR	Lucy-Richardson deconvolution
LSI	Linear Shift Invariant
MTF	Modulation Transfer Function
OTF	Optical Transfer Function
PSF	Point Spread Function
PTF	Phase Transfer Function
USAF	United States Air Force

Table 2. List of Symbols

Symbol	Description	Units
Q_e	Energy	J
Φ_e	Flux	W
L_e	Radiance	W cm^{-2} sr^{-1}
I_e	Intensity	W sr^{-1}
M_e	Exitance	W cm^{-2}
E_e	Irradiance	W cm^{-2}
f	BRDF	sr^{-1}
$\mathbf{G}$	Glint Vector	
Θ	Glint angle	rad
θ_i	Incident elevation angle	rad
θ_r	Reflected elevation angle	rad
$\Delta\phi$	Differential azimuthal angle	rad
$\mathbb{M}$	Modulation transfer function	n/a
$\mathbb{T}$	Dual Photography transport matrix	n/a
E_{xxx}	Irradiance on xxx	W cm^{-2}
L_{xxx}	Radiance of xxx	W cm^{-2} sr^{-1}
f_{xxx}	BRDF of xxx	sr^{-1}
ρ	Object reflectance	
f_{ph}	Object phase function	
θ_{xxx}	Incident elevation angle onto xxx	rad
ϕ_{xxx}	Incident azimuthal angle onto xxx	rad
θ'_{xxx}	Reflected elevation angle from xxx	rad
ϕ'_{xxx}	Reflected azimuthal angle from xxx	rad
Ω_{xxx}	Incident solid angel onto xxx	sr
Ω'_{xxx}	Reflected solid angel from xxx	sr
Φ_{pix_i}	flux incident on the ith pixel of the camera	
$\bar{w}$	2D wall reflector position	
$\bar{x}$	2D fixed object frame of reference position	
$\bar{x}'$	2D object reflector position	
$\bar{y}$	2D imaged reflector position	
$\bar{z}$	2D imaging system position	
α	Geometry terms from the fixed object frame of reference to the imaged reflector	
β	Geometry terms from the imaged reflector to the lens of the imaging system	
γ	Geometry terms from the wall reflector to the fixed object frame of reference	
$\odot$	Matrix Hadamard product	
$\otimes$	Matrix Kronecker product	

RESTORATION OF SCENE INFORMATION REFLECTED FROM

NON-SPECULAR MEDIA

I. Introduction

A photographic technique known as *dual photography*, which exploits Helmholtz reciprocity, allows for the position of a digital camera and a digital light source to be mathematically interchanged. This mathematical interchange was originally developed to aide in the rendering of computer generated scenes and enables the scene to be "viewed" from the position of the original light source as though "illuminated" from the position of the original camera. In the original work describing dual photography, the authors' main example of their work was to "show how dual photography can be used to capture and relight scenes." (Sen, et al., 2005). Subsequent work by the authors which include *Compressive Dual Photography* concentrate on the creation of adaptive and non-adaptive algorithms to more efficiently capture the large amounts of data necessary to build the light transport matrices required for the technique to work. (Sen & Shheil, 2009). Because the original goal of dual photography was the rendering and relighting of computer generated scenes, no attempt was made to recover details from the scene not directly visible to either the camera or the digitized light source. Additionally, no work has been done describing the quality of the dual image. Neither of these oversights effected the exploitation of dual photography for the authors' original intended purposes. Nevertheless, for applications outside the computer graphics community, the recovery of

1

scene information not directly visible to either the camera or the light source and a metric of the quality of the dual image are of considerable interest.

In one of the experiments from the original dual photography paper, a playing card was positioned such that the face of the playing card was not visible to the camera (Sen, et al., 2005). A pixilated light source was placed with a full view of the face of the playing card and a book was placed so that when a pixel illuminated the playing card, reflections from the card could be imaged by the camera after a intermediary reflection from the book (see Figure 1).
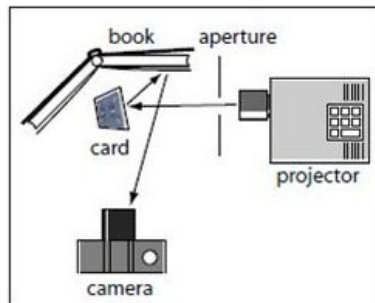
Figure 1. Original dual photography setup (Sen, et al., 2005) (reprinted with permission).

The pixels of the projector individually illuminated the playing card and the subsequent reflections from the card onto the book were imaged by the camera. Using a technique described in the background section of this document, the projector was converted to a "virtual camera" and the face of the playing card was revealed to be the King of Hearts.

While the technique of dual photography is effective for its original purpose, for most applications outside the field of computer generated graphics, there is no reason to attempt dual photography as described above. Simply put, if you are able to get a

pixilated light source in a position to directly view the object of interest, it is much easier to position a camera in that position and image the object directly instead of going through the complicated and data intensive process of creating a dual image. There are however, many applications where discretely viewing an object hidden from direct view of a camera is of interest. Extending the concept of dual photography into one of *indirect photography*, where neither the camera nor the controlling light source has a direct line-of-sight to the object of interest would open up countless new opportunities in the field of remote sensing and other fields of study.

This document details the development of the radiometric theory of indirect photography and the experimental validation of that theory, in which the image of an object was recovered without either the camera or the controlling light source having line of sight to the object of interest. (Figure 2 (b) is an indirect photograph of (a) produced by a co-located digital camera and light source neither of which had direct line-of-sight to the object. Details will appear in Chapter IV)

(a)   (b)

Figure 2. Object of interest (a) and its indirect image (b) created without either the camera or the light source having line-of-sight to the object

This document begins with a background section where dual photography is explained in detail. A brief review of radiometric principles and a technique for

quantitatively describing image quality is also included. The Chapter III fully develops the radiometric theory of dual photography and then extends it to one of indirect photography. The Chapter IV details the three experimental setups used to validate the theory of indirect photography and the resulting data. A brief conclusion, including follow-on research potentials is also included.

While the technique of indirect photography is still in the early stages of development and requires further research before an operational system can exist, the ability to "see around corners" and image hidden objects will have a profound effect on the intelligence community. This document lays the foundation for the development of that capability.

II. Background

This chapter reviews the concept of dual photography in detail and provides a description of the algorithm used to produce a dual image. It also reviews the basic concepts of radiometry and the bi-directional reflection distribution function (BRDF) which are used in the following chapters to develop the concept of indirect photography. The modulation transfer function (MTF) as it relates to image quality and concepts of linear algebra are also discussed.

Helmholtz Reciprocity

Helmholtz reciprocity in its most general form states that the flow of electromagnetic radiation, in particular light, can be reversed without altering its transport properties. Although in his 1856 work on physiological optics, von Helmholtz only discussed specular reflections, Rayleigh's 1900 work extended the theory of reciprocity to include non-specular reflections. In von Helmholtz's own words as quoted by Veach (Veach, 1998)(von Helmholtz & Southall, 1962):

> *Suppose light proceeds by any path whatever from point A to another point B undergoing any number of reflections or refractions en route. Consider a pair of rectangular planes a_1 and a_2 whose line of intersection is along the initial path of the ray at A; and another pair of rectangular planes b_1 and b_2 intersecting along the path of the ray when it comes to B. The components of the vibrations of the aether particles in these two pairs of planes may be imagined. Now suppose that a certain amount of light J leaving the point A in the given direction is polarized in the plane a_1 and that of this light the amount K arrives at the point B polarized in the plane b_1; then it can be proved that, when the light returns over the same path and the quantity of light J polarized in the plane b_1 proceeds from the point, the amount of this light that arrives at the point A polarized in the plane a_1 will be equal to K.*

Apparently the above proposition is true no matter what happens to the light in the way of single or double refraction, reflection, absorption, ordinary dispersion and diffraction, provided that there is no change in its refrangibility, and provided it does not traverse any magnetic medium that affects the position of the plane of polarization, as Faraday found to be the case

Rayleigh's work expanded Helmholtz's work to include non-specular reflections. In his words (Rayleigh & Strutt, 1900):

Suppose that in any direction (i) and at any distance (r) from a small surface (S) reflecting in any manner there be a situated a radiant point (A) of given intensity of the reflected vibrations at any point (B) situated in direction ε and at distance r' from S. The theorem is to the effect that the intensity is the same as it would be at A if the radiant point were transferred to B. [Footnote: I have not thought it necessary to enter into questions connected with polarization, but a more particular statement could easily be made.]

Using modern terminology, if a small reflective surface is illuminated by a small light source, and a small sensor is placed so that it measures the flux being reflected from the surface, then the positions of the light source and the sensor can be exchanged, but the measured reflected flux at the sensor will remain constant (Veach, 1998). It is from this concept of the reversibility of the flow of electromagnetic radiation that the concept of dual photography was derived.

Dual Photography

In a 2005 paper, *Dual Photography*, Sen *et al*. "presented a novel photographic technique called dual photography, which exploits Helmholtz reciprocity to interchange the lights and camera in a scene." (Sen, et al., 2005) The basic premise of dual photography is to use a pixilated light source to illuminate a scene of interest one pixel at a time and record the reflections either directly, or after being reflected from a second

surface. These reflections can then be used to create a matrix which characterizes the light transport from the light source to the camera. This matrix can then be transposed creating the matrix that characterizes the light transport from the camera to the light source.

The authors of the original dual photography paper used the term "primal configuration" to describe the real-world, *i.e.* physical, set-up used to record the data and the term "dual configuration" to describe the situation where the camera and the light source have been reversed, in effect creating a virtual light source out of the original camera and a virtual camera out of the original light source. These conventions will be used for the rest of this document and are explained in further detail in the next two sections.

Primal Configuration

In the primal configuration, a projector with $p \times q$ pixels is used to light a scene one pixel at a time with the resulting reflections imaged by a camera with a resolution of $m \times n$, (see Figure 3).
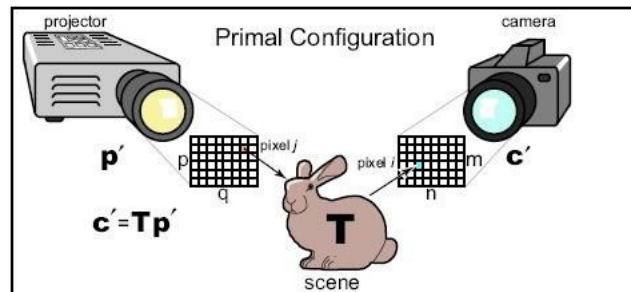
Figure 3. Dual photography primal configuration (Sen, et al., 2005) (reprinted with permission)

Due to linearity of the light transport, the system in Figure 3 can be modeled as (Sen, et al., 2005):

$$c' = \mathbb{T}\, p' \tag{1}$$

where c' is an $mn \times 1$ column vector representing the image recorded by the camera, p' is an $pq \times 1$ column vector representing the light source and $\mathbb{T}$ is an $mn \times pq$ matrix which represents the light transport characteristics from each pixel in the light source to each pixel in the camera (Sen, et al., 2005).

Dual Configuration

Based on Helmholtz reciprocity, it is possible to mathematically interchange the pixilated light source and the camera in Figure 3 without altering the path taken by the light or the energy transfer (Sen, et al., 2005). The dual configuration, shown in Figure 4, is one in which the light source and the camera are mathematically interchanged and can be modeled as:

$$p" = \mathbb{T}^T\, c" \tag{2}$$

where $c"$ is a $mn \times 1$ column vector representing the virtual light source, $p"$ is a $pq \times 1$ column vector representing the virtual camera, and the matrix $\mathbb{T}^T$ transpose of the matrix $\mathbb{T}$ (Sen, et al., 2005).
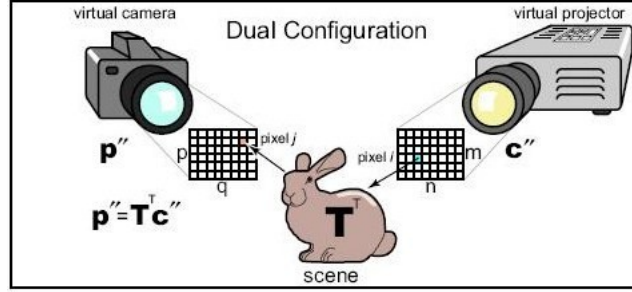
Figure 4. Dual photography dual configuration (Sen, et al., 2005) (reprinted with permission)

Dual Photography Algorithm

When applying the concept of dual photography, for each pixel in the light source of the primal configuration, an individual data image is recorded resulting in $p \times q$ images with a resolution of $m \times n$. This four-dimensional (4-D) set of data ($m \times n \times p \times q$) is then "unfolded" by creating a column vector from each data image and placing it in a column indexed to the given pixel position to form the 2-D $mn \times pq$ transport matrix, $\mathbb{T}$, which describes the light transport characteristics from the light source to the object and from the object to the camera (see Figure 5).

Once the transport matrix is known, Sen *et al.* intended for it be used to add shadows to scenes and decrease the number of calculations required for advanced lighting techniques by modifying the p' vector (Sen, et al., 2005)(Sen & Shheil, 2009).

Given Helmholtz reciprocity, the transpose of the transport matrix ,$\mathbb{T}^{T}$, can be used to describe the light transport characteristics from the camera to the object and from the object to the light source (Sen, et al., 2005). When $\mathbb{T}^{T}$ is multiplied from the right by an $mn \times 1$ column vector, the resulting column vector can then be reassembled to form

the dual image which has, in effect, turned the original light source into a virtual camera (see Figure 6).
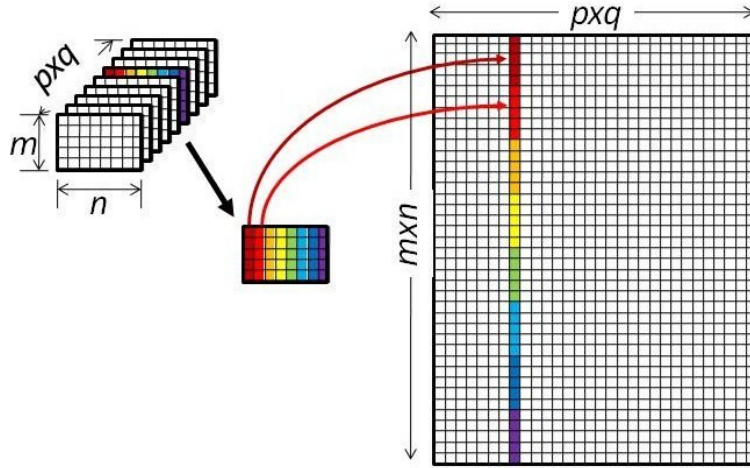
Figure 5. Creating the transport matrix from data images
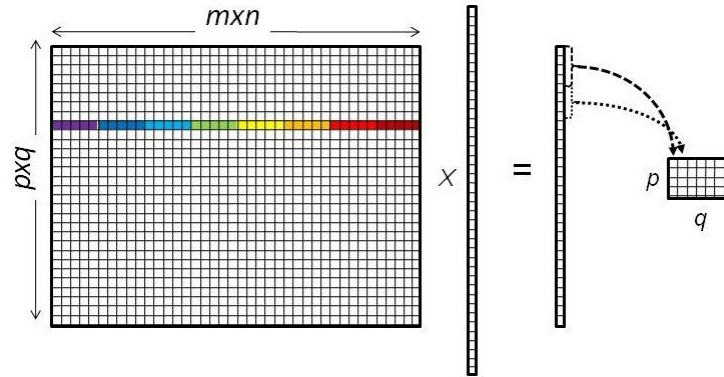
Figure 6. Creating the dual image from the transport matrix

The above discussion was based on a direct path from the object to the camera. This however, is not a necessary condition for the dual photography technique to be used.

The authors of the original paper demonstrated this concept using the set-up in Figure 1 where the dual image of the playing card revealed it to be the King of Hearts even though the camera used to create the transport matrix did not have direct line-of-sight to the playing card.

Radiometry

Radiometry is the quantitative study of the transfer of light. The following two sections outline the basic radiometric principles necessary for understanding the non-specular reflections discussed later in this document.

Solid Angle

The basic unit of reflectance is the solid angle, which is a 3-D cone measured in steradians. The 2-D analogy of the steradian is the radian (see Figure 7). The solid angle is defined as (Driggers, Cox, & Edwards, 1999, p. 91):

$$\Omega = \frac{A}{r^2} \text{ (sr)} \tag{3}$$

where A is the surface area of the sphere subtended by the solid angle, Ω and r is the radius of the sphere. In much the same way, the radian is defined as:

$$\theta = \frac{s}{r} \text{ (rad)} \tag{4}$$

where s is the length of the arc subtended by the angle θ and r is the radius of the circle.
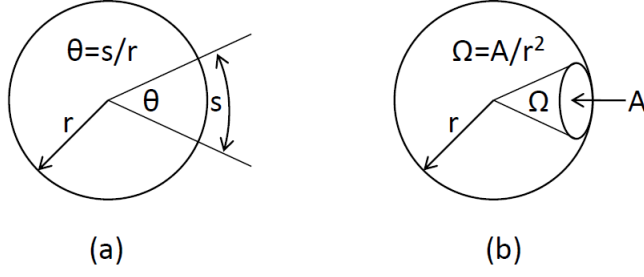
Figure 7. Comparing Radians and Steradians

While the area, A, is the surface area of the sphere subtended by Ω if $A \ll r^2$ then $A \approx A_d$ where A_d is the area of a flat plate that subtends the same solid angle as A, and Eq. (3) can be approximated by (Dereniak & Boreman, 1996, p. 40):

$$\Omega = \frac{A_d}{r^2} \text{ (sr)} \tag{5}$$

If the normal to the surface, A_d, is not directed to the vertex of the cone of the solid angle, then the projected area must be used and Eq. (5) becomes (Dereniak & Boreman, 1996, p. 41):

$$\Omega = \frac{A_d}{r^2} \cos \theta \text{ (sr)} \tag{6}$$

where θ is the angle between the surface normal and the central ray from the vertex to A_d. Likewise, the differential solid angle $\partial \Omega$ can be written as (Dereniak & Boreman, 1996, p. 44):

$$\partial \Omega = \frac{\partial A_d}{r^2} \cos \theta \text{ (sr)} \tag{7}$$

Radiometric Quantities

The basic radiometric equation is flux radiated per projected unit area of the source per solid angle of the detector, mathematically described by (Dereniak & Boreman, 1996, p. 45):

$$L_e = \frac{\partial^2 \Phi_e}{\partial A_s \cos \theta_s \, \partial \Omega_d} (\text{W cm}^{-2}\text{sr}^{-1}) \tag{8}$$

where L_e is the radiance of the surface, $\partial \Phi_e$ is the differential flux, $\partial A_s \cos \theta_s$ is the differential projected area of the source, and $\partial \Omega_d$ is the differential solid angle subtended by the detector. The flux in radiometric equations is typically quantified in one of two units: mks/Joules denoted by a subscripted *e*, or photon units denoted by a subscripted *p*. While either is valid, mks units will be used for this entire document.

All other radiometric quantities can be derived from this basic equation. By rearranging Eq. (8) to isolate flux, it becomes (Dereniak & Boreman, 1996, p. 45):

$$\Phi_e = \iint L_e \cos \theta_s \, \partial A_s \partial \Omega_d (\text{W}) \tag{9}$$

To obtain intensity, which is flux per solid angle, Eq. (9) becomes (Dereniak & Boreman, 1996, p. 46):

$$I_e = \left(\frac{\partial \Phi_e}{\partial \Omega_d} \right) = \int_{A_s} L_e \cos \theta_s \, \partial A_s \, (\text{W sr}^{-1}) \tag{10}$$

which can also be written in differential form:

$$\partial I_e = L_e \cos \theta_s \, \partial A_s (\text{W sr}^{-1}) \tag{11}$$

13

Likewise, to obtain exitance, which is flux per unit area of the source, Eq. (9) now becomes (Dereniak & Boreman, 1996, p. 46):

$$M_e = \left(\frac{\partial \Phi_e}{\partial A_s}\right) = \int_{\Omega_d} L_e \cos\theta_s \, \partial\Omega_d \, (\mathrm{W\,cm^{-2}}) \tag{12}$$

which can also be written in differential form:

$$\partial M_e = L_e \cos\theta_s \, \partial\Omega_d \, (\mathrm{W\,cm^{-2}}) \tag{13}$$

The last equation typically used in radiometry is also the only one from the point of view of the detector. Irradiance is the flux per unit area incident on the detector. Using Eq. (6), the differential solid angle, $\partial\Omega_d$, can be rewritten:

$$\partial\Omega_d = \frac{\partial A_d}{r^2} \cos\theta_d \tag{14}$$

where r is the range between the source and the detector. Substituting Eq. (14) into Eq. (9) yields:

$$\Phi_e = \iint L_e \cos\theta_s \, \partial A_s \left(\frac{\partial A_d}{r^2} \cos\theta_d\right) \tag{15}$$

By combining the r^2 with $\partial A_s \cos\theta_s$ into the differential solid angle subtended by the source:

$$\partial\Omega_s = \frac{\partial A_s}{r^2} \cos\theta_s \tag{16}$$

Eq. (15) becomes:

$$\Phi_e = \iint L_e \cos\theta_d \, \partial\Omega_s \partial A_s \tag{17}$$

14

and the irradiance becomes (Driggers, Cox, & Edwards, 1999, p. 92):

$$E_e = \left(\frac{\partial \Phi_e}{\partial A_d}\right) = \int_{\Omega_s} L_e \cos\theta_d \, \partial\Omega_s (\text{W cm}^{-2}) \tag{18}$$

or in differential form:

$$\partial E_e = L_e \cos\theta_d \, \partial\Omega_s (\text{W cm}^{-2}) \tag{19}$$

In the equations above, if the areas of the source or detector, A_s or A_d, are small compared to the range squared, r^2, the small-angle approximation can be invoked for a uniform source. It assumes the irradiance on the detector can also be considered uniform; therefore, the radiometric equations can be simplified to:

$$\Phi_e = L_e \cos\theta_s \, A_s \Omega_d (\text{W}) \tag{20}$$

$$I_e = \left(\frac{\partial \Phi_e}{\partial \Omega_d}\right) = L_e \cos\theta_s \, A_s (\text{W sr}^{-1}) \tag{21}$$

$$M_e = \left(\frac{\partial \Phi_e}{\partial A_s}\right) = L_e \cos\theta_s \, \Omega_d (\text{W cm}^{-2}) \tag{22}$$

$$E_e = \left(\frac{\partial \Phi_e}{\partial A_d}\right) = L_e \cos\theta_d \, \Omega_s (\text{W cm}^{-2}) \tag{23}$$

A summary of the basic radiometric quantities is contained in Table 3. These equations will be used to create the bi-directional distribution function in the next section.

Table 3. Basic Radiometric Quantities

Symbol	Quantity	Radiometric Ratio	Units
Q_e	Energy		J
Φ_e	Flux		W
L_e	Radiance	$\dfrac{\partial^2 \Phi_e}{\partial A_s \cos \theta_s \, \partial \Omega_d}$	W cm^{-2}sr^{-1}
I_e	Intensity	$\dfrac{\partial \Phi_e}{\partial \Omega_d}$	W sr^{-1}
M_e	Exitance	$\dfrac{\partial \Phi_e}{\partial A_s}$	W cm^{-2}
E_e	Irradiance	$\dfrac{\partial \Phi_e}{\partial A_d}$	W cm^{-2}

Bi-directional Reflectance Distribution Function

The bi-directional reflectance distribution function (BRDF) was initially described by Nicodemus in 1977, and is generally defined as the ratio of the radiance reflected from a surface to the irradiance incident on the same surface from a given solid angle (see Figure 8) (Nicodeums, Richmond, Limperis, Ginsberg, & HSIA, 1977)

$$BRDF(\theta, \phi, \theta', \phi', \bar{x}, \lambda) = \frac{\partial L_e(\theta, \phi, \theta', \phi', \bar{x}, \lambda)}{\partial E_e(\theta, \phi, \bar{x}, \lambda)} (sr^{-1}) \tag{24}$$

or alternately (Stover, 1995, p. 21):

$$f(\theta, \phi, \theta', \phi', \bar{x}, \lambda) = \frac{\partial L_e(\theta, \phi, \theta', \phi', \bar{x}, \lambda)}{\partial E_e(\theta, \phi, \bar{x}, \lambda)} (sr^{-1}) \tag{25}$$

where θ and θ' are the respective incident and reflected elevation angles with respect to the surface normal, ϕ and ϕ' are the respective incident and reflected azimuth angles with respect to a coordinate system in-plane with the reflecting surface, $\bar{x}$ is the position on the reflector and λ is the wavelength of the radiation (see Figure 8). Polarization can be

16

handled using a Stokes vector to represent the incident irradiance, and elements of the Mueller matrix are individual BRDFs (Bickel & Videen, 1991)(Pezzaniti, Chipman, & McClain, 1994). Furthermore, Eq. (25) can be rearranged to give the radiance from a surface given the irradiance and the BRDF of that surface:

$$\partial L_e(\theta, \phi, \theta', \phi', \bar{x}, \lambda) = \partial E_e(\theta, \phi, \bar{x}, \lambda) f(\theta, \phi, \theta', \phi', \bar{x}, \lambda)(\text{W cm}^{-2}\text{sr}^{-1}) \qquad (26)$$

which will be used to develop the radiometric theory of dual and indirect photography.
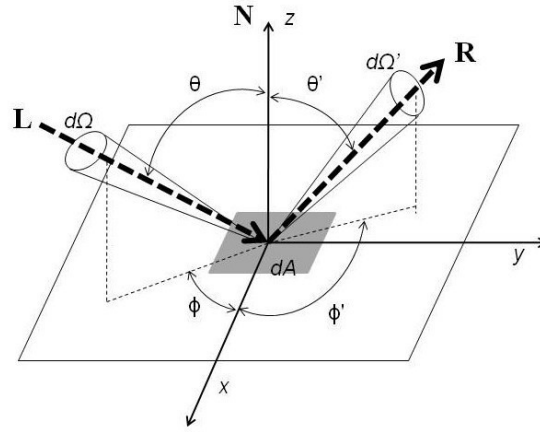
Figure 8. BRDF reference angles (Balling, 2008)

Glint Angle

The glint angle is a construct used to model the BRDF of surfaces. Simply put, the glint vector bisects the incident irradiance vector and reflected radiance vector, in the plane formed by the vectors. The glint angle is the elevation angle of the glint vector with respect to the surface normal (Sundberg, Gruninger, Nosek, Burks, & Fontaine, 1997). See Figure 9 where **G** is the glint vector and Θ is the glint angle. In the model

chosen to simulate the dual/indirect photography experiments, reflected vectors which produce the same glint angle are assigned the same radiance (Torrance & Sparrow, 1967) (Beard & Maxwell, 1973).
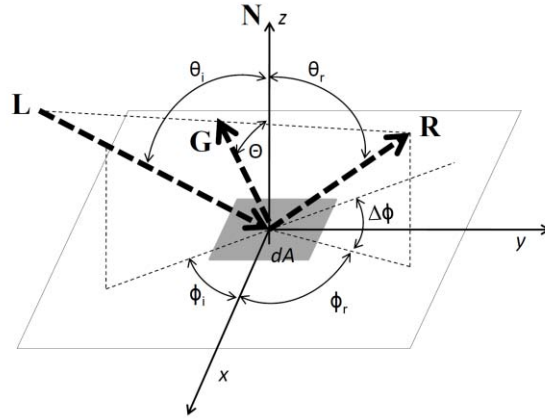
Figure 9. Glint vector and corresponding glint angle

Micro-facet BRDF Model

The micro-facet model assumes the reflecting surface is comprised of a collection of small micro-facts each obeying Snell's law of reflection. Each micro-facet is characterized by its local surface normal and the micro-facets are then distributed, generally, symmetrically about the global surface normal. A well studied form of the BRDF using the glint angle is given by (Priest & Meier, 2002):

$$p(\Theta) = \frac{1}{2\,\pi\,\sigma^2\,cos^{\,3}(\Theta)}\,exp\left(-\frac{tan^2(\Theta)}{2\sigma^2}\right) \qquad (27)$$

where Θ is the glint angle as described above which can be found using Eq. (28) (Priest & Meier, 2002):

$$cos(\Theta) = \frac{\cos(\theta_i) + \cos(\theta_r)}{2\cos(\beta)} \tag{28}$$

where (Priest & Meier, 2002):

$$\cos(2\beta) = \cos(\theta_i)\cos(\theta_r) + \sin(\theta_i)\sin(\theta_r)\cos(\Delta\phi) \tag{29}$$

and θ_i is the incident elevation angle with respect to the global normal, θ_r is the reflected elevation angle with respect to the global normal, and $\Delta\phi$ is the difference between the incident and reflected azimuthal angles (see Figure 8).

Modulation Transfer Function

The quality of an image can be characterized in two ways: 1) the impulse response of the system or 2) its Fourier Transform, the optical transfer function. The impulse response which is also known as the point spread function (PSF), is the 2-D response of the system to a point source (Dereniak & Boreman, 1996, p. 505)(Gaskill, 1978, pp. 334-336).

The object recorded by an imaging system can be described by its radiance as a function of position $f(x, y)$. This function can be further broken down into a series of evenly spaced point sources with intensities equal to the intensity of the object at that point (Goodman, 2005, p. 21). Assuming the system is linear shift invariant (LSI), the PSF of each point of the object, $h(x, y)$, on the image plane, can be summed to form the image, $g(x, y)$. Another way of describing this model of an image is the convolution of the object with the PSF of the imaging system (Dereniak & Boreman, 1996, p. 506).

$$g(x,y) = f(x,y) ** h(x,y) \tag{30}$$

where $**$ denotes a 2-D convolution.

By using the convolution theorem for Fourier transforms, Eq. (30) can be rewritten (Goodman, 2005):

$$G(\xi,\zeta) = F(\xi,\zeta) \times H(\xi,\zeta) \tag{31}$$

where

$$\begin{aligned} G(\xi,\zeta) &= \mathfrak{F}(g(x,y)) \\ F(\xi,\zeta) &= \mathfrak{F}(f(x,y)) \\ H(\xi,\zeta) &= \mathfrak{F}(h(x,y)) \end{aligned} \tag{32}$$

and $\mathfrak{F}$ is the Fourier Transform, ξ is the spatial frequency in the x direction and ζ is the spatial frequency in the y direction. The function H, which is also known as the Optical Transfer Function (OTF), describes the ability of the system to transfer the object's spatial distribution of light to the image plane (Dereniak & Boreman, 1996, p. 507). The OTF is generally a complex valued function; therefore, it can be described with both amplitude and a phase (Dereniak & Boreman, 1996, p. 507) (Gaskill, 1978, p. 358).

$$OTF(\xi,\zeta) = |H(\xi,\zeta)| \exp\{i\theta(\xi,\zeta)\} \tag{33}$$

The modulus of the OTF, $|H(\xi,\zeta)|$, is the modulation transfer function (MTF) and describes the imaging system's ability to transfer the spatial frequency of light to the image plane. Likewise, the argument of the OTF, $\theta(\xi,\zeta)$ is the phase transfer function (PTF) and describes the phase response due to an asymmetry in the PSF (Wolfe & Zissis,

1993, pp. 8-31). Based on Eq. (31), one way to find the MTF without explicitly knowing the OTF or the PSF is (Goodman, 2005, p. 139):

$$\mathbb{M}(\xi,\zeta) = |H(\xi,\zeta)| = \left|\frac{G(\xi,\zeta)}{F(\xi,\zeta)}\right| \tag{34}$$

Another way to think of the MTF is as a measure of the relationship between the brightest and dimmest portions of the image with that of the average level. It is described in the IR Handbook as a measure of what is commonly referred to as contrast (Wolfe & Zissis, 1993, pp. 8-31):

$$\mathbb{M}(\xi_1,\zeta_1) = \frac{L_{max}(\xi_1,\zeta_1) - L_{min}(\xi_1,\zeta_1)}{L_{max}(\xi_1,\zeta_1) + L_{min}(\xi_1,\zeta_1)} \tag{35}$$

where L_{max} is the maximum radiance and L_{min} is the minimum radiance at the specific spatial frequencies ξ_1 and ζ_1. Eq. (35) is most often used when the object is sinusoidal or has regularly-spaced bars such as those commonly found in Air Force bar charts. Due to the nature of the objects chosen for the experiment, Eq. (35) will be modified to:

$$\mathbb{M}' = \frac{White - Black}{White + Black} \tag{36}$$

where $White$ is the average radiance of all the pixels in the test image that are white in the ideal object and $Black$ is the average of the pixels in the test image that are black in the ideal object. The MTF described above will be used to quantitatively describe the ability to resolve spatial frequencies in both dual and indirect images[1].

---

[1] Note: While a traditional MTF ranges from 0, (no modulation), to 1, (no decrease in modulation from the object), the modified MTF ranges from -1, (a perfect negative of the image), to 0 a uniform *i.e.* gray image to 1 a perfect replication of the image.

Linear Shift Invariant Systems

For Eq. (31) to hold, the system must be a Linear Shift Invariant (LSI) system (Gaskill, 1978, p. 139). A system is said to be linear if for a system characterized by the operator, $\mathcal{L}$, then for two arbitrary signals $f_1(x)$ and $f_2(x)$ such that (Boas, 1983, p. 127):

$$\mathcal{L}\{f_1(x)\} = g_1(x)$$
$$\mathcal{L}\{f_2(x)\} = g_2(x)$$

(37)

and constants, a_1 and a_2, then

$$\mathcal{L}\{a_1 f_1(x) + a_2 f_2(x)\} = a_1 g_1(x) + a_2 g_2(x) \tag{38}$$

Likewise, a system is said to be shift invariant if "the only effect caused by a shift in the position of the input is an equal shift in the position of the output" (Gaskill, 1978, p. 139). Therefore, a system is shift invariant if given:

$$\mathcal{L}\{f_1(x)\} = g_1(x) \tag{39}$$

then:

$$\mathcal{L}\{f_1(x - x_o)\} = g_1(x - x_o) \tag{40}$$

The PSF of the dual and indirect images have been assumed to be LSI.

Linear Algebra

Two matrix multiplication concepts of linear algebra which are used in this research are the Hadamard and Kronecker products of matrix multiplication. The Hadamard product, which is sometimes referred to as entrywise product, is formally defined by the following.

Given two matrices of the same dimensions.

$$\mathbb{A}, \mathbb{B} \in \mathbb{R}^{m \times n} \tag{41}$$

then the Hadamard product of $\mathbb{A}$ and $\mathbb{B}$ is defined (Hogban, Brualdi, Greenbaum, & Mathias, 2003):

$$(\mathbb{A} \odot \mathbb{B})_{i,j} = \mathbb{A}_{i,j} \times \mathbb{B}_{i,j} \tag{42}$$

then

$$\mathbb{A} \odot \mathbb{B} \in \mathbb{R}^{m \times n} \tag{43}$$

The Kronecker product is defined as follows:

Given

$$\mathbb{A} \in \mathbb{R}^{m \times n} \tag{44}$$

$$\mathbb{B} \in \mathbb{R}^{p \times q} \tag{45}$$

then the Kronecker product of $\mathbb{A}$ and $\mathbb{B}$ is defined as (Hogban, Brualdi, Greenbaum, & Mathias, 2003):

$$\mathbb{A} \otimes \mathbb{B} = \begin{bmatrix} a_{11}\mathbb{B} & \cdots & a_{m1}\mathbb{B} \\ \vdots & \ddots & \vdots \\ a_{m1}\mathbb{B} & \cdots & a_{mn}\mathbb{B} \end{bmatrix}$$

where

$$\mathbb{A} \otimes \mathbb{B} \in \mathbb{R}^{mp \times nq} \tag{46}$$

Another linear algebra operator used in this document is the Vec operator. The Vec operator takes a matrix as its input and outputs as a column vector by stacking successive columns of the matrix below the previous column as shown in Eq. (47) (Hace & Johnson, 1991):

23

$$Vec \begin{bmatrix} a & c \\ b & d \end{bmatrix} = \begin{bmatrix} a \\ b \\ c \\ d \end{bmatrix} \qquad (47)$$

Complete Angle Scatter Instrument (CASI)

AFIT's complete angle scatter instrument (CASI) is used to experimentally determine the BRDF of selected materials. A calibrated laser illuminates the sample at different incident angles, and the resultant reflections from the sample (*and/or* the transmission through the sample) are measured and recorded by a sensor mounted on a movable arm. Both in-plane and out-of-plane measurements can be performed based on the geometry of the sample's orientation. Figure 10 shows AFIT's CASI.
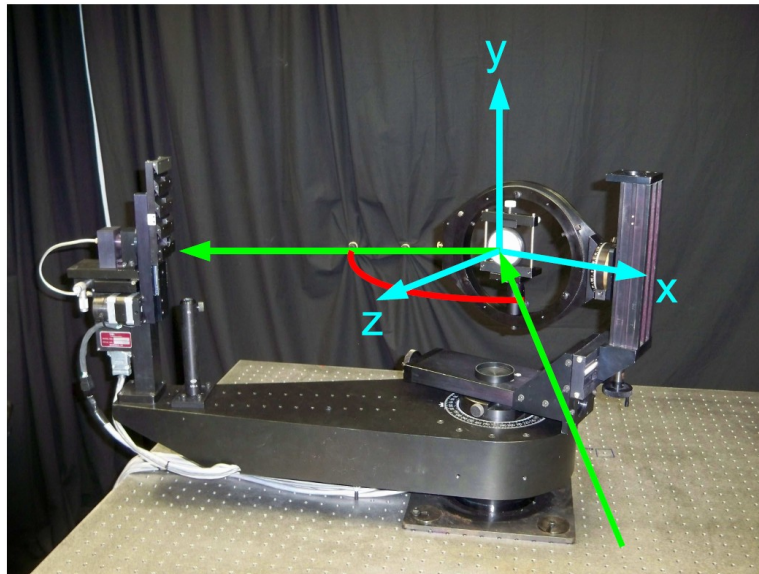
Figure 10. AFIT's complete angle scatter instrument.

Conclusion

This chapter provided a description of dual photography as well as a review of the radiometry, the BRDF, the MTF and linear algebra. The next chapter uses the concepts discussed under the radiometry section to develop the mathematical theory of dual and indirect photography. Chapter IV uses the concepts of the modified MTF to evaluate the image quality of the images produced using the dual or indirect techniques. Chapter V uses the linear algebra to detail a possible method to increase image quality over traditional blind deconvolution techniques.

III. Radiometric Theory of Indirect Photography

This chapter presents the radiometric theory of indirect photography. First, the radiometric theory of dual photography is developed; the theory is then expanded to the radiometric theory of indirect photography. The chapter closes out with a small angle approximation of dual photography. The contents of this chapter dealing with the theory of dual and indirect photography were originally presented at the *SPIE Conference on Reflection, Scattering, and Diffraction from Surfaces II* (Hoelscher & Marciniak, 2010). It has also been submitted for publication to *Optics Express* (Hoelscher & Marciniak, 2011).

Dual Photography

To radiometrically model the dual photography experiment shown in Figure 1, the setup in Figure 11 will be used. In this configuration, a laser is used as the illumination source instead of a pixilated projector. Additionally, instead holding the object fixed and moving the laser spot and camera in unison, the laser and camera are fixed and the playing card is translated. Four coordinate systems, three fixed with respect to each other and one fixed to the object, are used. The x coordinate system is a fixed coordinate system in-plane with the object's translation. The laser spot is centered at its origin. This coordinate system will be referred to as the fixed object frame of reference. The x' coordinate system is attached to the object, *i.e.* the playing card in the original experiment, with the center of the object at the origin. This is the only coordinate system that changes with respect to any other coordinate system during the creation of the dual

image and is referred to as the object frame of reference. The y coordinate system is attached to the non-specular surface imaged by the camera, *i.e.* the book in the original experiment, and will be referred to as the imaged reflector. The z coordinate system is fixed and attached to the lens of the imaging system.
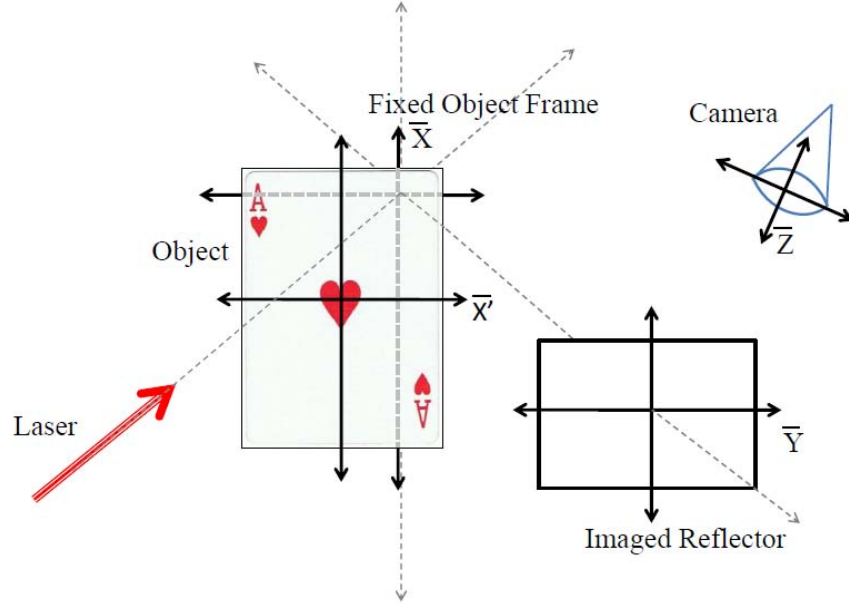
Figure 11. Dual photography coordinate systems

Using the setup in Figure 11, the irradiance due to the laser in the fixed object frame of reference in its most general form is $E_{obj}(\theta_{obj}, \phi_{obj}, \bar{x}, \lambda)$ where θ_{obj} is incident elevation angle of the irradiance with respect to the surface normal, ϕ_{obj} is the incident azimuth angle of the irradiance with respect to the fixed object frame of reference, $\bar{x}$ is a 2-D vector which denotes the position in the fixed object frame of reference and λ is the wavelength of the irradiance. Given the irradiance in the object frame of reference and using Eq. (26), the radiance from the object frame of reference can be written as:

$$L_{obj}\left(\theta_{obj}, \phi_{obj}, \theta'_{obj}, \phi'_{obj}, \bar{x}, \bar{x}', \lambda\right) =$$
$$E_{obj}(\theta_{obj}, \phi_{obj}, \bar{x}, \lambda)f_{obj}\left(\theta_{obj}, \phi_{obj}, \theta'_{obj}, \phi'_{obj}, \bar{x}, \bar{x}', \lambda\right) \tag{48}$$

where θ'_{obj} is the reflected elevation angle with respect to the normal of the fixed object frame of reference, ϕ'_{obj} is the reflected azimuth angle with respect to in the fixed object frame of reference, $\bar{x}'$ is the offset between the fixed object frame of reference and the object, and f_{obj} is the BRDF of the object. Because the irradiation source is a laser, the wavelength, λ, will be considered constant and dropped from further equations for brevity. Additionally, because a laser is used as the irradiation source, the incident solid angle can be considered constant and the irradiance in the fixed object frame of reference, E_{obj}, can be written solely as a function of position in the fixed object frame of reference, $\bar{x}$. Therefore, Eq. (48) can be simplified to:

$$L_{obj}\left(\bar{x}, \bar{x}', \theta_{obj}, \phi_{obj}, \Omega'_{obj}\right) = E_{obj}(\bar{x})f_{obj}\left(\bar{x}, \bar{x}', \theta_{obj}, \phi_{obj}, \Omega'_{obj},\right) \tag{49}$$

where the reflected elevation and azimuth angles, θ'_{obj} and ϕ'_{obj}, have been combined to form the reflected solid angle, Ω'_{obj}. Assuming the BRDF of the object is isotropic and uniformly scaled in magnitude by the reflectance of the object at that point two simplifications can be made: (1) the BRDF of the object no longer has a dependence on the incident azimuth angle with, ϕ_{obj} and (2) the BRDF can be decomposed into:

$$f_{obj}\left(\bar{x}, \bar{x}', \theta_{obj}, \Omega'_{obj}\right) = \rho(\bar{x}' - \bar{x})f_{ph}\left(\bar{x}, \theta_{obj}, \Omega'_{obj}\right) \tag{50}$$

where f_{ph} is the underlying angular shape of the BRDF (sometimes referred to as the "phase function" and therefore the *ph* subscript) that is scaled by ρ, the reflectance of the

object at the point, $\bar{x}'$. To validate the assumption that the BRDF can be decomposed into a reflectance and a phase function, AFIT's CASI was used to measure the BRDF of the white, black and red portions of a standard playing card, the results can be found in Appendix A. Substituting Eq. (50) into Eq. (49) the radiance of the object becomes:

$$L_{obj}\left(\bar{x},\bar{x}',\theta_{obj},\Omega'_{obj}\right) = E_{obj}(\bar{x})\rho(\bar{x}' - \bar{x})f_{ph}\left(\theta_{obj},\Omega'_{obj}\right) \qquad (51)$$

Given the radiance of the object reflector, and using Eq. (19), the differential irradiance on the imaged reflector from a differential area on the object is:

$$dE_{im}\left(\bar{x},\bar{x}',\theta_{obj},\Omega'_{obj},\theta_{im}\right) = L_{obj}\left(\bar{x},\bar{x}',\theta_{obj},\Omega'_{obj}\right)\cos\theta_{im}\,d\Omega_{im} \qquad (52)$$

where θ_{im} is the incident elevation angle with respect to the surface normal of the irradiance on the imaged reflector and $d\Omega_{im}$ is the differential solid angle incident on the imaged reflector that is subtended by a differential projected area of the object (see Figure 12).
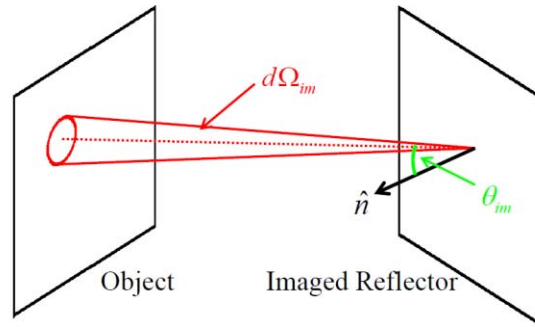
Figure 12. Differential solid angle ($d\Omega_{im}$) and incident angle with respect to the normal (θ_{im})

Given the fixed geometry of the experiment, Ω'_{obj}, θ_{im} and $d\Omega_{im}$ depend only on the positions in the fixed object frame of reference and on the imaged reflector, therefore they can be written solely as functions of $\bar{x}$ and $\bar{y}$ (see Figure 13).
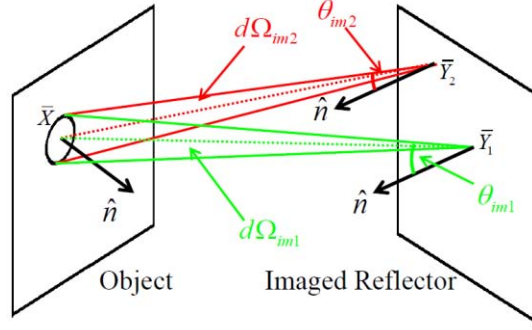
Figure 13. Angular dependence on $\bar{x}$ and $\bar{y}$.

Rewriting Eq. (52) explicitly in terms of $\bar{x}$ and $\bar{y}$:

$$dE_{im}(\bar{x}, \bar{x}', \bar{y}, \theta_{obj}) = L_{obj}(\bar{x}, \bar{x}', \bar{y}, \theta_{obj})\cos\theta_{im}(\bar{x}, \bar{y})\, d\Omega_{im}(\bar{x}, \bar{y}) \tag{53}$$

Using the definition of a solid angle, Eq. (7), the differential solid angle incident on the imaged reflector, $d\Omega_{im}$, can be rewritten:

$$d\Omega_{im}(\bar{x}, \bar{y}) = \frac{\cos\theta'_{obj}(\bar{x}, \bar{y})}{r^2_{im}(\bar{x}, \bar{y})} dA_{obj}(\bar{x}) \tag{54}$$

where θ'_{obj} is the reflected elevation angle of the radiance with respect to the surface normal of the differential area of the object, r_{im} is the range between points in the fixed object frame of reference and the imaged reflector, $\bar{x}$ and $\bar{y}$, respectively, and dA_{obj} is the differential area of the object (see Figure 14).
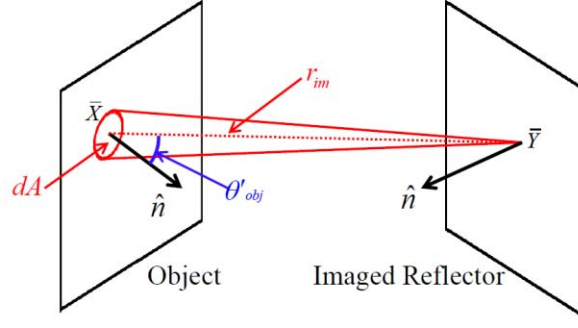
Figure 14. Converting from a differential solid angle to a differential area

Substituting Eq. (54) into Eq. (53) yields:

$$dE_{im}(\bar{x}, \bar{x}', \bar{y}, \theta_{obj}) =$$

$$L_{obj}(\bar{x}, \bar{x}', \bar{y}, \theta_{obj})\cos\theta_{im}(\bar{x}, \bar{y}) \left(\frac{\cos\theta'_{obj}(\bar{x}, \bar{y})}{r_{im}^2(\bar{x}, \bar{y})} dA_{obj}(\bar{x}) \right) \tag{55}$$

By combining like terms, Eq. (55) can be rewritten:

$$dE_{im}(\bar{x}, \bar{x}', \bar{y}, \theta_{obj}) = L_{obj}(\bar{x}, \bar{x}', \bar{y}, \theta_{obj})\alpha(\bar{x}, \bar{y})dA_{obj}(\bar{x}) \tag{56}$$

where

$$\alpha(\bar{x}, \bar{y}) = \frac{\cos\theta'_{obj}(\bar{x}, \bar{y})\cos\theta_{im}(\bar{x}, \bar{y})}{r_{im}^2(\bar{x}, \bar{y})} \tag{57}$$

Again, given the irradiance on the imaged reflector and using Eq. (26), the radiance from the imaged reflector can be written as:

$$L_{im}(\bar{x}, \bar{x}', \bar{y}, \bar{z}, \theta_{obj}) = E_{im}(\bar{x}, \bar{x}', \bar{y}, \theta_{obj}) f_{im}(\bar{y}, \theta_{im}, \phi_{im}, \theta'_{im}, \phi'_{im}) \tag{58}$$

where f_{im} is the BRDF of the imaged reflector, θ_{im} and θ'_{im} are the incident and reflected elevation angles with respect to the normal of the imaged reflector, ϕ_{im} and ϕ'_{im} are the

incident and reflected azimuth angles with respect to the imaged reflector frame of reference, and $\bar{y}$ is 2-D vector that denotes the position on the imaged reflector. Assuming the imaged reflector is uniform and isotropic, the BRDF can be simplified and Eq.(58) can be rewritten:

$$L_{im}(\bar{x},\bar{x}',\bar{y},\bar{z},\theta_{obj}) = E_{im}(\bar{x},\bar{x}',\bar{y},\theta_{obj})\, f_{im}(\theta_{im},\Omega'_{im}) \tag{59}$$

where the reflected elevation and azimuth angles, θ'_{im} and ϕ'_{im}, have been combined to form the reflected solid angle Ω'_{im}. Converting θ_{im} and Ω'_{im} into positions in the object frame of reference, $\bar{x}$, position on the imaged reflector, $\bar{y}$, and position on the lens of the imaging system, $\bar{z}$, Eq. (59) can be rewritten:

$$L_{im}(\bar{x},\bar{x}',\bar{y},\bar{z},\theta_{obj}) = E_{im}(\bar{x},\bar{x}',\bar{y},\theta_{obj})\, f_{im}(\bar{x},\bar{y},\bar{z}) \tag{60}$$

Given the radiance from the imaged reflector, and again using Eq. (19), the differential irradiance at any point on the lens of the imaging system from a differential area on the imaged reflector is:

$$dE_{lens}(\bar{x},\bar{x}',\bar{y},\bar{z},\theta_{obj}) = L_{im}(\bar{x},\bar{x}',\bar{y},\bar{z},\theta_{obj})cos\theta_{lens}(\bar{y},\bar{z})d\Omega_{lens}(\bar{y},\bar{z}) \tag{61}$$

where θ_{lens} is the incident elevation angle with respect to the surface normal of the lens of the imaging system and $d\Omega_{lens}$ is the incident solid angle of the radiation on the lens subtended by a differential area of the imaged reflector. Using Eq. (7) to convert the solid angle, Eq. (61) can be rewritten:

$$dE_{lens}\left(\bar{x},\bar{x}',\bar{y},\bar{z},\theta_{obj}\right) =$$

$$L_{im}\left(\bar{x},\bar{x}',\bar{y},\bar{z},\theta_{obj}\right)cos\theta_{lens}(\bar{y},\bar{z})\left(\frac{cos\theta'_{im}(\bar{y},\bar{z})}{r^2_{lens}(\bar{y},\bar{z})}dA_{im}(\bar{y})\right) \qquad (62)$$

where θ'_{im} is the reflected elevation angle with respect to the surface normal of the imaged reflector, r_{lens} is the distance between the points on the imaged reflector and the lens of the imaging system, $\bar{y}$ and $\bar{z}$ respectively, and dA_{im} the is differential area on the imaged reflector. Again combining like terms, Eq. (62) can be simplified:

$$dE_{lens}\left(\bar{x},\bar{x}',\bar{y},\bar{z},\theta_{obj}\right) = L_{im}\left(\bar{x},\bar{x}',\bar{y},\bar{z},\theta_{obj}\right)\beta(\bar{y},\bar{z})dA_{im}(\bar{y}) \qquad (63)$$

where

$$\beta(\bar{y},\bar{z}) = \frac{cos\theta'_{im}(\bar{y},\bar{z})cos\theta_{lens}(\bar{y},\bar{z})}{r^2_{lens}(\bar{y},\bar{z})} \qquad (64)$$

Given Eq. (63) and by using Eqs. (51), (56), and (60) the irradiance on a point on the lens of the imaging system, $\bar{z}$, for a given object position and incident elevation angle of the laser on the fixed object frame of reference, $\bar{x}'$ and θ_{obj}, respectively, is:

$$E_{lens}\left(\bar{x}',\bar{z},\theta_{obj}\right) =$$

$$\int_{im}\int_{obj} E_{obj}(\bar{x})\rho(\bar{x}'-\bar{x})f_{ph}\left(\bar{x},\bar{y},\theta_{obj}\right)f_{im}(\bar{x},\bar{y},\bar{z})\alpha(\bar{x},\bar{y})\,\beta(\bar{y},\bar{z})d\bar{x}\,d\bar{y} \qquad (65)$$

where $\bar{x}$ is integrated over the object, and $\bar{y}$ is integrated over the imaged reflector. If the irradiance outside the laser spot is zero, Eq. (65) can be rewritten:

33

$$E_{lens}\left(\bar{x}', \bar{z}, \theta_{obj}\right) =$$

$$\int_{im} \int_{las} E_{obj}(\bar{x})\rho(\bar{x}' - \bar{x})f_{ph}\left(\bar{x}, \bar{y}, \theta_{obj}\right)f_{im}(\bar{x}, \bar{y}, \bar{z})\alpha(\bar{x}, \bar{y})\,\beta(\bar{y}, \bar{z})d\bar{x}\,d\bar{y} \quad (66)$$

where $\bar{x}$ is now integrated over the laser spot. Given Eq. (66), the total flux collected by the lens for a given pixel on the camera can be written as:

$$\Phi_{\text{pix}_i}\left(\bar{x}', \theta_{obj}\right) =$$

$$\int_{lens} \int_{fov_i} \int_{las} E_{obj}(\bar{x})\rho(\bar{x}' - \bar{x})f_{ph}\left(\bar{x}, \bar{y}, \theta_{obj}\right)f_{im}(\bar{x}, \bar{y}, \bar{z})\alpha(\bar{x}, \bar{y})\,\beta(\bar{y}, \bar{z})d\bar{x}\,d\bar{y}d\bar{z} \quad (67)$$

where fov_i is the projected area of camera pixel i on the imaged reflector (see Figure 15).
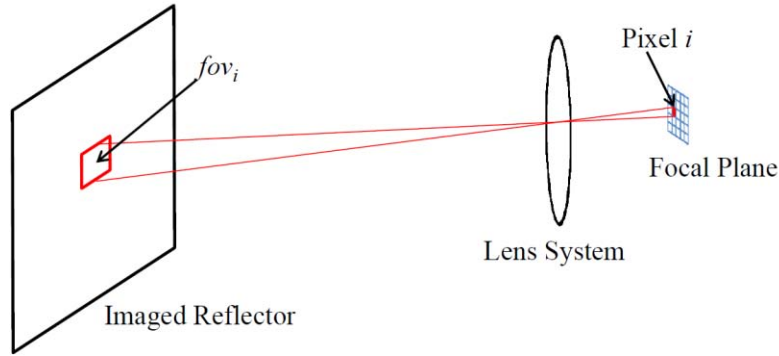
Figure 15. Field of view of an individual pixel

The order of integration can be rearranged and Eq. (67) simplified to:

$$\Phi_{pix_i}\left(\bar{x}', \theta_{obj}\right) = \int_{las} \Gamma_i\left(\bar{x}, \theta_{obj}\right)\rho(\bar{x}' - \bar{x})d\bar{x} \quad (68)$$

where:

$$\Gamma_i(\bar{x}, \theta_{obj}) = \int_{lens} \int_{fov_i} E_{obj}(\bar{x}) f_{ph}(\bar{x}, \bar{y}, \theta_{obj}) f_{im}(\bar{x}, \bar{y}, \bar{z}) \alpha(\bar{x}, \bar{y}) \, \beta(\bar{y}, \bar{z}) d\bar{y} \, d\bar{z} \qquad (69)$$

As a consequence of Eq. (68), a dual image can be created by using any single pixel, group of pixels or the entire digital image without explicit knowledge of the geometry, as long as the same pixel or set of pixels is used to create the dual image across all of the recorded data images. Furthermore, with a change of variables, $(\bar{x} = \bar{x}' - \bar{x}'')$, Eq. (68) can be rewritten:

$$\Phi_{pix_i}(\bar{x}', \theta_{obj}) = \int_{las} \Gamma_i(\bar{x}' - \bar{x}'', \theta_{obj}) \, \rho(\bar{x}'') \, d\bar{x}'' \qquad (70)$$

showing Γ_i to be the convolution kernel, *i.e.* the point spread function (PSF), for the dual image. If the irradiance of the laser spot and some knowledge of the BRDFs and geometries in Γ_i are known, the quality of the dual image can be improved by a deconvolution of the dual image and this kernel. It is this improvement in the image quality by the deconvolution of the irradiance on the object of interest that will be shown can be exploited to expand the concept of dual photography into one of indirect photography and allow for the recovery of information that is not directly visible to either the controlling illumination source or the imaging system.

Indirect Photography

As previously stated, one limiting factor of dual photography is the requirement for the illumination source, or the imaging system, to have a direct view of the object of

interest. To eliminate that requirement, the dual photography experiment modeled above will now be expanded and modeled with the illumination source reflecting from a non-specular surface prior to illuminating the object of interest. For example, if the laser is moved adjacent to the camera so that it could not illuminate the face of the playing card directly but now illuminates the diffuse imaged reflector as shown in Figure 16.
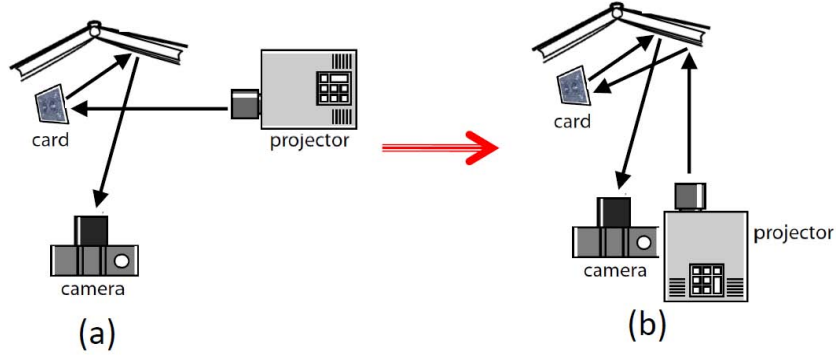

Figure 16. Real world setup for (a) dual photography and (b) indirect photography.

To aid in the modeling, the first surface has been separated from the imaged reflector and an additional fixed reference frame, $\overline{w}$, has been added to describe the first non-specular surface and will be referred to as the wall reflector (see Figure 17).

As in the previous section, because the illumination source is a laser, both the wavelength and incident solid angle can be considered constant and the general form of the irradiance on the wall reflector $E_{wall}(\theta_{wall}, \phi_{wall}, \overline{w}, \lambda)$ can again be simplified to $E_{wall}(\overline{w})$, where $\overline{w}$ is a 2-D vector which denotes the position on the wall reflector. Given the irradiance on the reflector and using Eq. (26), the radiance from the wall reflector is:

$$L_{wall}\left(\overline{w}, \theta_{wall}, \phi_{wall}, \theta'_{wall}, \phi'_{wall}\right) =$$

$$\text{(71)}$$

$$E_{wall}(\overline{w})f_{wall}\left(\overline{w}, \theta_{wall}, \phi_{wall}, \theta'_{wall}, \phi'_{wall}\right)$$

where θ_{wall} and θ'_{wall} are the incident and reflected elevation angles with respect to the surface normal of the wall reflector, ϕ_{wall} and ϕ'_{wall} are the incident and reflected azimuth angles with respect to the wall reflector frame of reference and f_{wall} is the BRDF of the wall reflector.
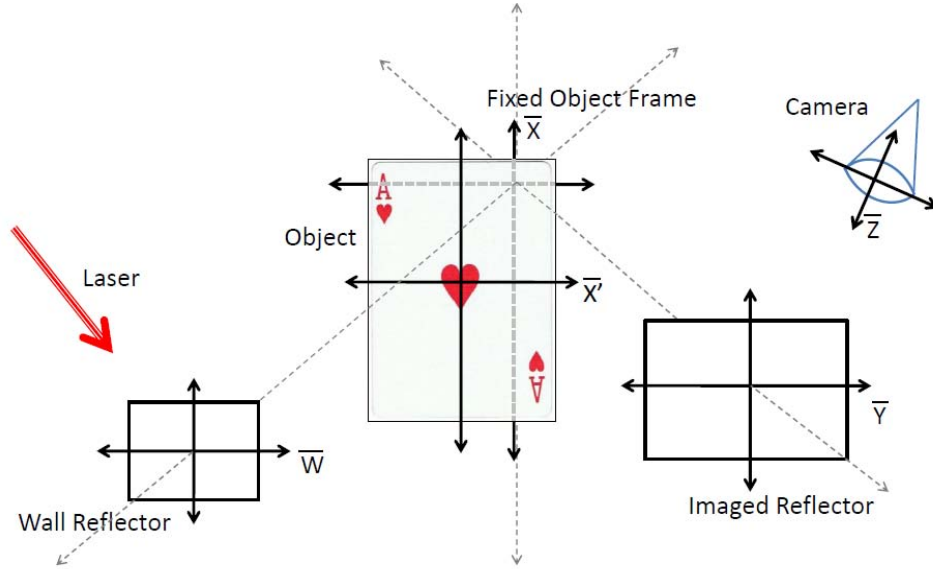
Figure 17. Indirect Photography coordinate systems

Assuming the wall reflector is both homogenous and isotropic, the BRDF of the wall reflector can be simplified and Eq. (71) can be rewritten:

$$L_{wall}(\overline{w}, \theta_{wall}, \Omega'_{wall}) = E_{wall}(\overline{w})f_{wall}(\theta_{wall}, \Omega'_{wall}) \qquad \text{(72)}$$

where the reflected elevation and azimuth angles, θ'_{wall} and ϕ'_{wall}, have been combined to form the reflected solid angle, Ω'_{wall}. Given the radiance from a differential area of

the wall reflector and using Eq. (19), the differential irradiance on the object frame of reference is:

$$dE_{obj}(\overline{w}, \theta_{wall}, \theta_{obj}, \Omega_{obj}) = L_{wall}(\overline{w}, \theta_{wall}, \Omega'_{wall})cos\theta_{obj}d\Omega_{obj} \tag{73}$$

where θ_{obj} is the incident elevation angle of the irradiance with respect to the surface normal in the fixed object frame of reference and $d\Omega_{obj}$ is the differential incident solid angle of the irradiance. Again, using Eq. (7) and converting the differential solid angle to differential area yields:

$$dE_{obj}(\overline{w}, \theta_{obj}, \theta'_{wall}, \Omega_{wall}) =$$

$$L_{wall}(\overline{w}, \theta_{wall}, \Omega'_{wall})cos\theta_{obj}\left(\frac{cos\theta'_{wall}}{r^2_{obj}}dA_{wall}\right) \tag{74}$$

where θ'_{wall} is the reflected elevation angle with respect to the surface normal of the radiance from the wall reflector, r_{obj} is the range between the points on the wall reflector and the position in the fixed object frame of reference, $\overline{w}$ and $\bar{x}$ respectively, and dA_{wall} is the differential area of the wall reflector. As in the previous section, because of the fixed geometry between the wall reflector and the fixed object frame of reference, all of the angles can be written explicitly as functions of $\overline{w}$ and $\bar{x}$. Rewriting Eq. (74) yields:

$$dE_{obj}(\overline{w}, \bar{x}, \theta_{wall}) =$$

$$L_{wall}(\overline{w}, \bar{x}, \theta_{wall})cos\theta_{obj}(\overline{w}, \bar{x})\left(\frac{cos\theta'_{wall}(\overline{w}, \bar{x})}{r^2_{obj}(\overline{w}, \bar{x})}dA_{wall}(\overline{w})\right) \tag{75}$$

and by combining like terms, Eq. (75) can be rewritten:

$$dE_{obj}(\overline{w}, \overline{x}, \theta_{wall}) = L_{wall}(\overline{w}, \overline{x}, \theta_{wall})\, \gamma(\overline{w}, \overline{x})\, dA_{wall}(\overline{w}) \tag{76}$$

where:

$$\gamma(\overline{w}, \overline{x}) = \frac{\cos\theta'_{wall}(\overline{w}, \overline{x})\cos\theta_{obj}(\overline{w}, \overline{x})}{r^2_{obj}(\overline{w}, \overline{x})} \tag{77}$$

Eq. (76) can now be inserted into Eq. (67) to give the total flux collected by a single pixel for a given object position and the incident elevation angle of the laser with respect to the normal of the wall reflector:

$$\Phi_{pix_i}(\overline{x}', \theta_{wall}) = \int_{las}\int_{obj}\int_{fov_i}\int_{lens} E_{wall}(\overline{w})\, \rho(\overline{x}' - \overline{x})\, f_{wall}(\overline{w}, \overline{x}, \theta_{wall}) \times$$
$$f_{ph}(\overline{w}, \overline{x}, \overline{y})f_{im}(\overline{x}, \overline{y}, \overline{z})\gamma(\overline{w}, \overline{x})\alpha(\overline{x}, \overline{y})\,\beta(\overline{y}, \overline{z})\, d\overline{z}\, d\overline{y}\, d\overline{x}\, d\overline{w} \tag{78}$$

where $d\overline{z}$ is integrated over the area of the lens of the imaging system, $d\overline{y}$ is integrated over the projected area of camera pixel i on the imaged reflector, $d\overline{x}$ is now integrated over the entire object and $d\overline{w}$ is integrated over the laser spot. Eq. (78) can be simplified to:

$$\Phi_{pix_i}(\overline{x}', \theta_{wall}) = \int_{las}\int_{obj} \Gamma_i(\overline{w}, \overline{x})\, \rho(\overline{x}' - \overline{x}) \times$$
$$E_{wall}(\overline{w})f_{wall}(\overline{w}, \overline{x}, \theta_{wall})\gamma(\overline{w}, \overline{x})\, d\overline{x}\, d\overline{w} \tag{79}$$

where:

$$\Gamma_i(\overline{w}, \overline{x}) = \int_{fov_i}\int_{lens} f_{ph}(\overline{w}, \overline{x}, \overline{y})f_{im}(\overline{x}, \overline{y}, \overline{z})\alpha(\overline{x}, \overline{y})\,\beta(\overline{y}, \overline{z})\, d\overline{z}\, d\overline{y} \tag{80}$$

The order of integration can be rearranged and Eq. (79) further simplified to:

$$\Phi_{pix_i}(\bar{x}', \theta_{wall}) = \int_{obj} T_i(\bar{x}, \theta_{wall}) \, \rho(\bar{x}' - \bar{x}) \, d\bar{x} \tag{81}$$

where:

$$T_i(\bar{x}, \theta_{wall}) = \int_{las} \Gamma_i(\bar{w}, \bar{x}, \theta_{wall}) \, E_{wall}(\bar{w}) f_{wall}(\bar{w}, \bar{x}, \theta_{wall}) \, \gamma(\bar{w}, \bar{x}) d\bar{w} \tag{82}$$

As with Eq. (68), a consequence of Eq. (81) is an indirect image can be created by using any single pixel, group of pixels or the entire digital image without explicit knowledge of the geometry, as long as the same set of pixels is used to create the dual image across all of the recorded images. Likewise, Eq. (82) can also be rewritten with a change of variables:

$$\Phi_{pix_i}(\bar{x}', \theta_{wall}) = \int_{obj} T_i(\bar{x}' - \bar{x}'', \theta_{wall}) \, \rho(\bar{x}'') \, d\bar{x}'' \tag{83}$$

as in the case of the dual image, the indirect image is the convolution of the point spread function, T_i, and the object of interest, ρ. Due to the nature of the problem, the point spread function will probably not be fully known; it should however, be possible to improve the image quality using blind deconvolution techniques.

Dual Photography Approximation

In the above derivations of dual and indirect photography, assumptions were made about the BRDFs of the reflectors, *i.e* that they were homogeneous and isotropic. No assumptions, however, were made about the geometry of the setup(s). If two assumptions are made about the geometry of the setup, Eq. (70) can be significantly

simplified and the convolution kernel in dual photography can be approximated with the laser irradiance on the object.

The two assumptions that must be made are: (1) both the area of the laser spot on the object and the projected area of pixel i on the imaged reflector are much less than the range between the two points squared, r_{im}^2, and (2) the incident elevation angle of the laser on the object, θ_{obj}, is constant. The first assumption means r_{im} can be considered constant for the range between any point with the laser spot and any point in within the projected pixel area. Also if the first assumption is true, then the reflected elevation angle from object frame of reference, θ'_{obj}, will vary only slightly across all possible combinations of $\bar{x}$ and $\bar{y}$; therefore, $\cos\theta'_{obj}(x,y)$, of the angle can be considered constant. Likewise, the cosine of the incident elevation angle on the imaged reflector, θ_{im}, can also be considered constant. This allows Eqs. (57) and (64) to be rewritten:

$$\alpha(\bar{x},\bar{y}) \Rightarrow \frac{\cos\theta'_{obj}(\bar{x}_o,\bar{y}_o)\cos\theta_{im}(\bar{x}_o,\bar{y}_o)}{r_{im}^2(\bar{x}_o,\bar{y}_o)} \Rightarrow \alpha_i \tag{84}$$

$$\beta(\bar{y},\bar{z}) \Rightarrow \frac{\cos\theta'_{im}(\bar{y}_o,\bar{z})\cos\theta_{lens}(\bar{y}_o,\bar{z})}{r_{lens}^2(\bar{y}_o,\bar{z})} \Rightarrow \beta_i(\bar{z}) \tag{85}$$

where $\bar{x}_o$ and $\bar{y}_o$ are constants representing the center position of the laser spot and the pixel, respectively, and the i subscript denotes the pixel. If the second assumption is true, as is the case when the laser is translated horizontally and vertically, and by holding $\bar{x}$ and $\bar{y}$ constant, the BRDF phase component of the object, f_{ph}, can also be considered constant; *i.e.* if the reflected solid angle is small, the BRDF within that solid angle will vary only slightly, and can therefore be rewritten:

$$f_{ph}(\bar{x}, \bar{y}, \theta_{obj}) \Rightarrow f_{ph}\left(\bar{x}_o, \bar{y}_o, \theta_{o\,obj}\right) \Rightarrow f_{ph_i} \tag{86}$$

Again, if the laser spot is small in comparison to the range between the laser spot and the projection of the pixel, then the incident solid angle of the irradiance on the imaged reflector can be considered constant across the laser spot and the BRDF of the imaged reflector, f_{im}, can be rewritten:

$$f_{im}(\bar{x}, \bar{y}, \bar{z}) \Rightarrow f_{im}(\bar{x}_o, \bar{y}_o, \bar{z}) \Rightarrow f_{im_i}(\bar{z}) \tag{87}$$

Using Eqs. (84) through (87), Eq. (69) becomes:

$$\Gamma'_i(\bar{x}) = \int_{lens} \int_{fov_i} E_{obj}(\bar{x})\, f_{ph_i}\, f_{im_i}(\bar{z})\, \alpha_i\, \beta_i(z) d\bar{y}\, d\bar{z} \tag{88}$$

Rearranging the integral yields:

$$\Gamma'_i(\bar{x}) = E_{obj}(\bar{x})\alpha_i\, f_{ph_i} \int_{fov_i} d\bar{y} \int_{lens} f_{im_i}(\bar{z})\beta_i(z) d\bar{z} \tag{89}$$

The integration over the field of view of the pixel can be evaluated and yields the area of the pixel which is a constant.

$$A_i = \int_{fov_i} d\bar{y} \tag{90}$$

and given the fixed geometry of the setup, the integration of f_{im_i} and β_i over the area of the lens can be evaluated and yields a constant

$$f_{im_i} = \int_{lens} f_{im_i}(\bar{z})\beta_i(z) d\bar{z} \tag{91}$$

Substituting Eqs. (90) and (91) into Eq. (89) yields:

$$\Gamma'_i(\bar{x}) = E_{obj}(\bar{x})\alpha_i\, f_{ph_i}A_i f_{im_i} \tag{92}$$

which can be simplified to:

$$\Gamma'_i(\bar{x}) = K_i\, E_{obj}(\bar{x}) \tag{93}$$

where

$$K_i = \alpha_i\, f_{ph_i}A_i f_{im_i} \tag{94}$$

It is important to note that K_i varies from one pixel to the next but for each pixel i, K_i will remain constant for all data images. Substituting Eq. (94) into Eq. (68) yields:

$$\Phi_{pix_i}(\bar{x}') = K_i \int_{las} E_{obj}(\bar{x})\rho(\bar{x}' - \bar{x})d\bar{x} \tag{95}$$

which through a change of variables can be rewritten:

$$\Phi_{pix_i}(\bar{x}') = K_i \int_{las} E_{obj}(\bar{x}' - \bar{x}'')\rho(\bar{x}'')d\bar{x}'' \tag{96}$$

Eq. (96) suggests the complete geometry of a dual photography setup is not necessary to improve the image. Instead, the irradiance of the controlling illumination, in this case the laser, can be used as the deconvolution kernel.

Conclusion

This chapter developed the radiometric theory of both dual and indirect photography. It also included a simplification of the radiometric equation of dual photography. To verify Eqs. (70), (83) and (96), *i.e.* that the image produced by either dual or indirect photography is a convolution of the original object of interest and either

43

the laser spot in the case of dual photography or an unknown point spread function in the case of indirect photography, both a MATLAB simulation and a physical experiment described in the next chapter of this document were used.

IV. Experimental Verification

To verify the radiometric theory of indirect photography described in Chapter III, a basic simulation and three different experiments were accomplished in a building block approach. The first experiment was a 1-D experiment with the illumination source and the camera separated to mimic the theoretical model. Sinusoidal slides and a separated object reflector were used as the object. The experiment was then expanded to 2-D where the sinusoidal slides were replaced with more representative 2-D objects. In the final experiment, the illumination source and the laser were co-located to create a real-world scenario. This chapter describes the simulation as well as the three experimental setups and discusses the results.

Simulation

Following the development of the radiometric theory of indirect photography, a MATLAB simulation was created to verify the results of Eqs. (70), (83) and (96), *i.e.* that the image quality of both dual and indirect images are improved following the deconvolution process. To that end, Eqs. (67) and (78) were used to calculate the total flux incident on the lens of the imaging system for the dual and indirect image, respectively. The resultant images were then improved through the deconvolution processes. The image quality was evaluated for both the unimproved images and recovered images following deconvolution. A description of the simulation and the subsequent results are described below.

The simulation was based on the micro-facet model discussed in the background section of this document and consisted of a wire frame model for each reflector. The three reflectors and the lens of the imaging system were modeled by the following sets of points: (1) the wall reflector consisted of 9 points in a 3x3 pattern, (2) the object reflector consisted of 625 points in a 25x25 pattern, (3) the imaged reflector consisted of 441 points in a 21x21 pattern, and (4) the lens of imaging system consisted of 9 points in a 3x3 pattern. Two objects were used for the simulation. The first object was a single white square on a black background, so the PSF of the system could be evaluated. The second object consisted of a two white squares separated both vertically and horizontally by one side length on a black background. For reference, the squares used to create the objects subtended approximately 0.08 mrad at the distance modeled in the simulation.

Each component of Eqs. (67) and (78) was calculated and stored in look-up tables to decrease the time requirements to run the model. The Priest and Meier BRDF, Eq. (27), a well studied form of the BRDF using the glint vector, was used to used to model the BRDF of each of the reflectors. The BRDF of the wall reflector was chosen so that when the object was in the center position, the radiance from the wall reflection would cover the entire object. Figure 18 shows the glint angle from the center point on the wall reflector to every point in the fixed object frame of reference and Figure 19 is an overlay of the irradiance in the object frame of reference and the two square object when it is in the center position.

The laser was modeled as a 3x3 Gaussian beam, Eq. (97), shows the matrix representation of the irradiance on the wall reflector used for the simulation.

$$E_{wall}(\bar{w}) = \begin{bmatrix} 1 & 2 & 1 \\ 2 & 5 & 2 \\ 1 & 2 & 1 \end{bmatrix} \tag{97}$$
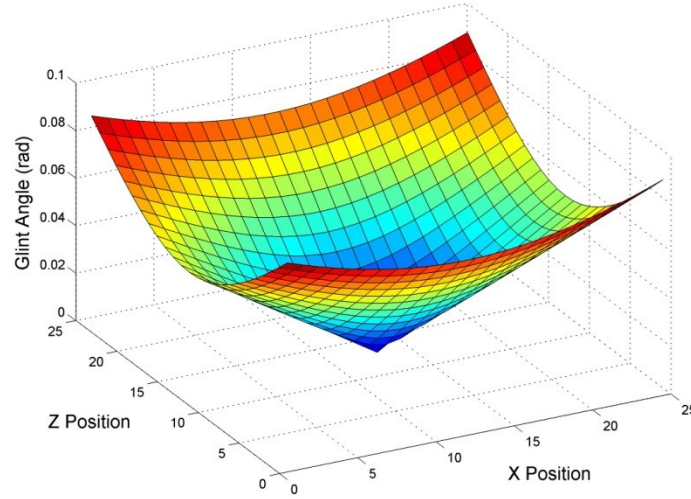
Figure 18. Glint Angle from the center of the wall reflector to every point on the object reflector
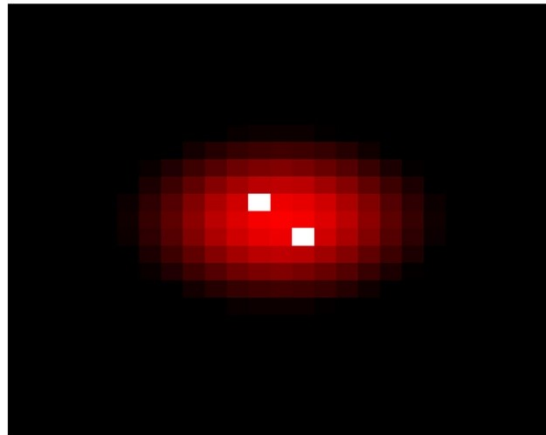
Figure 19. Simulated object irradiance

The object was then placed in the upper left corner of the fixed object frame of reference and beginning from the wall reflector, every possible path to the imaging system was evaluated, *i.e.* from each point on the wall reflector to every point on the object reflector to every point on the imaged reflector, *etc.* The total flux impinging on the lens of the imaging system was summed to simulate the entire image was being used to create the dual or indirect image. The object was then translated horizontally and vertically through each of the possible positions and the process repeated. The dual and indirect images created by the simulation are shown in Figure 20. The full MATLAB code used to create the images can be found in Appendix B.

(a)　　　　　　　　　　　　　(b)

(c)　　　　　　　　　　　　　**(d)**
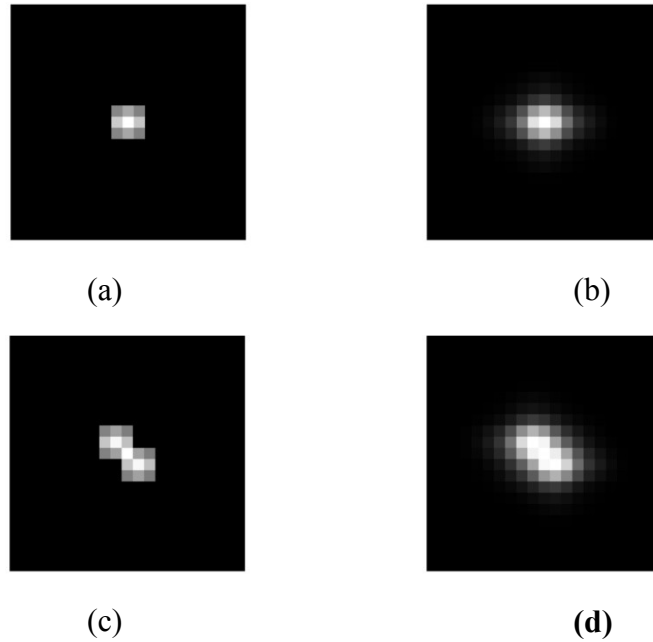
Figure 20. Simulation results of the single square (a) dual and (b) indirect images and the two square (c) dual and (d) indirect images

As stated earlier, Eqs. (70), (83) and (96) suggest that both dual and indirect image quality can be improved through a deconvolution process. The dual images were improved using two of MATLAB's deconvolution algorithms, *deconvlucy* which is based

48

on the Lucy-Richardson (LR) (Richardson, 1972) (Lucy, 1974) method and a blind deconvolution algorithm *deconvblind* (Holmes, 1992) (Gonzalez, Woods, & Eddins, 2004, pp. 176,179). The irradiance of the laser shown in Eq. (97) was used as the PSF (deconvolution kernel) in the *deconvlucy* routine. Because explicit knowledge of the entire setup would be required to fully develop the PSF (deconvolution kernel) for indirect photography, which is unrealistic in a real world scenario, only the blind deconvolution was used on the indirect images. Following each iteration in the deconvolution process, Eq. (36) was used to quantify image quality of each iteration's recovered image. The algorithm was allowed to run for ten iterations, after which there was negligible improvement with each successive iteration. Figure 21 shows the image quality after each iteration of the blind deconvolution algorithm for both of the indirect images.
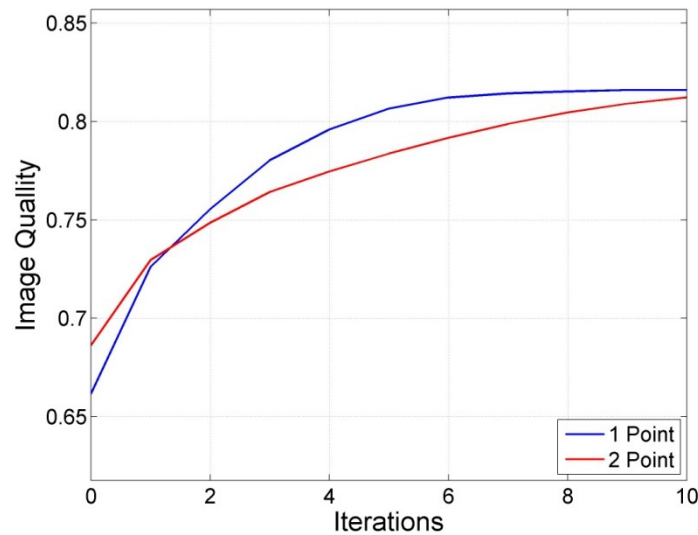
Figure 21. Simulation image quality improvement per deconvolution iteration

Table 4 summarizes the results of the image quality assessment in the original and improved images. Figure 22 shows the recovered images after the blind deconvolution process. (Note: Because there was no discernable difference between the recovered images using the LR or blind deconvolution algorithm, only those recovered using the blind deconvolution are shown.)

Table 4. Simulation image quality[2]

	Raw Image	LR Deconv	Blind Deconv
1 point dual image	0.8326	0.9999	0.9998
1 point indirect image	0.6616	n/a	0.8160
2 point dual image	0.8326	0.9999	0.9989
2 point indirect image	0.6863	n/a	0.8150

(a)   (b)

(c)   (d)
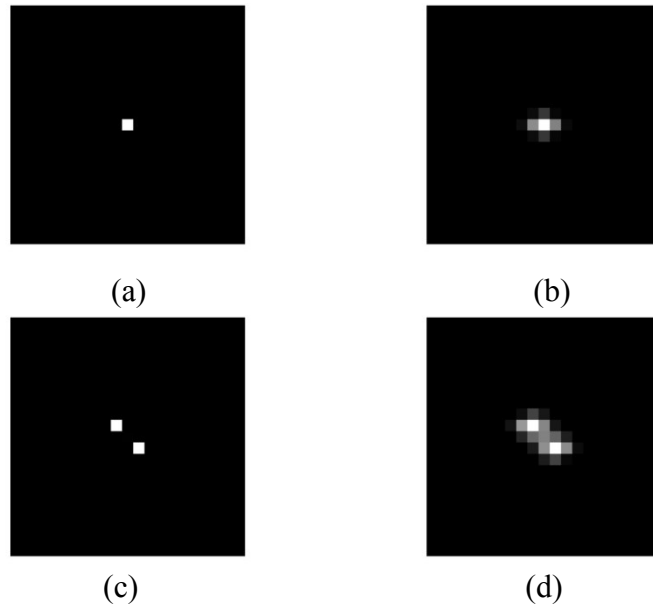
Figure 22. Simulation results following the blind deconvolution of the single-square (a) dual and (b) indirect images, and the two-square (c) dual and (d) indirect images

---

[2] The image quality calculations were carried out to four significant digits to show the difference between the LR and the blind deconvolutions. In a real world scenario, the noise floor will be the determining factor on the number of significant digits the equations will support.

While somewhat limited in scope due to computer processing speed and memory requirements, the above results verify that the image quality of both dual and indirect images as modeled by Eqs. (67) and (78) can be improved through deconvolution. It also validated the small angle-approximation of dual photography and verified Eq. (96) could be used to improve the image quality of dual images if the irradiance in the object frame of reference is known. Due to time constraints, a full scale/higher fidelity version of the simulation was not pursued, opting instead to begin a physical experiment. The following section describes the 1-D experiment and its results in detail.

1-D Experimental Setup

The dual and indirect photography 1-D experiments were set up in accordance with Figure 23 (a) and (b), respectively, where a 633nm HeNe laser is used as the illumination source. The imaged reflectors, and wall reflector for the indirect images, were polished aluminum plates that had been finished in one of three ways: (1) spray-painted semi-gloss white paint, (2) spray-painted with a flat white paint or (3) polished with 600-grit sandpaper and left unpainted. The BRDF of each of the reflectors was measured using AFIT's CASI instrument and the respective measurements can be found in Appendix C. The object reflector, which provides the phase function dependence, f_{ph}, was also a polished aluminum plate with a flat white finish similar to finish of the second set of reflectors.

Six sinusoidal slides with spatial frequencies from 0.1 to 3.0 cycles/mm (0.02 to 0.6 cycles/mrad with respect to the wall-reflector-to-slide-distance) were used as the object to create the dual and indirect images. (See Table 5 for a complete list of slides

used.) A computer-controlled translation stage moved the slide through the path of the illumination to create the $(\bar{x}' - \bar{x})$ dependence for each image. The complete laboratory set up is shown in Figure 24.

Table 5. 1-D sinusoidal slides

	Spatial Frequency	
slide	cycles/mm	cycles/mrad
Slide 1	0.1	0.02
Slide 2	0.2	0.04
Slide 3	0.5	0.10
Slide 4	1.0	0.20
Slide 5	2.0	0.40
Slide 6	3.0	0.60

1,000 data images were taken with the sinusoidal slide translated horizontally 0.1mm between each image.   These data images were then used to create the dual or indirect image, depending on the setup, in accordance with the dual photography algorithm described in the background section of this document. Figure 25 shows the 0.1 cycle/mm (0.02 cycle/mrad) slide being illuminated by the reflection from the semi-gloss wall reflector, *i.e.* when creating an indirect image.

Representative images recorded by the camera through a non-transmissive and transmissive portion of the 0.1 cycles/ mm slide (0.02 cycles/ mrad) dual image are shown in Figure 26 (a) and (b), respectively.
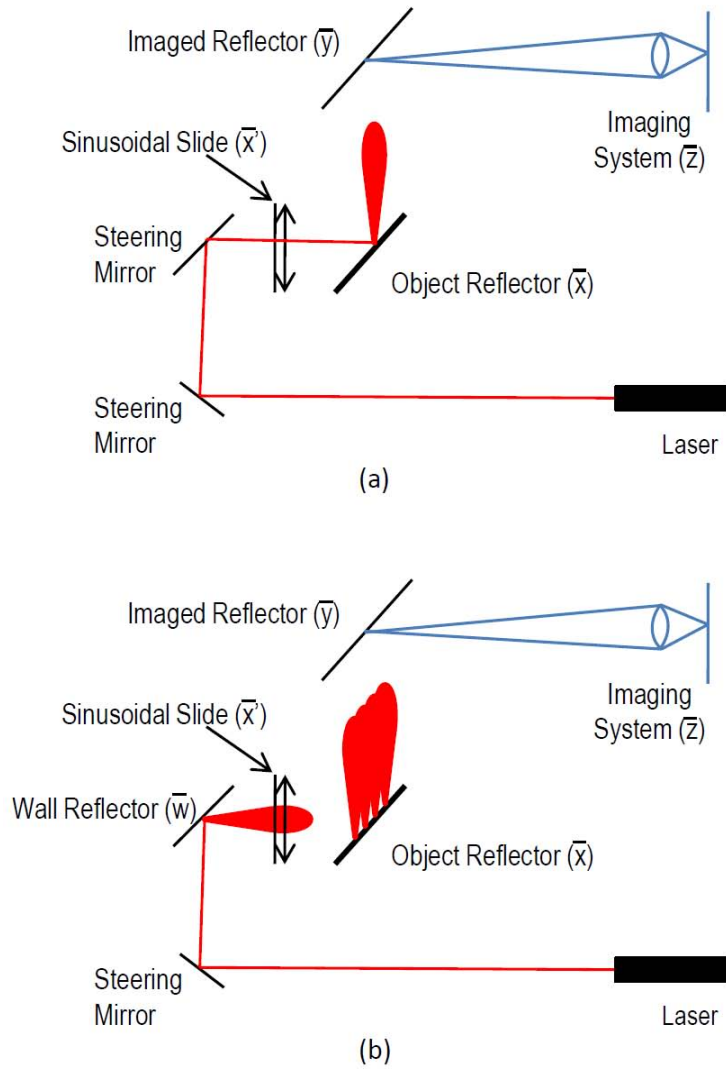
Figure 23. 1-D (a) dual photography and (b) indirect photography setup
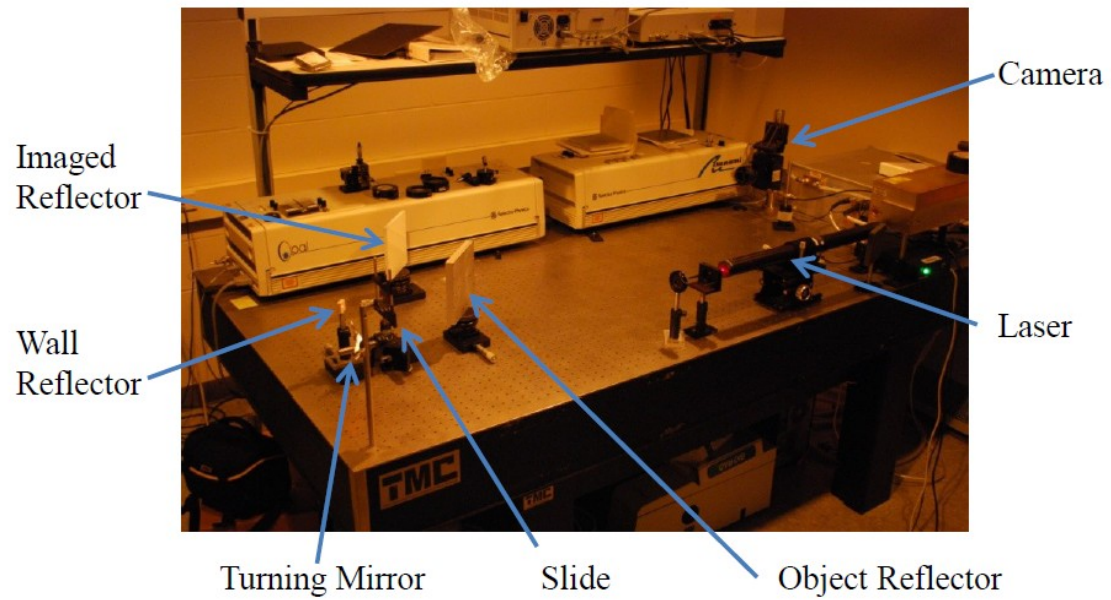
Figure 24. 1-D Laboratory setup
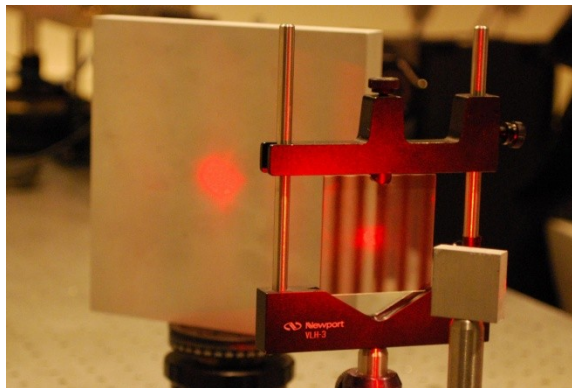
Figure 25. Indirect illumination on the 0.1 cycles/mm (0.02 cycles/mrad) slide
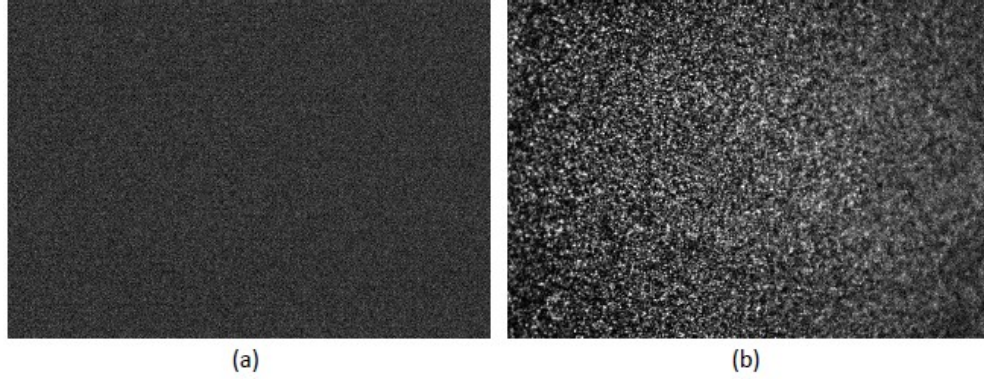
Figure 26. Data image of 0.1 cycles/mm slide through (a) a non-transmissive and (b) transmissive portion of the slide

To improve the signal-to-noise ratio, the entire image was used to create each of the dual or indirect images. The average intensity of each digital image was used as the total irradiance on the lens for each position, x', as represented by Eqs. (67) and (77) for the dual and indirect images, respectively.

Beam View Analyzer by COHERENT® was used to obtain the cross-sectional power distribution of the laser beam used as the illumination source. This analysis was used to create an estimation of the object irradiance, E_{obj}, as a function of position which was, in-turn, used as the deconvolution kernel for MATLAB's LR deconvolution algorithm. The dual images created with the semi-gloss reflector were then improved using the LR and the blind deconvolution algorithms. The results of these deconvolutions for the 0.1 cycles/mm slide are shown in Figure 27 while an expanded view of the 1.0 cycles/mm slide dual image and deconvolutions are shown in Figure 28. Based on the high quality match of the two deconvolution techniques, and for consistency, further analysis will be done with only the blind deconvolution algorithm.

Following the above analysis, both the dual and indirect images were improved using MATLAB's blind deconvolution algorithm. After the creation of the improved images, Fourier analysis was accomplished on all of the images (dual, indirect and improved) to assess the amount of energy in the fundamental frequency of each of the corresponding slides. Figure 29-31 show the following images for the semi-gloss, flat white and unpainted reflectors, respectively, all for the 0.1 cycles/mm (0.02 cycles/mrad) (a) dual images; (c) indirect images; (e) overlay of the dual and deconvolved images; and (g) overlay of the indirect and deconvolved images; (b), (d), (f), and (h) are the Fourier transforms of (a), (c), (e), and (g), respectively. The complete set of dual and indirect images, as well as the corresponding plots of the Fourier transforms, can be found in Appendices D-F for the semi-gloss, flat white and unpainted reflectors.
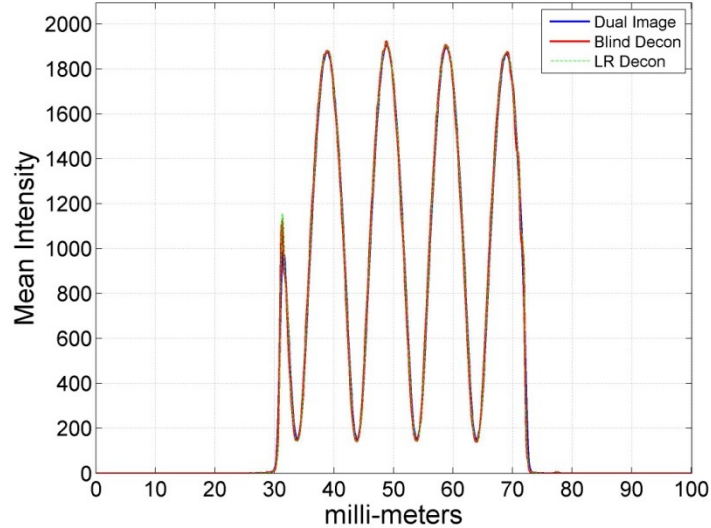
Figure 27. 0.1 cycles/mm slide dual, and dual with LR, and blind deconvolutions
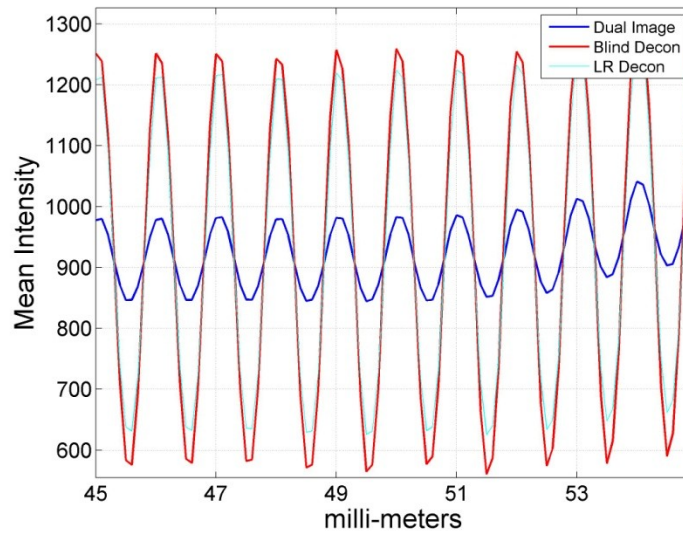
Figure 28. Expanded 1.0 cycles/mm slide dual, and dual LR, and blind deconvolutions

As previously stated the modulation transfer function (MTF) is one technique of quantifying an imaging system's ability to transfer frequency content from the object of interest to the final image. Therefore, the transfer of information, *i.e.* spatial frequencies, for the dual, indirect and deconvolved images can be quantified by the MTF described by Eq. (34). For the purposes of this analysis, the energy corresponding to the fundamental frequency of each slide was normalized to the lowest frequency dual image (0.1 cycles/mm or 0.02 cycles/mrad slide) and then used to create the MTF. The experimental MTF for the semi-gloss, flat white and unpainted reflectors are shown in Figure 32-34.

The 1-D experiment was set up with three goals in mind. First was to validate the theoretical model of indirect photography and insure spatial information could be recovered from an indirect image created from wall and imaged reflectors with different reflection characteristics. Second was to verify Eqs. (70) and (83) could be used to improve the image quality of both the dual and indirect images. The final goal was verify

the small-angle approximation of dual photography, and therefore, Eq. (96) could be used to improve the image quality of the dual image.

The creation of the dual/indirect images and subsequent deconvolutions as shown in the MTFs of Figure 32 -34 verify that the frequency content of the slides, both visually and quantitative, could be recovered and that the deconvolution would improve the image quality. The small-angle approximation was also confirmed by a direct comparison of a blind deconvolution and a LR deconvolution using the laser profile as the kernel for the deconvolution. Having verified the general assumptions and validated the radiometric theory in 1-D, the next set of experiments expanded the experiment to 2-D.

2-Dimensional Setup

With the final goal of a real world setup with the illumination source and camera co-located to image a 2-D object, an intermediary step of a 2-D object similar to the 1-D experiment was conducted. The sinusoidal slides and object reflector were replaced by a 2-D object in the place of the object reflector (see Figure 35).
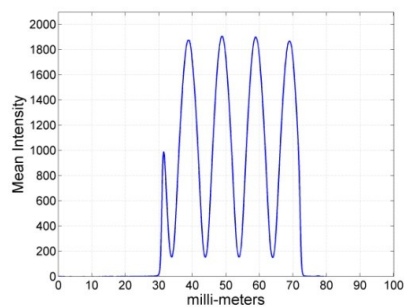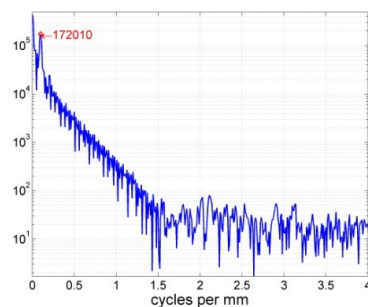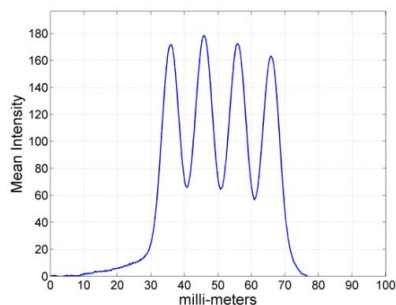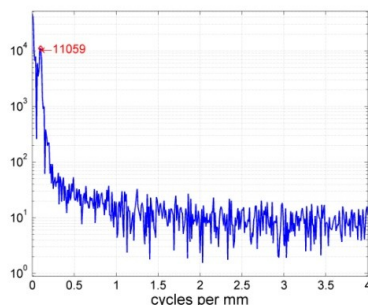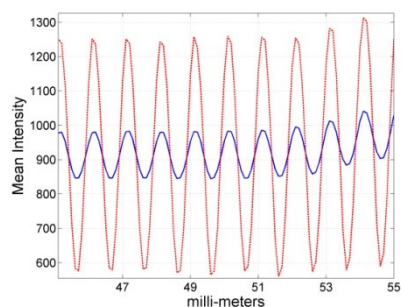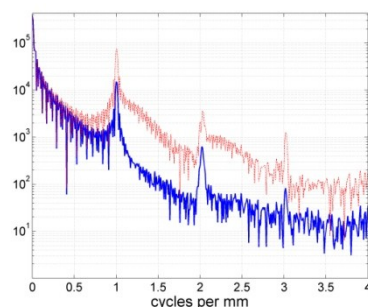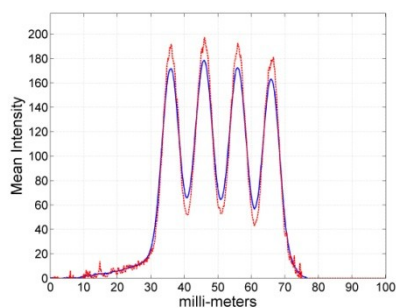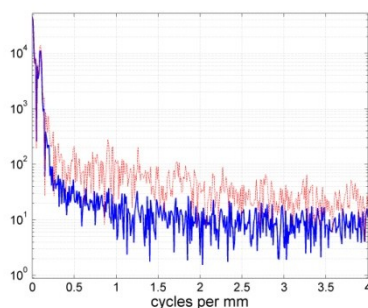
Figure 29. Semi-gloss reflector 0.1 cycles/mm (a) dual image and (b) Fourier transform (c) indirect image, (d) Fourier transform (e) overlay of 1.0 cycles/mm dual and improved image and (f) Fourier transform (g) overlay 0.1 cycles/mm indirect and improved image and (h) Fourier transforms
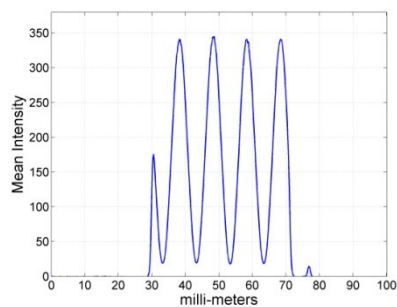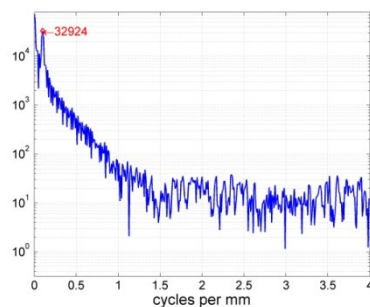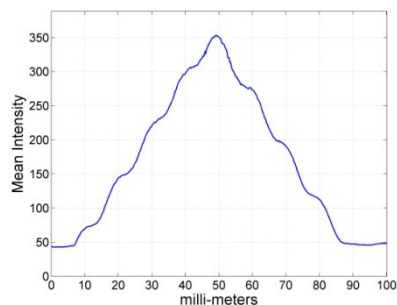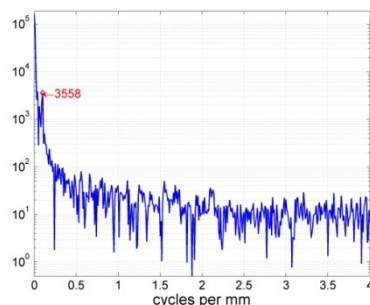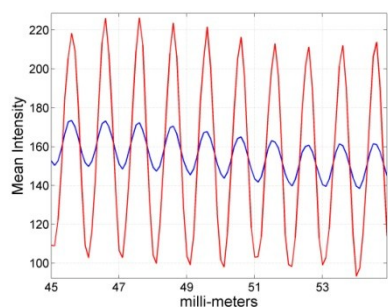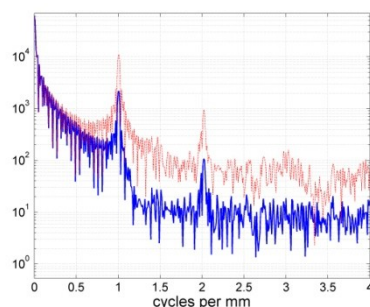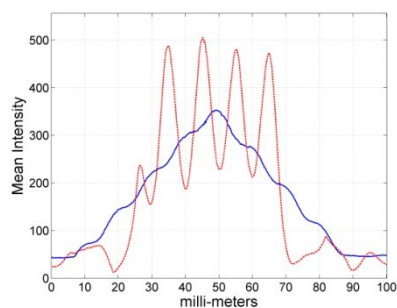
Figure 30. Flat white reflector 0.1 cycles/mm (a) dual image and (b) Fourier transform (c) indirect image, (d) Fourier transform (e) overlay of 1.0 cycles/mm dual and improved image and (f) Fourier transform (g) overlay 0.1 cycles/mm indirect and improved image and (h) Fourier transforms

(a)

(b)

(c)

(d)

(e)

(f)

(g)

(f)
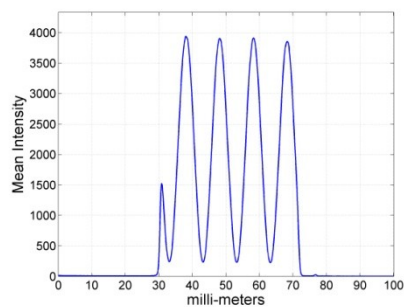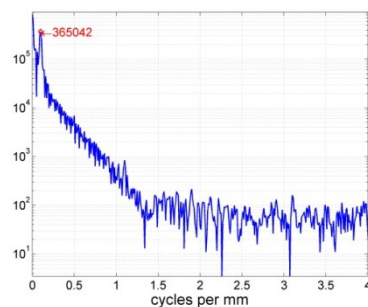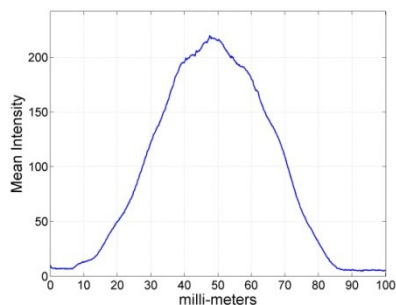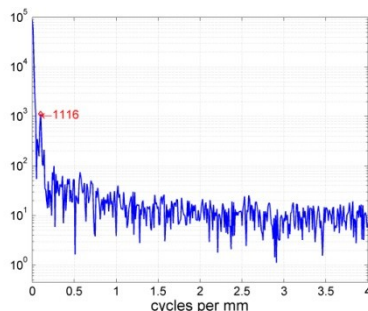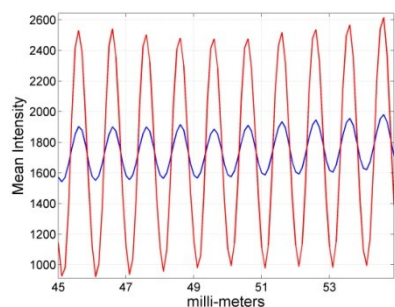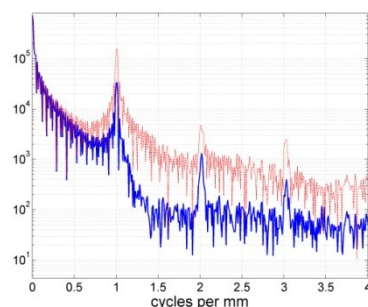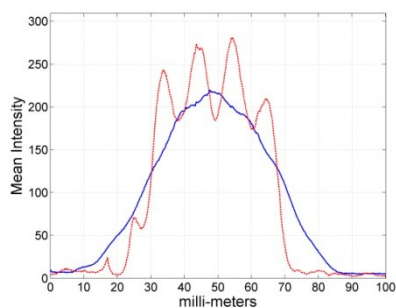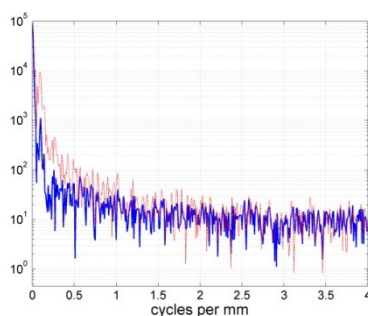
Figure 31. Unpainted reflector 0.1 cycles/mm (a) dual image and (b) Fourier transform (c) indirect image, (d) Fourier transform (e) overlay of 1.0 cycles/mm dual and improved image and (f) Fourier transform (g) overlay 0.1 cycles/mm indirect and improved image and (h) Fourier transforms

61
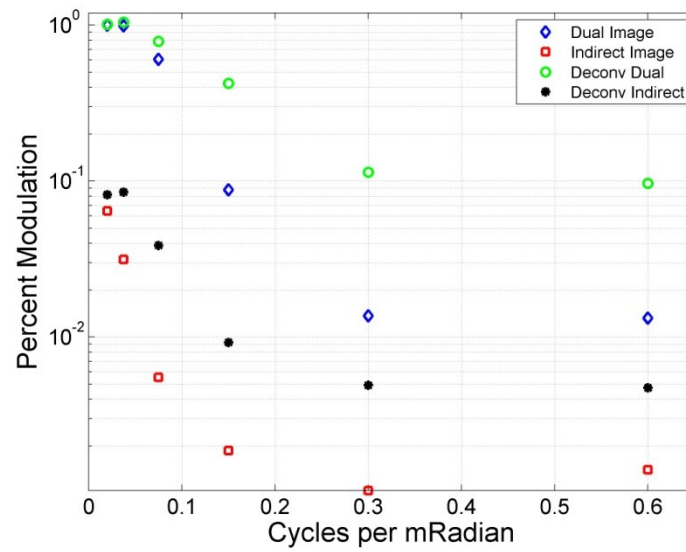
Figure 32. Semi-gloss reflector 1-D experimental MTF
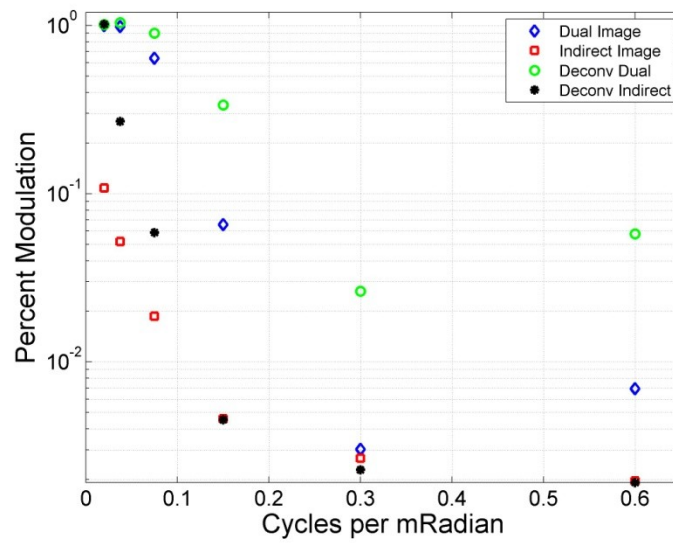
Figure 33. Flat white reflector 1-D experimental MTF
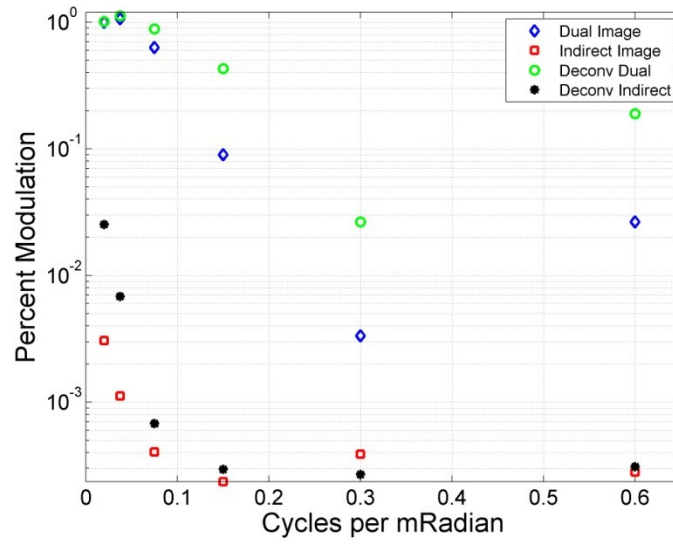
Figure 34. Unpainted reflector 1-D experimental MTF
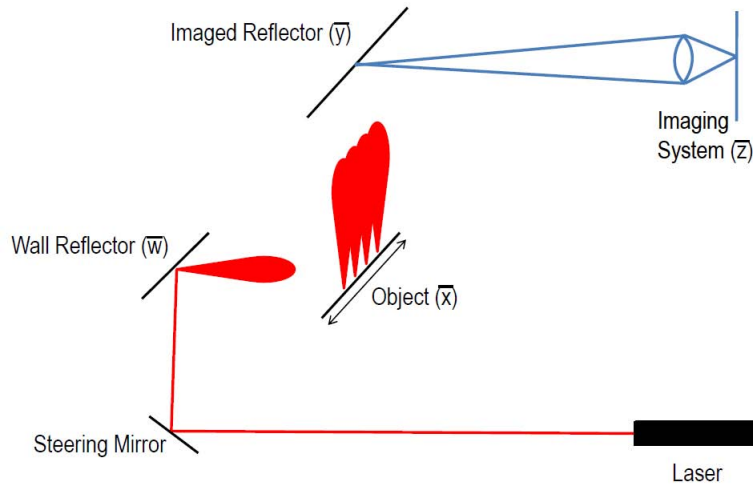
Figure 35. 2-D indirect photography experimental setup

Four objects were used to create the 2-D indirect images: (1) two white 1-cm squares (each square subtending 24 mrad with respect to the wall-to-object distance) separated by 1 cm both horizontally and vertically; (2) two white 5-mm squares (12

mrad) separated by 5 mm both horizontally and vertically; (3) two white 2-mm squares (4.8 mrad) separated by 2 mm both horizontally and vertically; (4) a white 25-mm (60 mrad) square with a 5-mm (12 mrad) square cut from the center. The objects were created from white cardstock on a flat black poster board background. Figure 36 shows object 2 and object 4. The semi-gloss wall and imaged reflectors from the 1-D experiment were used.

(a)   (b)

Figure 36. 2-D (a) object 2 and (b) object 4

To create the indirect images of objects 1, 2 and 3, 2601 digital images in a 51x51 pattern were acquired with the object translated horizontally *and/or* vertically one fifth of the square size between each data image, *i.e.* 2-mm movement for object 1, 1-mm movement for object 2. Three indirect images were created of object 4: (1) 2601 digital images in a 51x51 pattern with the object translated 1-mm horizontally *and/or* vertically between each data image; (2) 441 digital photographs in a 21x21 pattern with 2.5-mm movement between data images; and (3) 121 digital images in an 11x11 pattern with 5-mm movement between each data image, which corresponds to the Nyquist frequency for object 4. For reference, Figure 37 shows an overlay of the reflected laser spot and object 2, and Figure 38 shows the complete 2-D laboratory setup.
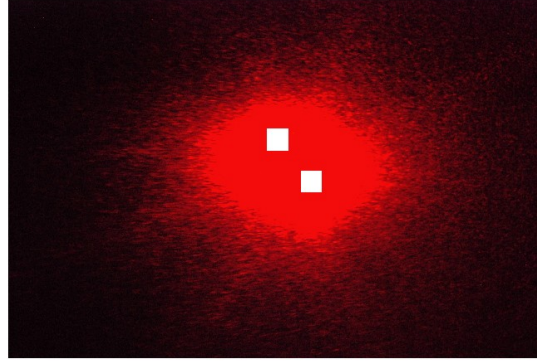
Figure 37. Overlay of reflected laser spot and object 2
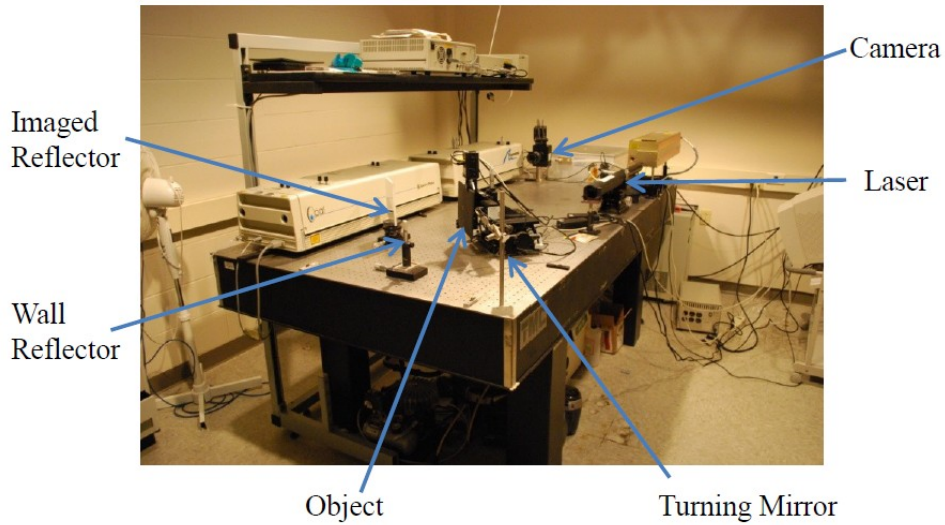
Figure 38. 2-D laboratory setup

As with the 1-D dual and indirect images, to improve the signal-to-noise ratio, the entire digital image was used to create the raw indirect image. Initially, the average intensity of the image's pixels was used to form the intensity on the imaging system for each position, $\bar{x}'$, as represented by Eq. (83). Figure 39 shows the raw indirect images of objects 1, 2 and 3 and the indirect images of object 4 created with 2601, 441, and 121 images.

65
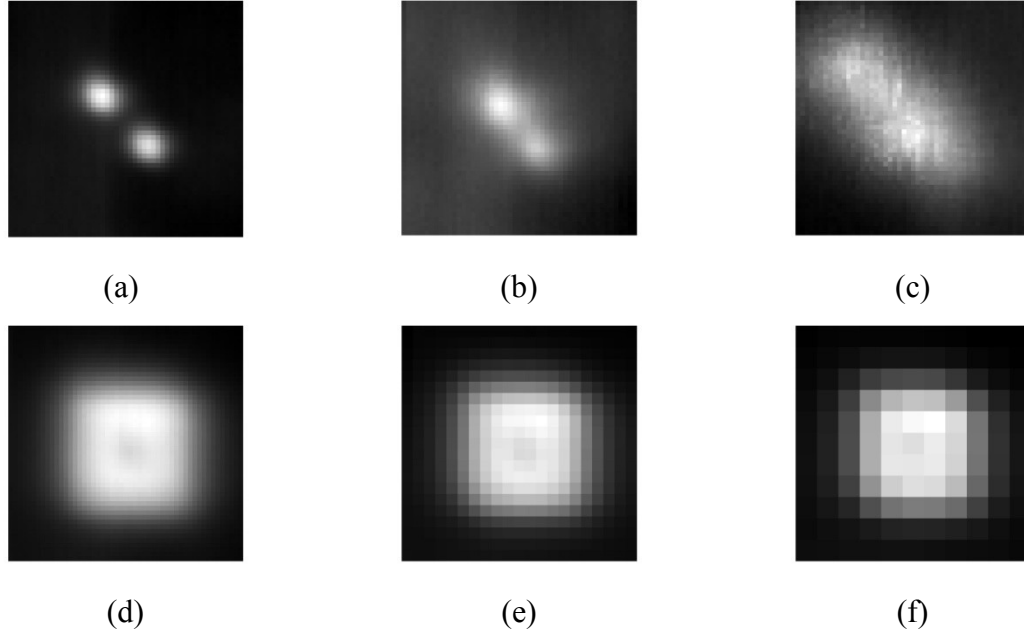
Figure 39. Unimproved indirect images of (a) object 1, (b) object 2, (c) object 3, and object 4's (d) 51x51 image, (e) 21x21 image and (f) 11x11 image

Image quality was then improved in two parts. The first consisted of creating a cumulative histogram of each recorded image, assigning to each position, $\bar{x}'$, the intensity corresponding to the 99.5th percentile of the cumulative histogram, *i.e.* the intensity at which 99.5% of the pixels are below that point and 0.5% are above that point. The subsequent image was then improved using MATLAB's blind deconvolution command *deconvblind*. The initial point spread function for the deconvolution was a block of ones one pixel less than the image size, *i.e.* 50x50 for the 51x51 image, 20x20 for the 21x21 image, *etc.* The deconvolution was allowed to run from four to 40 iterations in blocks of 4 iterations. Figure 40 shows the averaged 51x51 indirect image of object four deconvolved using four, eight, 16, 24, 32 and 40 iterations. Figure 41 shows the corresponding cumulative 51x51 indirect images of object 4.

(a)   (b)   (c)

(d)   (e)   (f)
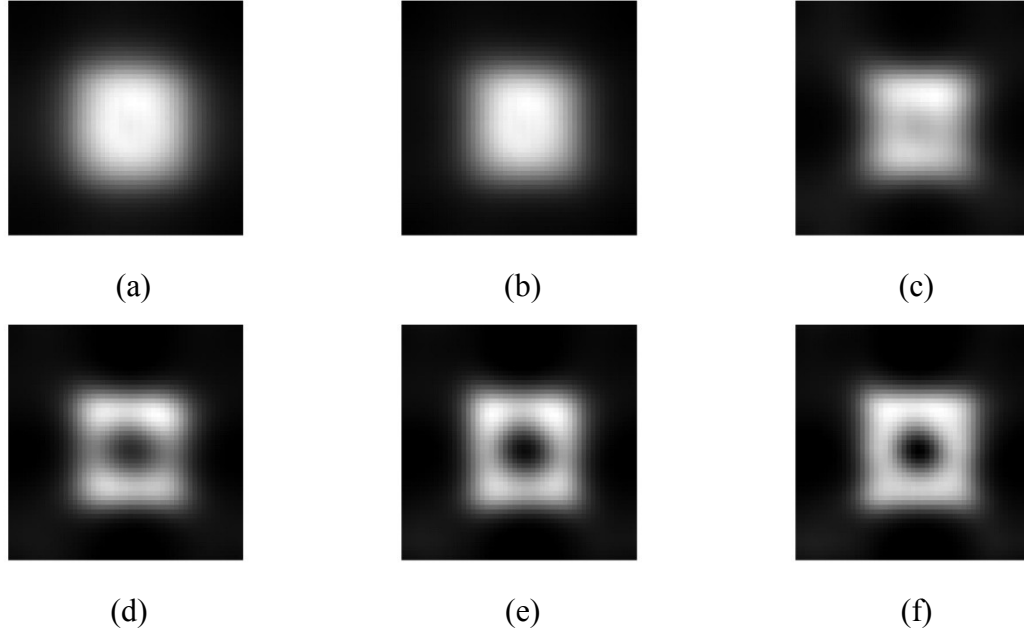
Figure 40. 51x51 averaged object 4 indirect image deconvolved for (a) 4 (b) 8 (c) 16 (d) 24 (e) 32 and (f) 40 iterations

Following each block of four iterations in the deconvolution process, image quality for each image was assessed using Eq. (36). Because it was not guaranteed the object would be in the exact center of the indirect image, every possible position of the object was evaluated and the estimated position of the object was assigned where the image quality was the highest. Figure 42 shows the image quality for every four iterations of the deconvolution process for the 51x51 cumulative indirect image of object 4, while Figure 43 shows the highest quality image produced by the deconvolution process and the overlay of the ideal image.

(a)   (b)   (c)

(d)   (e)   (f)
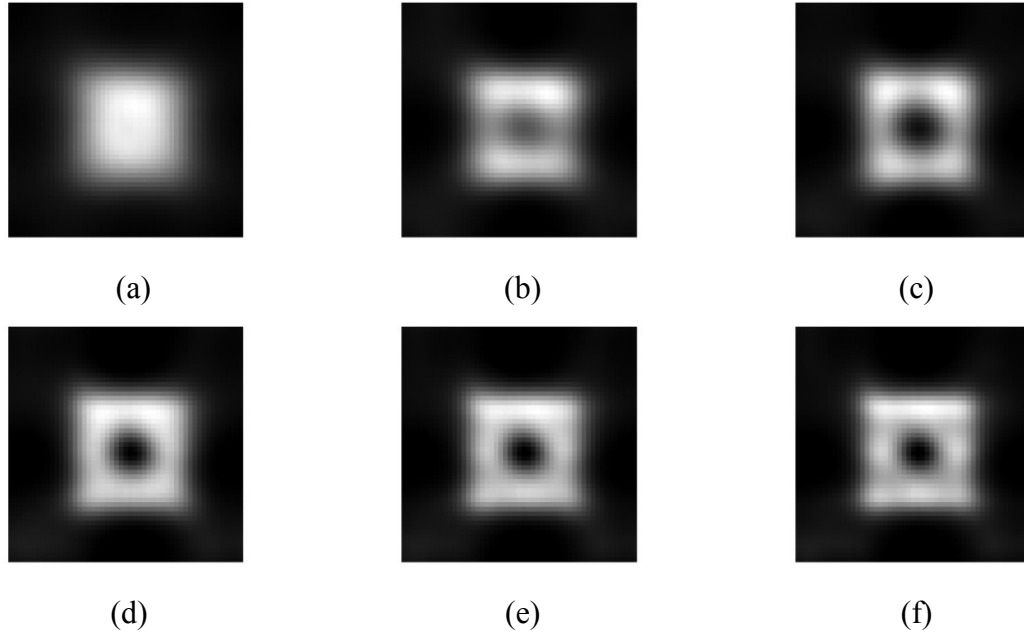
Figure 41. 51x51 cumulative object 4 indirect image deconvolved (a) 4 (b) 8 (c) 16 (d) 24 (e) 32 and (f) 40 iterations

The same average and cumulative techniques and deconvolution processes were accomplished for each of the unimproved indirect images seen in Figure 39.   The recovered images with the highest image quality for objects 1, 2 and 3 and the three indirect images of object 4 are shown in Figure 44.
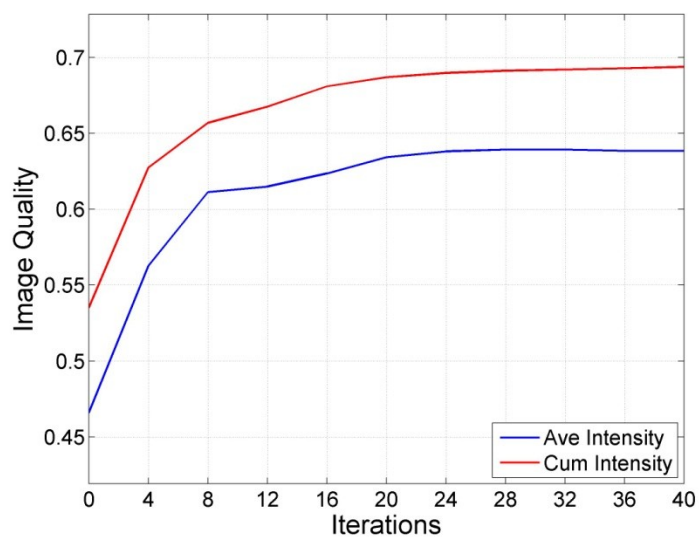
Figure 42. Image quality as a function of number of deconvolution iterations for 51x51 indirect image of object 4

(a)   (b)
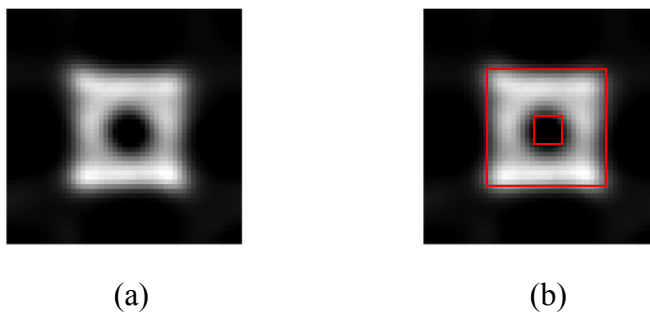
Figure 43. (a) Best recovered (deconvolved) cumulative image of object 4 and (b) the same image with ideal image of object 4 overlaid.
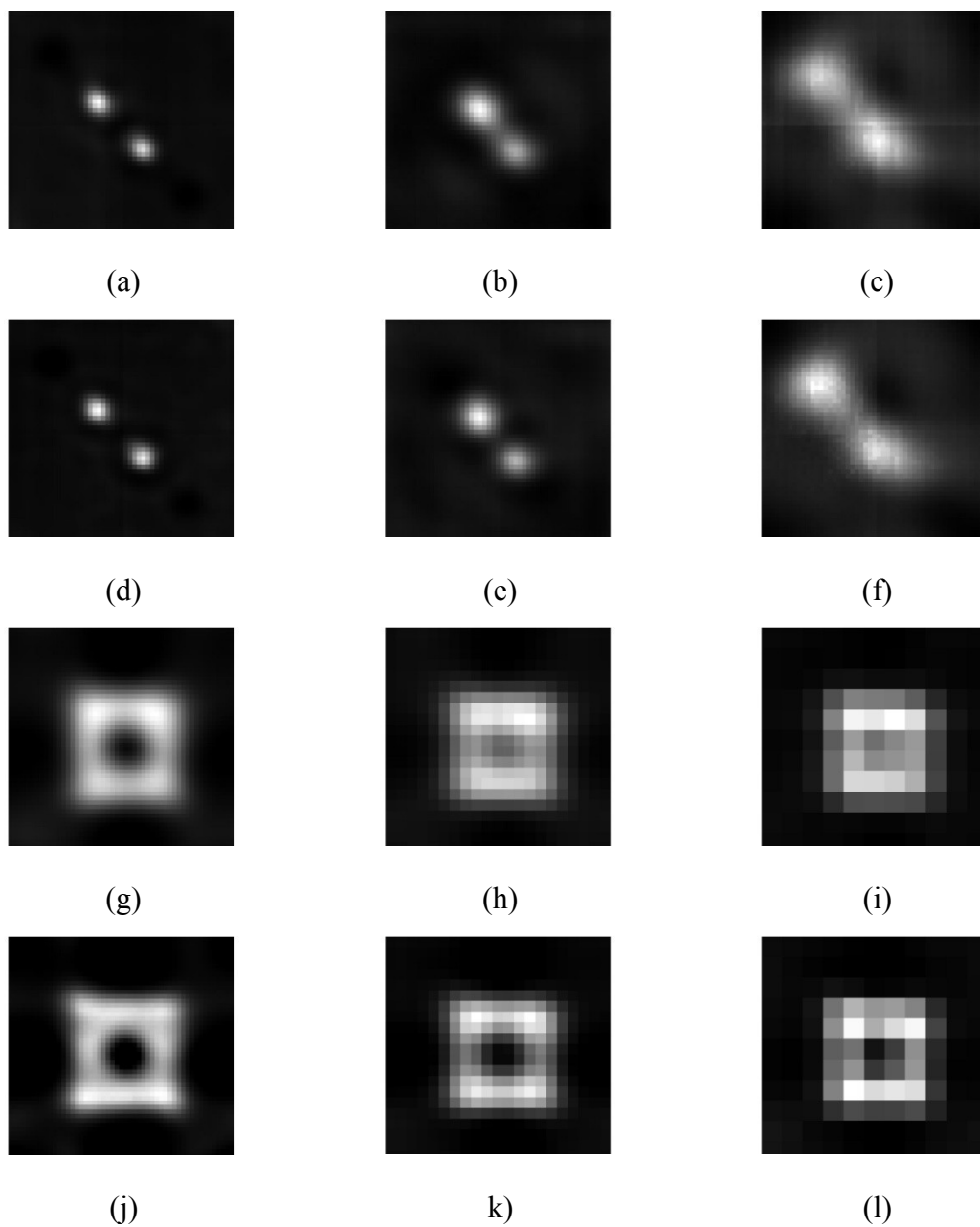
Figure 44. Recovered averaged indirect images of (a) object 1, (b) object 2 and (c) object 3. Cumulative indirect images of (d) object 1, (e) object 2 and (f) object 3. Averaged (g) 51x51, (h) 21x21 and (i) 11x11 and cumulative (j) 51x51, (k) 21x21 and (l) 11x11 indirect images of object 4.

The image quality analysis of objects 1, 2 and 3 can be converted to an MTF by considering the size of the square used to make each image to be a half cycle. Figure 45 shows the MTF for unimproved average and cumulative indirect images and the corresponding deconvolved indirect images of objects 1, 2 and 3.
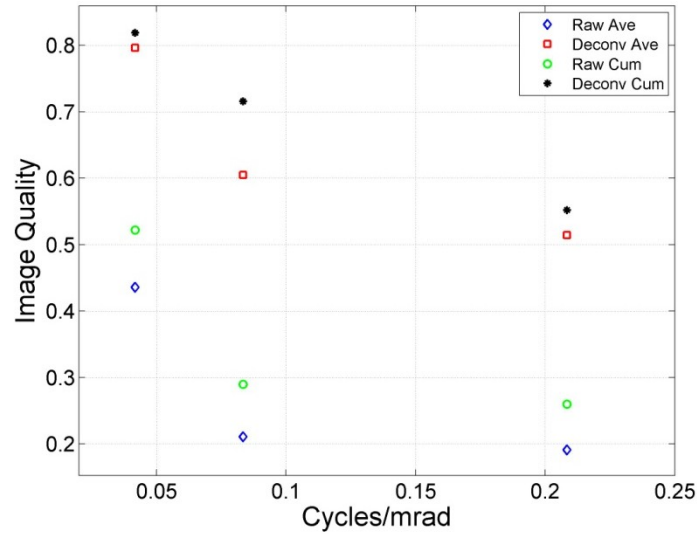
Figure 45. MTF of unimproved and deconvolved images of objects 1, 2 and 3.

While the images of object 4 do not lend themselves to a traditional MTF, *i.e.* percent modulation or image quality *v.* cycles/(m)rad, they can be used to determine the image quality *v.* step size used in comparison to the object feature size. To that end, the image quality of the three indirect images and the associated recovered images of object 4 were plotted as function of ratio of the step size to feature size, *i.e.* 1-mm step size and 5-mm square feature on object 4 yields the ratio 0.2. Figure 46 shows the results of the analysis for object 4's images.

Indirect images of object 2 were accomplished in a 21x21 pattern using a 2.5-mm step size and an 11x11 pattern using a 5-mm step size. As with the 11x11 image of

object 4, the 11x11 image of object 2 represents the Nyquist frequency of object 2. The

resultant plot of image quality *v.* the ratio of step size per feature size is shown in Figure

47.
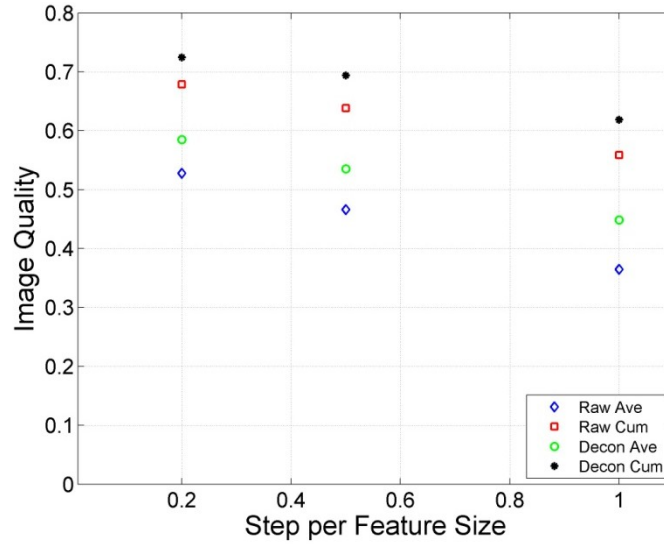
Figure 46. Object 4 image quality v. step size results for 51x51, 21x21 and 11x11 images

The goal of the 2-D setup was to validate that indirect photography could be

expanded from the 1-D sinusoidal slides with well-defined frequencies to more

representative 2-D objects. Figure 44 shows the recovered images can be recognized;

even the 2-mm (4.8 cycles/mrad) squares can be recognized as separate squares after the

deconvolution. More importantly, Figure 45 shows the image quality can be improved

by a blind deconvolution.
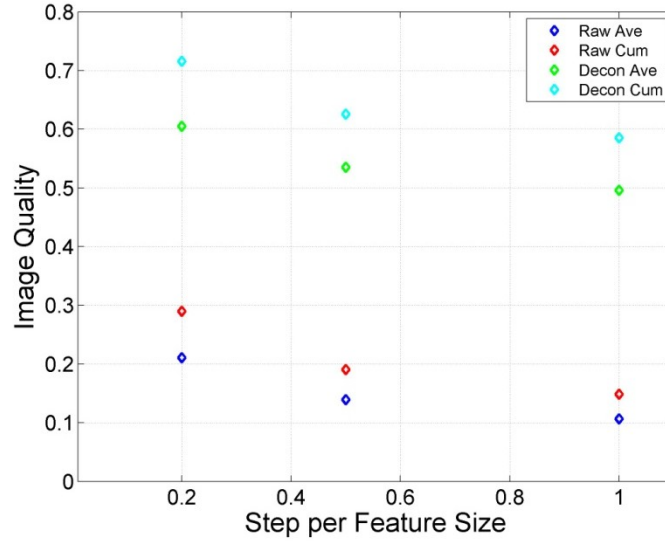
Figure 47. Object 2 image quality v. step size results for 51x51, 21x21 and 11x11 images

While the experimental setup was consistent with the setup used in the radiometric model, in order to be operationally significant, the camera and the laser must be co-located. The next section describes the results of co-locating the camera and the laser.

Real-world Setup

Following the completion of the 2-D experimental setup, the camera was co-located with the laser creating a real-world setup. Figure 48 shows the experimental setup and Figure 49 shows the real-world laboratory setup. While the separated wall reflector was used, it was placed parallel to the imaged reflector to simulate they were part of the same wall.
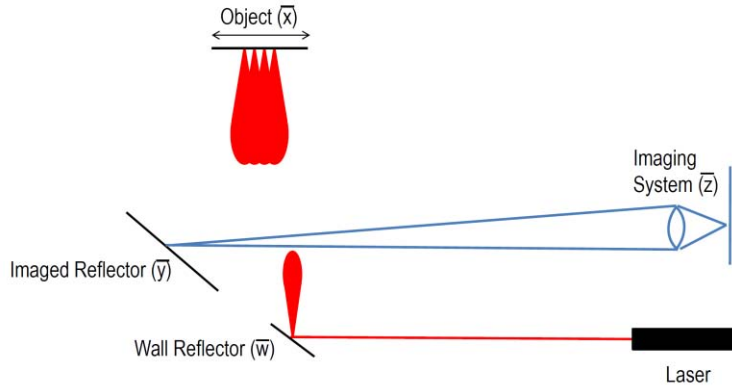
Figure 48. Real world experimental setup

Initially, object 2 from the 2-D experiment described in the previous section was used to test the real-world configuration. Figure 50 (a) shows the dual image of object 2, (b) shows the indirect image and (c) shows the deconvolved image. The indirect image (b) shows a banding on the left half of the image which carries over to the deconvolved image. It was determined that the banding was caused by the translation stage. As the object was translated to the left, the black cardstock covered the corner of the translation stage and prevented the reflections from the translation stage from being imaged by the camera off the imaged reflector. Figure 51 shows the indirect image (a) and deconvolved image (b) with the block in place.

Following confirmation the 2-D setup could be transitioned to a real-world setup, the objects were changed to playing cards. Figure 52 shows the indirect illumination of the five of clubs. Raw indirect images of the five of clubs were created at the following resolutions: (1) 96x63, (2) 47x31, (3) 23x15, (4) 11x7 and (5) 5x3. Additionally, a 5x3 dual image was created (see Figure 53).
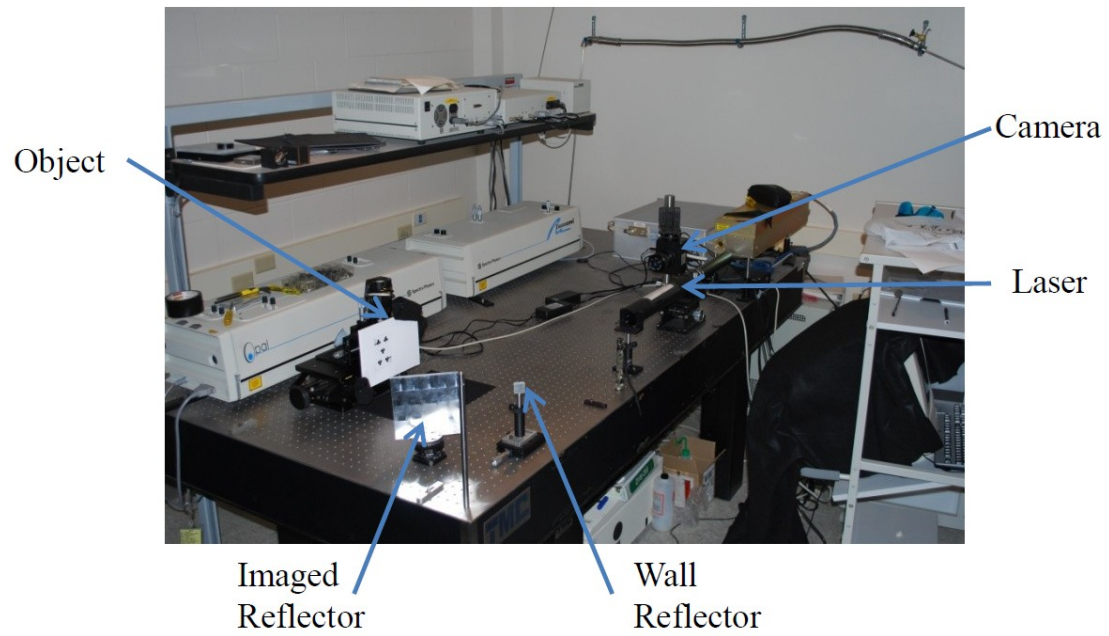
Figure 49. Real world laboratory setup

(a)   (b)   (c)
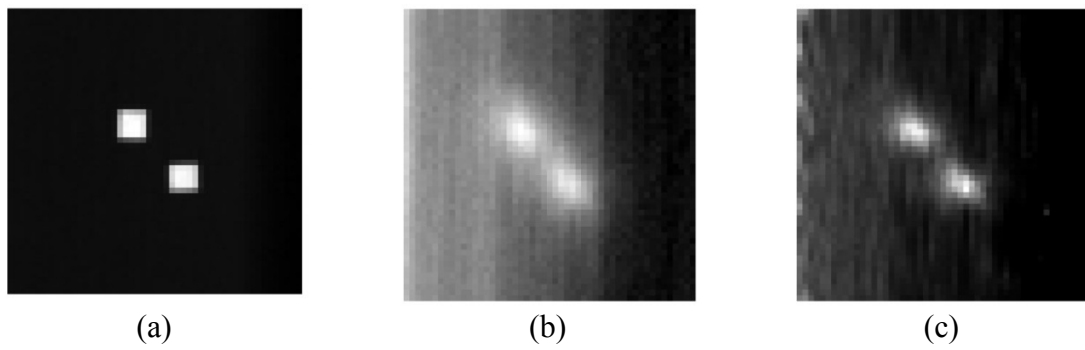
Figure 50. Object 2 real world setup results

(a)   (b)
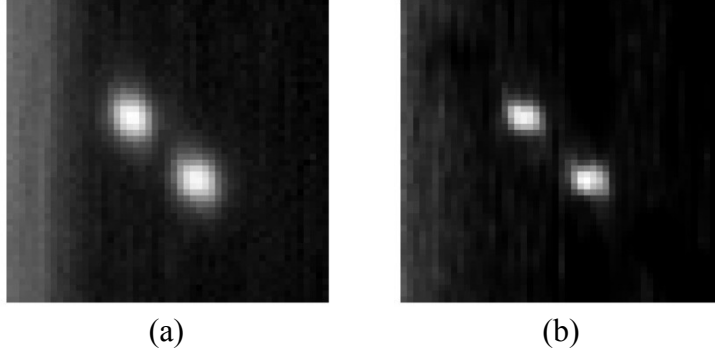
Figure 51. Real-world (a) raw and (b) improved indirect images of object 1 with the translation stage covered
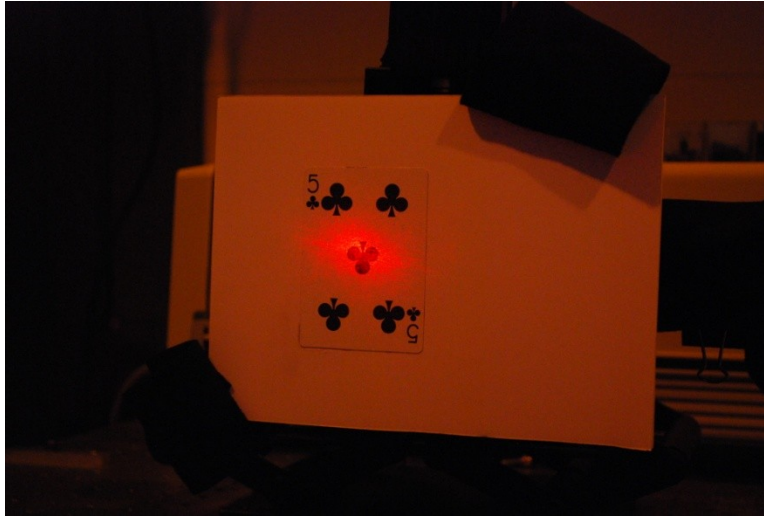
Figure 52. Indirect illumination of the five of clubs

At this point, the goal of the experiment was to identify the value of the playing card, *i.e.* ace through king, but not necessarily the suit. To that end, the image quality of the 11x7 and 5x3 indirect images were computed as though they were the ace through eight. (Note: The 7 is the only card that is not horizontally symmetric; therefore, whether the pip is in the upper or lower position must be tested and reported, *i.e.* 7U and 7L). The resultant image qualities are reported in Table 6. Based on the results presented in the previous section, the image quality should improve as the step size to feature size

increases (see Figure 46 and 47). Given that the five of clubs was correctly identified using the 5x3 indirect image, the next set of experiments will be used to try to correctly identify the ace through eight using 5x3 indirect images.

(a)   (b)   (c)

(d)   (e)   (f)
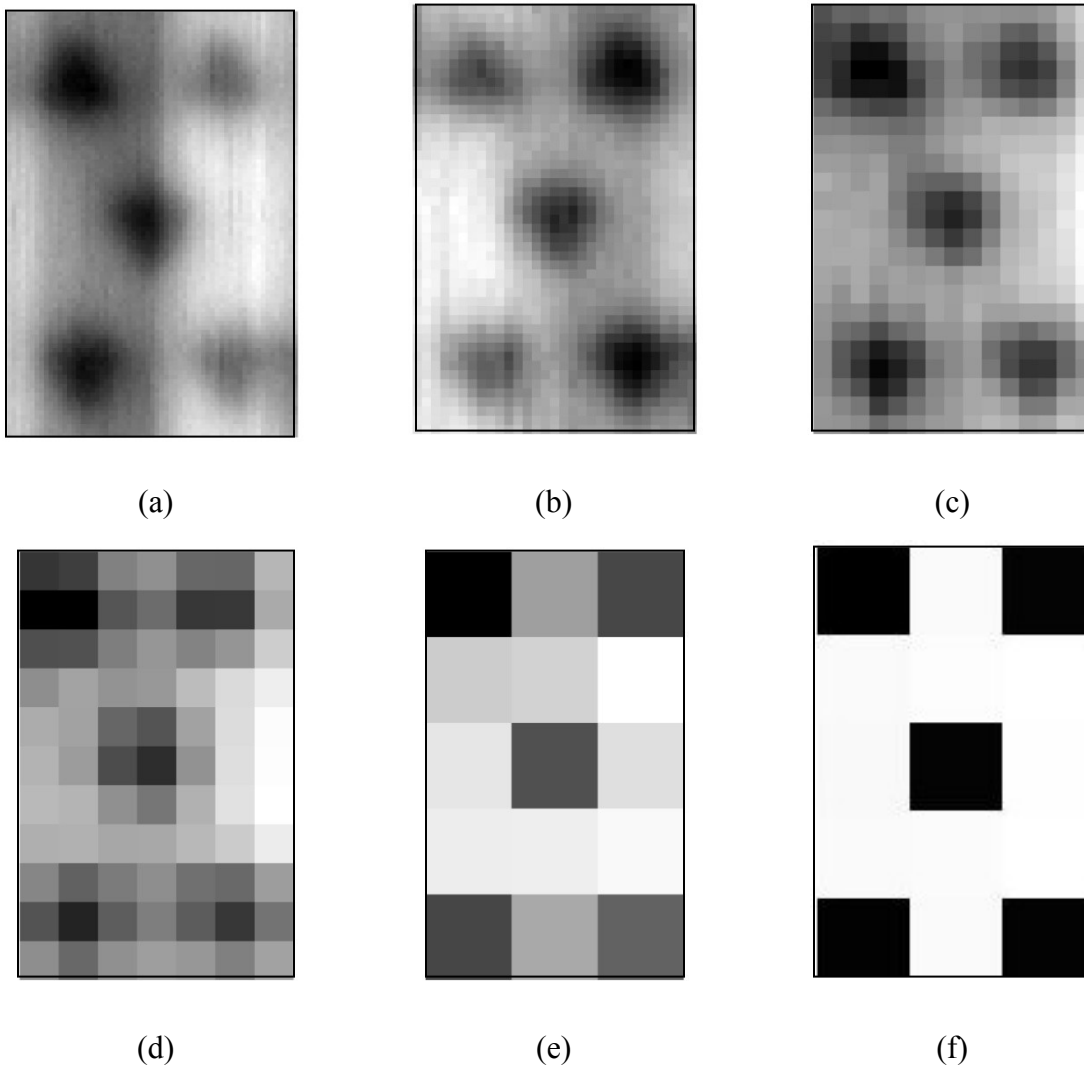
Figure 53. 5 of clubs indirect images: (a) 95x63, (b) 47x31, (c) 23x15, (d) 11x7, (e) 5x3 and (f) 5x3 dual image

Because the process of creating indirect images is both data and time intensive, using the lowest resolution possible will increase the operational utility of an indirect imaging system. To that end, indirect images of the ace of clubs through the eight of

clubs were created with a 5x3 resolution (see Figure 54). Following the creation of the indirect images, the image quality of each image was calculated for each of the possible cards. The highest image qualities for each indirect image are identified in red. In every case, the correct card was identified.

Table 6. Five of clubs indirect image quality

	Mask								
Res	Ace	2	3	4	5	6	7L	7U	8
5x3	0.016	0.001	0.007	0.026	0.027	0.015	0.011	0.012	0.009
11x7	0.021	0.012	0.016	0.032	0.034	0.016	0.012	0.013	0.014

Table 7. Card indirect image selection criteria

	Mask								
Card	Ace	2	3	4	5	6	7L	7U	8
Ace	0.032	-0.005	0.008	-0.004	0.004	-0.002	-0.002	-0.002	-0.002
2	-0.009	0.032	0.019	0.003	0.0002	-0.003	-0.004	-0.003	-0.005
3	0.022	0.024	0.026	-0.001	0.005	-0.003	-0.005	-0.005	-0.007
4	-0.015	0.004	-0.003	0.032	0.024	0.018	0.014	0.015	0.011
5	0.016	0.001	0.007	0.026	0.027	0.015	0.011	0.012	0.009
6	-0.007	-0.004	-0.005	0.023	0.018	0.026	0.021	0.021	0.017
7	-0.002	-0.007	-0.006	0.015	0.013	0.018	0.021	0.013	0.016
8	-0.005	-0.009	-0.008	0.010	0.008	0.016	0.014	0.016	0.018

Following the identification of each card, the image quality of each indirect image was improved using MATLAB's blind deconvolution algorithm. Figure 55 shows the image quality improvement per iteration for the two, five and eight, while Table 8 lists the image quality improvement for each card following 100 iterations of the deconvolution algorithm and Figure 56 shows the improved indirect images.
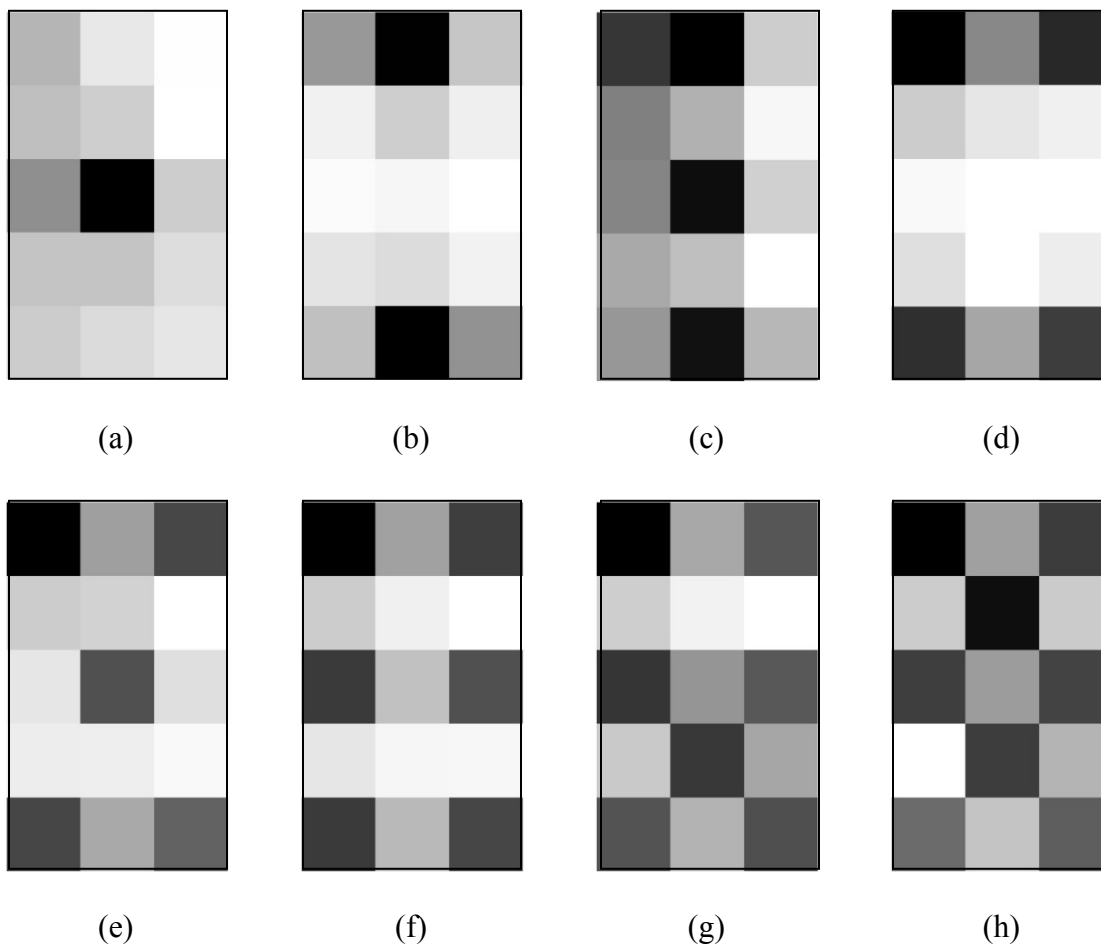
Figure 54. 5x3 indirect images of (a) ace, (b) two, (c) three, (d) four, (e) five, (f) six, (g) seven and (h) eight of clubs
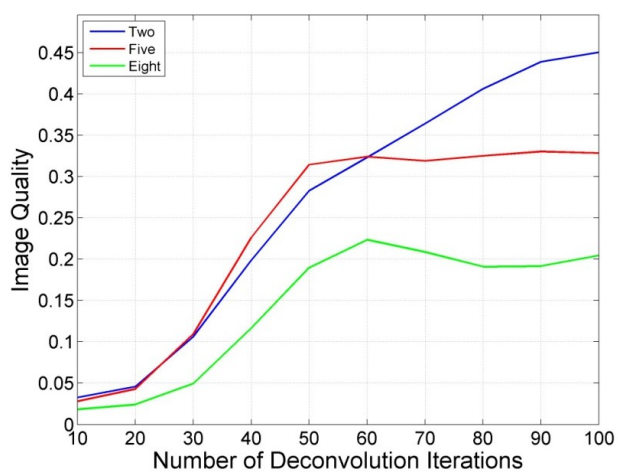
Figure 55. Image quality improvement per deconvolution iteration

Table 8. Indirect image improved image quality

Card	Card							
	Ace	2	3	4	5	6	7L	8
Raw	0.032	0.032	0.026	0.032	0.027	0.026	0.021	0.018
Improved	0.902	0.451	0.317	0.355	0.329	0.2641	0.231	0.2045

(a) (b) (c) (d)

(e) (f) (g) (h)
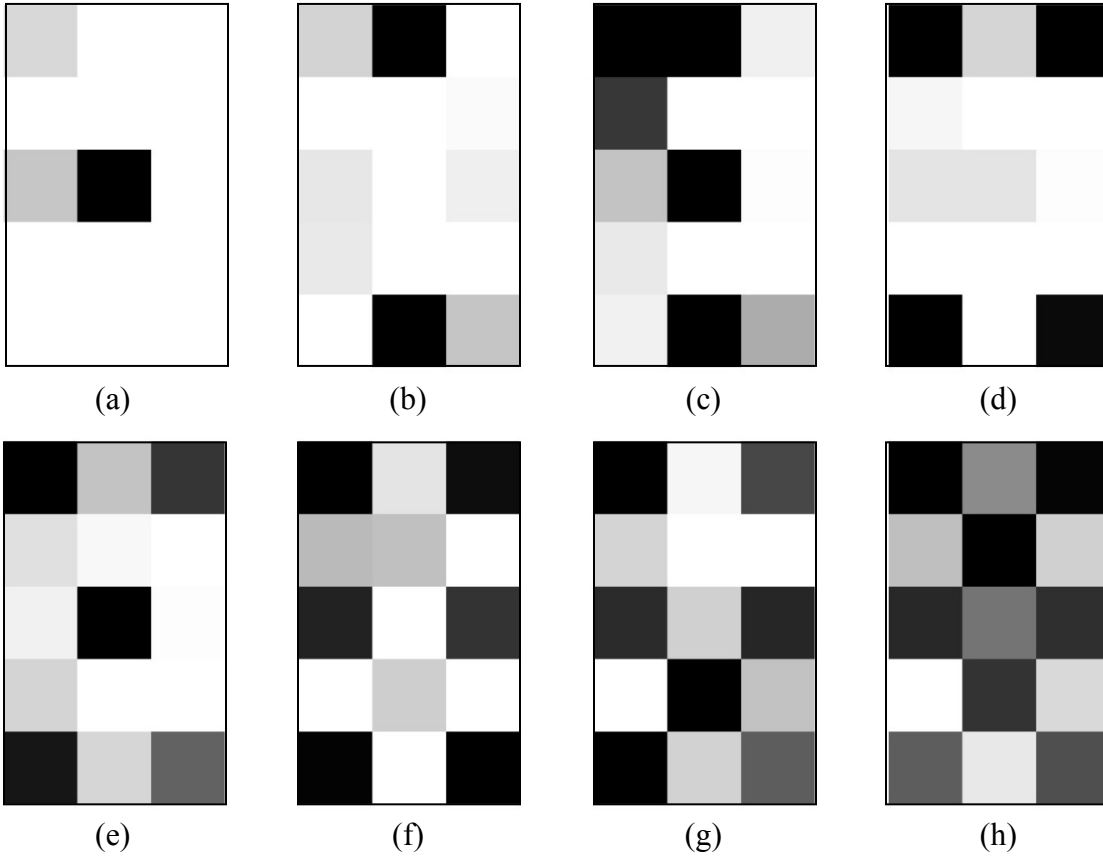
Figure 56. 5x3 improved indirect images for the (a) ace, (b) two, (c) three, (d) four, (e) five, (f) six, (g) seven and (h) eight of clubs

Conclusion

The goal of the simulation and experiments was to confirm the radiometric theory of dual and indirect photography following the setups shown in Figures 11 and 17. In particular, that Eqs. (70), (83) and (96) could be used to improve the quality of the images as defined by Eq. (36).

The 1-D experiment showed indirect photography could be used to recover information about the spatial-frequency content of an object using wall and imaged reflectors with different BRDFs. The 2-D experiment expanded the 1-D experiment and produced images of non-sinusoidal objects. The real-world experiment confirmed indirect photography could be used to produce images in an operational setup by imaging the ace through eight of clubs and computationally identifying each card correctly.

The experiments also showed the image quality of the dual or indirect images could be improved though a deconvolution process. In the case of the dual experiment, the small angle-approximation equation, and the cross section of the laser as the PSF or a blind deconvolution could be used to increase the image quality. In the case of indirect photography a blind deconvolution could be used to increase the image quality.

While standard deconvolution techniques did increase the image quality, the symmetry of the dual/indirect photography process may allow for further improvement of the image quality. The next chapter lays the foundation for that further improvement.

IV. Matrix Formulation

While standard deconvolution techniques can be used to improve the image quality of the indirect images, the formation of the indirect images creates symmetries which may offer the opportunity to improve the deconvolution process. By modeling the indirect image equation using matrices, some of these symmetries have been revealed and research is continuing in the effort to improve the image quality.

Matrix theory of indirect photography

To create the matrix representation of indirect photography, each component of the indirect photography equation, Eq. (78), is represented by a matrix resulting in the following equation:

$$\mathbb{D} = (\mathbb{B} \odot \mathbb{F}_{im}) \cdot (\mathbb{A} \odot \mathbb{F}_{ph}) \cdot \mathbb{P} \odot ((\mathbb{G} \odot \mathbb{F}_w) \cdot \mathbb{E}_w) \tag{98}$$

where

> $\mathbb{D}$ is a $y \times n$ matrix representing the data, y is the number of pixels in the camera and n is the number of data images.
>
> $\mathbb{E}_w$ is a $w \times n$ matrix representing the irradiance on the wall reflector and w is the number of individual points on the wall.
>
> $\mathbb{F}_w$ is a $x \times w$ matrix representing the BRDF of the wall from every point on the wall to every point in the fixed object frame of reference and x is the total number of points in the fixed object frame of reference.
>
> $\mathbb{G}$ is a $x \times w$ matrix representing the geometry terms(γ) from every point on the wall to every point in the fixed object frame of reference.
>
> $\mathbb{P}$, the object reflectance matrix, is a $x \times n$ matrix representing the position of the object of interest in the fixed object frame of reference for every data image.
>
> $\mathbb{F}_{ph}$ is a $y \times x$ matrix representing the BRDF from the fixed object frame of reference to the imaged reflector and y is the number pixels in the camera.[3]
>
> $\mathbb{A}$ is a $y \times x$ matrix representing the geometry terms(α) from every point in the

---

[3] The points on the imaged reflector correspond to the projection of the camera's pixels onto the imaged reflector.

fixed object frame of reference to every point on the imaged reflector.

$\mathbb{F}_{im}$ is a $y \times y$ matrix representing the BRDF from the imaged reflector to the lens of the imaging system which is subsequently focused on the camera's individual pixels.[4]

$\mathbb{B}$ is a $y \times y$ matrix representing the geometry terms(β) from every point in the fixed object frame of reference to the pixels in the camera.

$\cdot$ represents standard matrix multiplication.

$\odot$ represents the Hadamard product.

With the goal of recovering the image represented by any column of the object reflectance matrix, $\mathbb{P}$, the matrices before and after the reflectance matrix can be evaluated to form the equation:

$$\mathbb{D}_{y \times n} = \mathbb{Q}_{y \times x} \cdot \mathbb{P}_{x \times n} \odot \mathbb{R}_{x \times n} \tag{99}$$

where:

$$\mathbb{Q}_{y \times x} = (\mathbb{B} \odot \mathbb{F}_{im})_{y \times y} \cdot \left(\mathbb{A} \odot \mathbb{F}_{ph}\right)_{y \times x} \tag{100}$$

$$\mathbb{R}_{x \times n} = (\mathbb{G} \odot \mathbb{F}_{wall})_{x \times w} \cdot \mathbb{E}_{wall_{w \times n}} \tag{101}$$

To identify the symmetry created by the indirect image process, the structure of each matrix of Eq. (99) will be evaluated. Based on the unknown BRDFs of both the imaged reflector, $\mathbb{F}_{im}$, and the phase function of the object, $\mathbb{F}_{ph}$, as well as the unknown geometry of the setup between the object, the imaged reflector and the lens of the imaging system, nothing can be definitely stated about the structure of the $\mathbb{Q}$ matrix without *a priori* knowledge. Therefore, the $\mathbb{Q}$ matrix, in its most general form, is represented by a $y \times x$ matrix of unknown elements.

---

[4] With an ideal imaging system, $\mathbb{F}_{im}$ would be a diagonal matrix, *i.e.* each pixel is perfectly focused.

$$\mathbb{Q}_{y \times x} = \begin{bmatrix} q_{11} & \cdots & q_{1x} \\ \cdots & \ddots & \vdots \\ q_{y1} & \cdots & q_{yx} \end{bmatrix} \qquad (102)$$

Since both the dual and indirect photography algorithms require the same set of pixels from each data image to be used to create the image, and in keeping with the experiments detailed in Chapter IV, where the entire image is used to form the dual/indirect image, the $\mathbb{Q}$ matrix can be represented by a row vector:

$$\mathbb{Q}_{z \times x} = [q_1, \quad q_2, \quad \cdots \quad , q_n] \qquad (103)$$

The structure of the object reflectance matrix, $\mathbb{P}$, and the irradiance matrix, $\mathbb{R}$, is determined by the number of data images taken, n, the distance the object of interest is translated between each data image in comparison to the size of the object of interest, and the pattern in which the object is translated. To demonstrate this concept, an object with four distinctive points in a two-by-two square pattern will be used. The first data image is acquired for an indirect image as described in the real-world section of Chapter IV. The object is then translated vertically downward a distance equal to one half the vertical length of the object and a second data image is acquired. For the second data image, the irradiance on the upper left quadrant of the object will be the same as the irradiance on the lower left quadrant of the object in the first image. Likewise, the irradiance on the upper right quadrant of the object in the second data image is the same as the irradiance on the lower right quadrant in the first data image. Figure 57 illustrates this symmetry where Figure 57 (a) is the position of the object when the first data image is acquired in comparison to the irradiance in the fixed object frame of reference. Figure 57 (b) shows the position of the object after the translation vertically downward. In both cases, the

blue (upper left) designators represent the irradiance in the fixed object frame of reference and the red (lower right) designators represent the reflectance of that quadrant of the object.

(a)				(b)				(c)				(d)		
r1	r4	r7		r1	r4	r7		r1	r4	r7		r1	r4	r7
p1 *p3*								*p1* *p3*						
r2	r5	r8		r2	r5	r8		r2	r5	r8		r2	r5	r8
p2 *p4*				*p1* *p3*				*p2* *p4*				*p1* *p3*		
r3	r6	r9		r3	r6	r9		r3	r6	r9		r3	r6	r9
				p2 *p4*								*p2* *p4*		
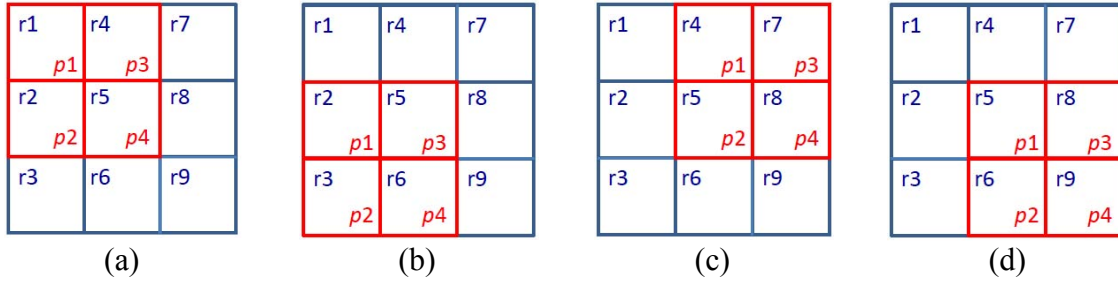
Figure 57. Irradiance of the object given a 2x2 pattern for the (a) first, (b) second, (c) third and (d) fourth data images.

Following the second data image, the object is translated vertically up, to the original vertical position and then horizontally to the right, a distance equal to one half the horizontal width of the object resulting in the configuration shown in Figure 57(c). In this position, the irradiance on the upper and lower left quadrants of the object are the same as the irradiance on the upper and lower right quadrants of the object in the first data image. Figure 57(d) shows the position of the object in the fixed object frame of reference after it has been translated vertically downward from the position of the object in the third data image. The relationship between the irradiance in the fixed object frame of reference and the reflectance of the object between the third and fourth data images is the same as the relationship previously described between the first and second data images.

Given the fixed geometry between the wall reflector and the fixed object frame of reference, the irradiance in the fixed object frame of reference is unchanged from one

data image to the next. Given the scenario described in Figure 57, the irradiance matrix, $\mathbb{R}$, can be represented by:

$$\mathbb{R}_{x \times n} = \begin{bmatrix} r_1 & r_1 & r_1 & r_1 \\ r_2 & r_2 & r_2 & r_2 \\ r_3 & r_3 & r_3 & r_3 \\ r_4 & r_4 & r_4 & r_4 \\ r_5 & r_5 & r_5 & r_5 \\ r_6 & r_6 & r_6 & r_6 \\ r_7 & r_7 & r_7 & r_7 \\ r_8 & r_8 & r_8 & r_8 \\ r_9 & r_9 & r_9 & r_9 \end{bmatrix} \tag{104}$$

where the individual elements, r_1, r_2, *etc,.* represent the irradiance incident on the specific area in the fixed object frame of reference. In a more general form, the irradiance matrix, $\mathbb{R}$, can be written as the Kronecker product of two vectors $\mathbf{R}$ and $\mathbf{e_n^T}$, where $\mathbf{R}$ is the column vector that results from applying the *Vec* operator on the matrix describing the irradiance in the fixed object frame of reference and the vector $\mathbf{e_n}$ is a column vector of n ones where n is the number of data images. (see Eq. (105))

$$\mathbb{R} = \mathbf{R} \otimes \mathbf{e_n^T} \tag{105}$$

In the case of the scenario described by Figure 57, $\mathbf{R}$ and $\mathbf{e_n}$ are represented by:

$$\mathbf{R} = \begin{bmatrix} r_1 \\ r_2 \\ r_3 \\ r_4 \\ r_5 \\ r_6 \\ r_7 \\ r_8 \\ r_9 \end{bmatrix} \quad \text{and} \quad \mathbf{e_n} = \begin{bmatrix} 1 \\ 1 \\ 1 \\ 1 \\ 1 \end{bmatrix} \tag{106}$$

The object reflectance matrix, $\mathbb{P}$, is an $x \times n$ matrix where, for each column of the matrix, the *Vec* operator has been applied to the matrix describing the object in the fixed

object frame of reference corresponding to the data image. The $\mathbb{P}$ matrix for the scenario described in Figure 57 is:

$$\mathbb{P}_{x \times n} = \begin{bmatrix} \rho_1 & 0 & 0 & 0 \\ \rho_2 & \rho_1 & 0 & 0 \\ 0 & \rho_2 & 0 & 0 \\ \rho_3 & 0 & \rho_1 & 0 \\ \rho_4 & \rho_3 & \rho_2 & \rho_1 \\ 0 & \rho_4 & 0 & \rho_2 \\ 0 & 0 & \rho_3 & 0 \\ 0 & 0 & \rho_4 & \rho_3 \\ 0 & 0 & 0 & \rho_4 \end{bmatrix} \tag{107}$$

where the rows of the matrix correspond to the distinctive points in the fixed object frame of reference and the columns correspond to the different data images. Substituting Eqs. (103), (104) and (107) into Eq. (99), the equation for the data matrix becomes:

$$\mathbb{D}_{1 \times n} = \begin{bmatrix} q_1 & \cdots & q_9 \end{bmatrix} \cdot \left(\begin{bmatrix} \rho_1 & 0 & 0 & 0 \\ \rho_2 & \rho_1 & 0 & 0 \\ 0 & \rho_2 & 0 & 0 \\ \rho_3 & 0 & \rho_1 & 0 \\ \rho_4 & \rho_3 & \rho_2 & \rho_1 \\ 0 & \rho_4 & 0 & \rho_2 \\ 0 & 0 & \rho_3 & 0 \\ 0 & 0 & \rho_4 & \rho_3 \\ 0 & 0 & 0 & \rho_4 \end{bmatrix} \odot \begin{bmatrix} r_1 & r_1 & r_1 & r_1 \\ r_2 & r_2 & r_2 & r_2 \\ r_3 & r_3 & r_3 & r_3 \\ r_4 & r_4 & r_4 & r_4 \\ r_5 & r_5 & r_5 & r_5 \\ r_6 & r_6 & r_6 & r_6 \\ r_7 & r_7 & r_7 & r_7 \\ r_8 & r_8 & r_8 & r_8 \\ r_9 & r_9 & r_9 & r_9 \end{bmatrix} \right) \tag{108}$$

As previously stated, the transport of light through the system described above and used to create dual/indirect images is linear. Given that the $\mathbb{R}$ and $\mathbb{Q}$ matrices are defined by the geometry of the setup and the irradiance of the laser spot, both constant throughout the creation of the indirect image, by creating two basis sets, $\mathfrak{B}_{\mathbb{P}}$ and $\mathfrak{B}_{\mathbb{D}}$ to describe the reflectance matrix, $\mathbb{P}$, and the data matrix, $\mathbb{D}$, respectively, and defined as:

$$\mathfrak{B}_{\mathbb{P}} = \{\Psi_1, \Psi_2, \Psi_3, \Psi_4\} \tag{109}$$

$$\mathfrak{B}_{\mathbb{D}} = \{Y_1, Y_2, Y_3, Y_4\} \tag{110}$$

87

where

$$\Psi_1 = \begin{bmatrix} 1 & 0 & 0 & 0 \\ 0 & 1 & 0 & 0 \\ 0 & 0 & 0 & 0 \\ 0 & 0 & 1 & 0 \\ 0 & 0 & 0 & 1 \\ 0 & 0 & 0 & 0 \\ 0 & 0 & 0 & 0 \\ 0 & 0 & 0 & 0 \\ 0 & 0 & 0 & 0 \end{bmatrix}, \Psi_2 = \begin{bmatrix} 0 & 0 & 0 & 0 \\ 1 & 0 & 0 & 0 \\ 0 & 1 & 0 & 0 \\ 0 & 0 & 0 & 0 \\ 0 & 0 & 1 & 0 \\ 0 & 0 & 0 & 1 \\ 0 & 0 & 0 & 0 \\ 0 & 0 & 0 & 0 \\ 0 & 0 & 0 & 0 \end{bmatrix}, \cdots, \Psi_4 = \begin{bmatrix} 0 & 0 & 0 & 0 \\ 0 & 0 & 0 & 0 \\ 0 & 0 & 0 & 0 \\ 0 & 0 & 0 & 0 \\ 1 & 0 & 0 & 0 \\ 0 & 1 & 0 & 0 \\ 0 & 0 & 0 & 0 \\ 0 & 0 & 1 & 0 \\ 0 & 0 & 0 & 1 \end{bmatrix} \tag{111}$$

and

$$\Upsilon_1 = \begin{bmatrix} 1 \\ 0 \\ 0 \\ 0 \end{bmatrix}, \Upsilon_2 = \begin{bmatrix} 0 \\ 1 \\ 0 \\ 0 \end{bmatrix}, \cdots, \Upsilon_4 = \begin{bmatrix} 0 \\ 0 \\ 0 \\ 1 \end{bmatrix} \tag{112}$$

then Eq. (108) can be modeled as a linear transform from the object reflectance basis to the data basis formally defined as:

$$\mathfrak{L}(\mathbb{P}, \mathbb{D}) = \{\mathfrak{T} \colon \mathbb{P} \to \mathbb{D}\} \tag{113}$$

where the linear transform, $\mathfrak{T}$, is formed by applying the Vec operator to the data matrix, $\mathbb{D}$, created when the respective object reflectance basis sets are evaluated. For the scenario described in Figure 57

$$\mathfrak{T} = \left[\mathbb{D}[\Psi_1], \mathbb{D}[\Psi_2], \mathbb{D}[\Psi_3], \mathbb{D}[\Psi_4]\right] \tag{114}$$

Evaluating Eq. (114), the linear transform becomes:

$$\mathfrak{T} = \begin{bmatrix} q_1 r_1 & q_2 r_2 & q_4 r_4 & q_5 r_5 \\ q_2 r_2 & q_3 r_3 & q_5 r_5 & q_6 r_6 \\ q_4 r_4 & q_5 r_5 & q_7 r_7 & q_8 r_8 \\ q_5 r_5 & q_6 r_6 & q_8 r_8 & q_9 r_9 \end{bmatrix} \tag{115}$$

which is a block-Hankel, Hankel-block matrix and can be simplified to:

$$\mathfrak{T} = \begin{bmatrix} a & b & c & d \\ b & e & d & f \\ c & d & g & h \\ d & f & h & i \end{bmatrix} \tag{116}$$

where

$$a = q_1 r_1, b = q_2 r_2, \dots, i = q_9 r_9 \tag{117}$$

Using Eq. (116), an indirect image can be modeled as the linear transform operating on a column vector representing the object to produce the recorded data:

$$\begin{bmatrix} d_1 \\ d_2 \\ d_3 \\ d_4 \end{bmatrix} = \begin{bmatrix} a & b & c & d \\ b & e & d & f \\ c & d & g & h \\ d & f & h & i \end{bmatrix} \cdot \begin{bmatrix} \rho_1 \\ \rho_2 \\ \rho_3 \\ \rho_4 \end{bmatrix} \tag{118}$$

In keeping with the theory of indirect photography described in Chapter III, if the BRDF and geometry of the setup are known *a priori,* then the transform matrix will be known. The transform matrix can then be inverted and when both sides of Eq. (118) are multiplied from the left by the inverted transform matrix, $\mathfrak{T}^{-1}$, the reflectance matrix, $\mathbb{P}$, can be solved for, which, in-turn, allows for the reconstruction of the object of interest.

Given that the BRDFs and geometry of the setup will likely not be available in an operational environment, Eq. (118) must be solved without explicitly knowing the transform matrix, $\mathfrak{T}$. Eq. (118) is underspecified, with four equations and 13 unknowns. Therefore, solving the system of equations directly will not be possible. However, it may be possible to solve Eq. (118) by posing it as an optimization problem and finding the optimum transform matrix and optimum image vector given the constraint that the multiplication of the two matrices results in the data matrix.

To that end, the object has been simplified to a 2x1 matrix, resulting in a 2x2 transform matrix and a 2x1 data matrix. This results in two equations and five unknowns. While research to date has not yielded a solution, progress has been made by optimizing the solution such that total energy of the system is minimized while still satisfying Eq. (118).

Conclusion

At the time of this writing, the matrix formulation has yet to yield the desired results. While more research is required, I believe the best path forward is to divide the data images into equal sections, *i.e.* halves, quadrants, *etc,*. and using each section of the recorded data to form an indirect image. While each of these indirect images will have a unique linear transform, the object remains the same for all of the indirect images. Therefore, solving Eq. (118) simultaneously for all of the indirect images may yield a unique solution at the intersection of the sets of solutions formed by the individual images.

VI. Conclusion

While techniques to image objects through triple layered jungle canopies and camouflage netting have been previously developed, the theory described in Chapter III and the experimental proof of concept described in Chapter IV are the first to allow images to be created either around corners or of objects under solid shelters.

The concept of dual photography, originally designed to aid in the creation of computer generated graphics, was radiometrically modeled and simplified to Eq. (70), repeated here as Eq. (119), which revealed the dual image was a convolution of the object of interest and a kernel comprised of the reflection characteristics of the object and non-specular reflectors as well as the geometry of the set up used to create the dual image.

$$\Phi_{pix_i}(\bar{x}', \theta_{obj}) = \int_{las} \Gamma_i(\bar{x}' - \bar{x}'', \theta_{wall}) \, \rho(\bar{x}'') \, d\bar{x}'' \qquad (119)$$

The dual photography radiometric equation was further simplified by using the small-angle approximation to Eq. (95), repeated here as Eq. (120), which revealed the dual image could be approximated as a convolution of the object of interest and the illumination source.

$$\Phi_{pix_i}(\bar{x}') = K_i \int_{las} E_{obj}(\bar{x}' - \bar{x}'') \rho(\bar{x}'') d\bar{x}'' \qquad (120)$$

These equations showed the image quality of the dual images could be improved through a deconvolution process.   In the case of the small-angle approximation Eq. (120), the irradiance on the object of interest could be used to approximate the point spread function (PSF) of the system and image quality could be improved by standard

deconvolution techniques. In the case of the standard dual photography equation Eq. (119), two processes could be used to improve the image quality. If the exact BRDFs of the reflecting surfaces and geometry of the setup are known, standard deconvolution techniques can be used to improve the image quality. The second process used a blind deconvolution to improve the image quality. This technique has the advantage of not requiring explicit knowledge of the geometry and BRDFs of the reflecting surfaces, a constraint likely to be encountered in an operational situation.

Following the development of the dual photography radiometric equations, the irradiance on the object of interest was changed from the laser spot of dual photography to a reflection from a non-specular surface, resulting in Eq. (83) repeated here:

$$\Phi_{pix_i}(\bar{x}', \theta_{wall}) = \int_{obj} T_i(\bar{x}' - \bar{x}'', \theta_{wall})\, \rho(\bar{x}'')\, d\bar{x}'' \tag{121}$$

As with the dual photography equation, the indirect photography equation implied two important concepts: (1) an indirect image could be created if an individual pixel, any group of pixels or the entire image was used to create the image, as long as the same sets of pixels were used from every data image, and (2) the image quality of the resultant indirect image could be improved through a (blind) deconvolution technique.

Following the development of the theoretical equations, the dual photography equations were experimentally validated using six sinusoidal slides as objects. Figure 28, repeated here as Figure 58 (a), shows the unimproved dual image created using a 1.0 cycles/mm (0.20 cycles/ mrad) slide and image quality improvements made using Lucy-Richardson and blind deconvolution algorithms. Figure 32, repeated here as Figure 58 (b), is the modulation transfer function (MTF) created by the dual/indirect images of all

six slides and shows the improvement in image quality achieved by the deconvolution process.

(a)   (b)
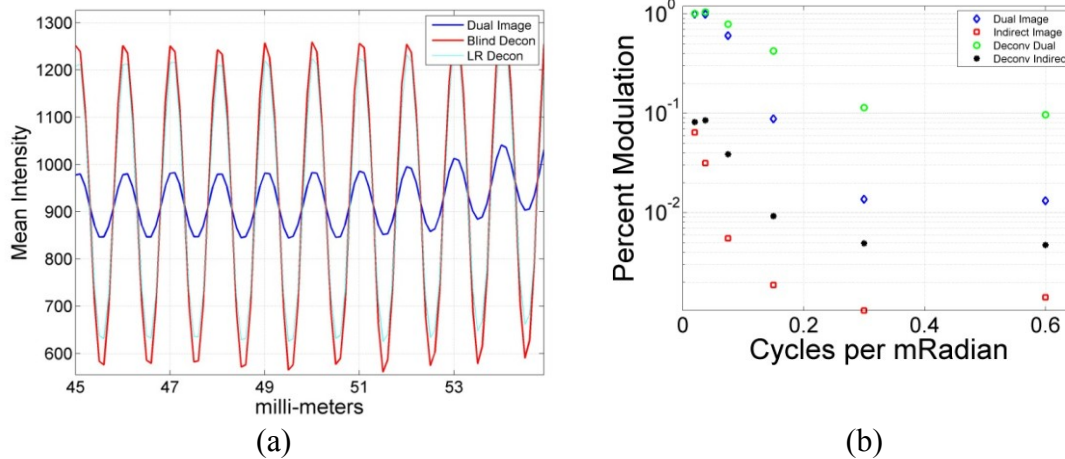
Figure 58. Summary of 1-D experiment (a) Dual 1.0 cycles/mm image and deconvolutions and (b) 1-D semi-gloss reflector MTF

The experiment was expanded to 2-D, resulting in indirect images being created of simple geometric objects. The resultant image quality was evaluated for the raw and improved (deconvolved) images. Representative images showing the raw and deconvolved 2-D indirect images and the resultant MTF originally shown in Figure 43 and 45 have been reprinted here as Figure 59.

Finally, the experiment was reconfigured, co-locating the camera and the laser in an operationally representative configuration. Indirect images of eight playing cards were created and evaluated against the ideal image of all eight playing cards. The image quality analysis resulted in all eight playing cards being properly identified at a resolution of 5x3 pixels. The indirect images of the 5 of clubs at various resolutions are shown in Figure 53 for comparison and the 47x31 resolution is repeated here as Figure 60.

(a)   (b)

(c)
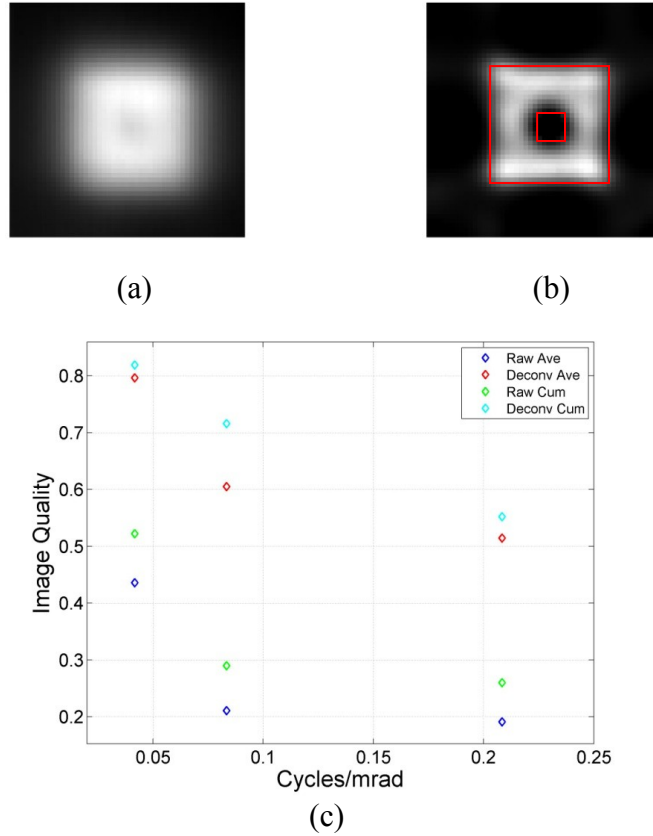
Figure 59. Indirect image of a square annulus (a) unimproved and (b) deconvolved ideal image of the annulus overlaid and(c) MTF created from offset squares.
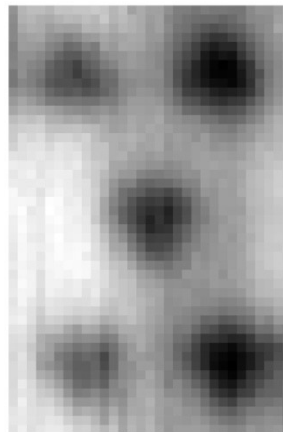
Figure 60. 47x31 indirect image of the 5 of clubs.

The results of this research have been presented at the SPIE conference on Reflections, Scattering and Diffraction from Surfaces II. It has also been submitted to *Optics Express* and is currently under peer review for publication. Additionally, a patent application has been filed with Air Force Material Command for the concept of indirect photography and is under review by intellectual property lawyers.

While the research presented in this document achieved the desired goal of developing the theory of indirect photography and experimentally proving that theory, additional improvements to the theory lend themselves to follow-on research. Some of these possible improvements are: (1) the continuation of the concept described in Chapter V, where the improvement to the deconvolution process is sought by taking advantage of the known symmetries in the matrices that emerge from the radiometric equations involved in the creation of an indirect image. (2) The second area of possible continued research is to polarimetrically model the dual and indirect setups in an effort to take advantage of reflectance differences between polarizations in the creation of the indirect image. (3) Application of advanced signal/image processing beyond the deconvolution process. (4) Research into removing the limitations/assumptions of the theory described in Chapter III, *i.e.* 3-D objects and objects with object with varying phase functions as well as reflectance.

The technique of indirect photography described in this document is still in the early stages of development and requires additional research before an operational prototype can be fielded. That said, I believe this document lays the foundation for that research and has the potential, when fully developed, to aid the military and intelligence

communities in their ability to identify and classify items of interest in situations currently not possible.

Appendix A. Play card BRDFs

To validate the assumption that the BRDF of playing cards can be decomposed into a reflectance, ρ, and a phase function that controls the underlying angular shape of the BRDF as described in Eq. (50), AFIT's CASI was used to measure the BRDF of the white, black and red portions of a standard playing cards. Figure 61 shows the measured BRDFs resulting from 633nm HeNe laser and a 45 degree incident angle. In this graph, 'X' axis is the angular difference from the specular reflection *i.e.* 0 on the 'X' axis represents specular reflection, positive angles are away from the surface normal and negative numbers are toward the surface normal and the incident irradiance. The gap in the data at -90 degrees comes from the sensor blocking the incident irradiance.
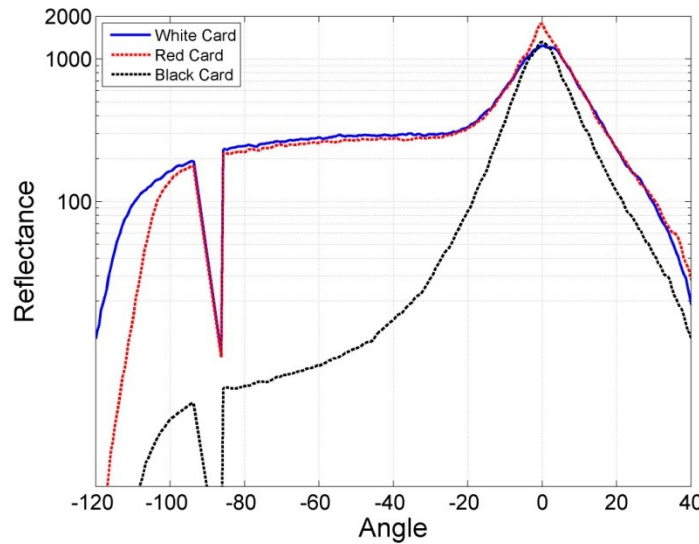
Figure 61. Measured BRDF of standard playing cards.

Appendix B. Indirect Photography Simulation MATLAB Code

The following MATLAB code was used to simulate the dual and indirect photography experiments. A wire-frame model of the fixed object frame of reference (25x25 reflector points) and the wall, for indirect photography, and imaged reflectors (3x3 and 21x21 reflector points respectively) were created. Arrays are then created for all incident and reflected angles and distances from each point on the adjacent reflectors. The glint angle and subsequent BRDF using Eq. (27) on page 18 are also created and stored in arrays. The object was then placed in the upper left corner of the fixed object frame of reference and beginning from the wall reflector, every possible path to the imaging system was evaluated, *i.e.* from each point on the wall reflector to every point on the object reflector to every point on the imaged reflector, *etc.* The total flux impinging on the lens of the imaging system was summed to simulate the entire image was being used to create the dual or indirect image. The object was then translated horizontally and vertically through each of the possible positions and the process repeated. The resultant images are then improved using both *Lucy-Richardson* and *blind* deconvolution algorithms. The raw and improved images are shown in Figure 20 and 22 on pages 48 and 50 respectively.

```
%---------------------------------------------------------------------
%This code is a dual and indirect simulation designed to test the basic
%equations and assumptions made in the mathematical model.
%---------------------------------------------------------------------


%---------------------------------------------------------------------
%Required Input
%---------------------------------------------------------------------

laser = [0,0,-1];

WallNormal = [0,1,-1];
WallCenterPoint = [0,0,0];
xNumWallPoints =3;
yNumWallPoints =3;
xWallLength = .08;
yWallLength = .08;

xNumWallImPoints =21;
yNumWallImPoints =21;
xWallImLength = 3;
yWallImLength = 5;

ObjNormal = [0,-1,0];
ObjCenterPoint = [0,5,0];
xNumObjPoints =25;
zNumObjPoints =25;
xObjLength = 1;
zObjLength = 1;

LensNormal = [0,0,1];
LensCenterPoint = [0,0,-10];
xNumLensPoints =3;
yNumLensPoints =3;
xLensLength = 1;
yLensLength = 1;

SigmaWall = .5* pi/180;
SigmaObj = 1.5 * pi/180;

xSlideWidth = 1;
zSlideWidth = 1;
```

```matlab
%-----------------------------------------------------------------------
% Basic Calculations
WallNormalHat = WallNormal/norm(WallNormal);
ObjNormalHat = ObjNormal/norm(ObjNormal);
LensNormalHat = LensNormal/norm(LensNormal);

TotWallPoints = xNumWallPoints*yNumWallPoints;
TotWallImPoints = xNumWallImPoints*yNumWallImPoints;
TotObjPoints = xNumObjPoints*zNumObjPoints;
TotLensPoints = xNumLensPoints*yNumLensPoints;

xSlideHalfWidth = xSlideWidth/2;
zSlideHalfWidth = zSlideWidth/2;


%-----------------------------------------------------------------------
% This section creates the Reflector Points
%-----------------------------------------------------------------------


%-----------------------------------------------------------------------
% This section creates the Wall Reflector Points
xWallStart = WallCenterPoint(1,1)- (xWallLength/2);
yWallStart = WallCenterPoint(1,2)- (yWallLength/2)*WallNormalHat(1,2);

xWallStep = (xWallLength /(xNumWallPoints-1)) ;
yWallStep = (yWallLength /(yNumWallPoints-1))*WallNormalHat(1,2);

WallArray = zeros(xNumWallPoints,yNumWallPoints,3);

for i = 1:xNumWallPoints
   WallArray(i,:,1)= xWallStart+xWallStep*(i-1);
   for j = 1:yNumWallPoints
     WallArray(:,j,2)= yWallStart+yWallStep*(j-1);
     WallArray(:,j,3)= (WallNormalHat(1,2)*(WallCenterPoint(1,2)-...
     (yWallStart+yWallStep*(j-1))))/WallNormalHat(1,3);
   end
end

FlatWallArray = squeeze(reshape(WallArray,1,TotWallPoints,3));

%-----------------------------------------------------------------------
% This section creates the Imaged Wall Reflector Points
 xWallImStart = WallCenterPoint(1,1)- (xWallImLength/2);
yWallImStart = WallCenterPoint(1,2)- (yWallImLength/2)*WallNormalHat(1,2);

xWallImStep = (xWallImLength /(xNumWallImPoints-1)) ;
yWallImStep = (yWallImLength /(yNumWallImPoints-1))*WallNormalHat(1,2);

WallImArray = zeros(xNumWallImPoints,yNumWallImPoints,3);

for i = 1:xNumWallImPoints
   WallImArray(i,:,1)= xWallImStart+xWallImStep*(i-1);
   for j = 1:yNumWallImPoints
```

```matlab
            WallImArray(:,j,2)= yWallImStart+yWallImStep*(j-1);
            WallImArray(:,j,3)= (WallNormalHat(1,2)*(WallCenterPoint(1,2)-...
            (yWallImStart+yWallImStep*(j-1))))/WallNormalHat(1,3);
    end
end

FlatWallImArray = squeeze(reshape(WallImArray,1,TotWallImPoints,3));


%------------------------------------------------------------------------
% This section creates the Object Reflector Points
 xObjStart = ObjCenterPoint(1,1)- xObjLength/2;
zObjStart = ObjCenterPoint(1,3)- zObjLength/2;

xObjStep = xObjLength /(xNumObjPoints-1);
zObjStep = zObjLength /(zNumObjPoints-1);

ObjArray = zeros(xNumObjPoints,zNumObjPoints,3);

for i = 1:xNumObjPoints
    for j = 1:zNumObjPoints
        ObjArray(i,:,1) = xObjStart + xObjStep*(i-1);
        ObjArray(:,j,3) = zObjStart + zObjStep*(j-1);
    end
end

ObjArray(:,:,2) = ObjCenterPoint(1,2);

FlatObjArray = squeeze(reshape(ObjArray,1,TotObjPoints,3));


%------------------------------------------------------------------------
% This section creates the Lens Points
 xLensStart = LensCenterPoint(1,1)- (xLensLength/2);
yLensStart = LensCenterPoint(1,2)- (yLensLength/2);

xLensStep = (xLensLength /(xNumLensPoints-1));
yLensStep = (yLensLength /(yNumLensPoints-1));

LensArray = zeros(xNumLensPoints,yNumLensPoints,3);

for i = 1:xNumLensPoints
    for j = 1:yNumLensPoints
        LensArray(i,:,1)=xLensStart+xLensStep*(i-1);
        LensArray(:,j,2)=yLensStart+yLensStep*(j-1);
    end
end

LensArray(:,:,3) = LensCenterPoint(1,3);

FlatLensArray = squeeze(reshape(LensArray,1,TotLensPoints,3));
```

```matlab
 clear ('WallCenterPoint','xWallLength','yWallLength',...
   'xWallImLength','yWallImLength',...
   'ObjCenterPoint','xObjLength','zObjLength',...
   'LensCenterPoint','xLensLength','yLensLength')

clear ('xLensStart','xLensStep','yLensStart','yLensStep',...
   'xWallImStart','xWallImStep','xWallStart','xWallStep',...
   'yWallImStart','yWallImStep','yWallStart','yWallStep',...
   'xObjStart','xObjStep','zObjStart','zObjStep')

clear('LensArray','WallArray','WallImArray')

clear('WallNormal','ObjNormal','LensNormal')



%------------------------------------------------------------------------
% This section creates the Distance Arrays for calculations
%------------------------------------------------------------------------


%------------------------------------------------------------------------
% Distance from every point on the Wall to every point on the Object
 DistToObj = zeros(TotWallPoints,TotObjPoints);

for i=1:TotWallPoints
   for j=1:TotObjPoints
      DistToObj(i,j)= norm(FlatWallArray(i,:)-FlatObjArray(j,:));
   end
end

%------------------------------------------------------------------------
% Distance from every point on the Obj to every point on the Imaged Wall

DistToWallIm = zeros(TotObjPoints,TotWallImPoints);

for i=1:TotObjPoints
   for j=1:TotWallImPoints
      DistToWallIm(i,j)= norm(FlatObjArray(i,:)-FlatWallImArray(j,:));
   end
end



%------------------------------------------------------------------------
% Distance from every point on the Imaged Wall to every point on the Lens

DistToLens = zeros(TotWallPoints,TotLensPoints);

for i=1:TotWallImPoints
   for j=1:TotLensPoints
      DistToLens(i,j)= norm(FlatWallImArray(i,:)-FlatLensArray(j,:));
   end
end
```

```matlab
%-------------------------------------------------------------------
% This section creates the Theta Arrays for calculations
%-------------------------------------------------------------------


%-------------------------------------------------------------------
%Cos of the angle between the Wall Normal and every vector between the Wall
%points and the Object Points

CosThetaWallPrime = zeros(TotWallPoints,TotObjPoints);

for i=1:TotWallPoints
   for j=1:TotObjPoints
      RefVect = FlatObjArray(j,:)-FlatWallArray(i,:);
      RefVectHat = RefVect/norm(RefVect);
      CosThetaWallPrime(i,j)= dot(WallNormalHat,RefVectHat);
   end
end


%-------------------------------------------------------------------
%Cos of the angle between the Obj Normal and every vector between the Wall
%points and the Object Points

CosThetaObj = zeros(TotWallPoints,TotObjPoints);

for i=1:TotWallPoints
   for j=1:TotObjPoints
      IncVect = FlatWallArray(i,:)-FlatObjArray(j,:);
      IncVectHat = IncVect/norm(IncVect);
      CosThetaObj(i,j)= dot(ObjNormalHat,IncVectHat);
   end
end


%-------------------------------------------------------------------
%Cos of the angle between the Obj Normal and every vector between the
%Imaged Wall points and the Object Points

CosThetaObjPrime = zeros(TotObjPoints,TotWallImPoints);

for i=1:TotObjPoints
   for j=1:TotWallImPoints
      RefVect = FlatWallImArray(j,:)-FlatObjArray(i,:);
      RefVectHat = RefVect/norm(RefVect);
      CosThetaObjPrime(i,j)= dot(ObjNormalHat,RefVectHat);
   end
end


%-------------------------------------------------------------------
%Cos of the angle between the Imaged Wall Normal and every vector between
%the Object Points and theImaged Wall points

CosThetaWallIm = zeros(TotObjPoints,TotWallImPoints);
```

```matlab
for i=1:TotObjPoints
    for j=1:TotWallImPoints
        IncVect = FlatObjArray(i,:)-FlatWallImArray(j,:);
        IncVectHat = IncVect/norm(IncVect);
        CosThetaWallIm(i,j)= dot(WallNormalHat,IncVectHat);
    end
end


%------------------------------------------------------------------------
%Cos of the angle between the Wall Normal and every vector between the Wall
%points and the Lens Points

CosThetaWallImPrime = zeros(TotWallImPoints,TotLensPoints);

for i=1:TotWallImPoints
    for j=1:TotLensPoints
        RefVect = FlatLensArray(j,:)-FlatWallImArray(i,:);
        RefVectHat = RefVect/norm(RefVect);
        CosThetaWallImPrime(i,j) = dot(WallNormalHat,RefVectHat);
    end
end


%------------------------------------------------------------------------
%Cos of the angle between the Lens Normal and every vector between the Wall
%points and the Lens Points

CosThetaLens = zeros(TotWallImPoints,TotLensPoints);

for i=1:TotWallImPoints
    for j=1:TotLensPoints
        IncVect = FlatWallImArray(i,:)-FlatLensArray(j,:);
        IncVectHat = IncVect/norm(IncVect);
        CosThetaLens(i,j)= dot(LensNormalHat,IncVectHat);
    end
end

clear ('WallArray','WallImArray')



%------------------------------------------------------------------------
% This section creates the Glint Anlge Arrays for calculations
%------------------------------------------------------------------------


%------------------------------------------------------------------------
% This section creates the Wall Glint Angle Array

WallGlintAngle= zeros(TotWallPoints,TotObjPoints);

IncRay = laser;
for i = 1:TotWallPoints
    for j =1:TotObjPoints
        RefRay =FlatObjArray(j,:)-FlatWallArray(i,:);
```

```matlab
            RefRayHat = RefRay/norm(RefRay);
            GlintVec = (RefRayHat + IncRay)/2;
            GlintVecHat = GlintVec/norm(GlintVec);
            WallGlintAngle(i,j)=acos(dot(GlintVecHat,WallNormalHat));
        end
    end


%-----------------------------------------------------------------------
% This section creates the Object Glint Angle Array

ObjGlintAngle = zeros(TotWallPoints,TotObjPoints,TotWallImPoints);

for i = 1:TotWallPoints
    for j=1:TotObjPoints
        IncRay = FlatWallArray(i,:)-FlatObjArray(j,:);
        IncRayHat = IncRay/norm(IncRay);
        for k = 1:TotWallImPoints
            RefRay = FlatWallImArray(k,:)-FlatObjArray(j,:);
            RefRayHat = RefRay/norm(RefRay);
            GlintVec = (RefRayHat + IncRayHat)/2;
            GlintVecHat = GlintVec/norm(GlintVec);
            ObjGlintAngle(i,j,k)= acos(dot(GlintVecHat,ObjNormalHat));
        end
    end
end


%-----------------------------------------------------------------------
% This section creates the Wall Imaged Glint Angle Array

WallImGlintAngle = zeros(TotObjPoints,TotWallImPoints,TotLensPoints);

for i = 1:TotObjPoints
    for j = 1:TotWallImPoints
        IncRay = FlatObjArray(i,:)-FlatWallImArray(j,:);
        IncRayHat = IncRay/norm(IncRay);
        for k = 1:TotLensPoints
            RefRay = FlatLensArray(k,:)-FlatWallImArray(j,:);
            RefRayHat = RefRay/norm(RefRay);
            GlintVec = (RefRayHat + IncRayHat)/2;
            GlintVecHat = GlintVec/norm(GlintVec);
            WallImGlintAngle(i,j,k)= acos(dot(GlintVecHat,WallNormalHat));
        end
    end
end

clear ('FlatLensArray','FlatObjArray','FlatWallArray','FlatWallImArray')

clear ('RefRay','RefRayHat','RefVect','RefVectHat')

clear ('ObjNormalHat','LensNormalHat','WallNormalHat')
```

```matlab
%-----------------------------------------------------------------------
% This section creates the model
%-----------------------------------------------------------------------


%-----------------------------------------------------------------------
% This section models the Wall Radiance

LWall = zeros(TotWallPoints,TotObjPoints);
for i = 1:TotWallPoints
    for j = 1:TotObjPoints
        LWall(i,j) =(1/(2*pi*SigmaWall^2*cos(WallGlintAngle(i,j))^3))*...
            exp(-tan(WallGlintAngle(i,j)^2)/(2* SigmaWall^2));
    end
end


%-----------------------------------------------------------------------
% This section models the Object Irradiance

EObj = zeros(TotWallPoints,TotObjPoints);

for i = 1:TotWallPoints
    for j=1:TotObjPoints
        EObj(i,j)= LWall(i,j)*...
            CosThetaWallPrime(i,j)*CosThetaObj(i,j)/DistToObj(i,j)^2;
    end
end

WGA = reshape(WallGlintAngle(5,:),xNumObjPoints,zNumObjPoints);
LW = reshape(LWall(5,:),xNumObjPoints,zNumObjPoints);
EO = reshape(LWall(5,:),xNumObjPoints,zNumObjPoints);

clear ('WallGlintAngle','CosThetaWallPrime','CosThetaObj',...
    'DistToObj','LWall')

%-----------------------------------------------------------------------
% This section models the Object Radiance

LObj = zeros(TotWallPoints,TotObjPoints,TotWallImPoints);

for i = 1:TotWallPoints
    for j = 1:TotObjPoints
        for k = 1:TotWallImPoints
            LObj(i,j,k)= EObj(i,j)*...
                (1/(2*pi*SigmaObj^2*cos(ObjGlintAngle(i,j,k))^3))*...
                exp(-tan(ObjGlintAngle(i,j,k)^2)/(2* SigmaObj^2));
        end
    end
end
```

106

```matlab
%---------------------------------------------------------------------
% This section models the Imaged Wall Irradiance

EIm = zeros(TotWallPoints,TotObjPoints,TotWallImPoints);

for i = 1:TotWallPoints
    for j = 1:TotObjPoints
        for k = 1:TotWallImPoints
            EIm(i,j,k)= LObj(i,j,k)*...
                CosThetaObjPrime(j,k)*CosThetaWallIm(j,k)/DistToWallIm(j,k)^2;
        end
    end
end

clear('EObj','ObjGlintAngle','LObj','CosThetaObjPrime',...
    'CosThetaWallIm','DistToWallIm')

%---------------------------------------------------------------------
% This section models the Imaged Wall Radiance

LIm =zeros(TotWallPoints,TotObjPoints,TotWallImPoints,TotLensPoints);

for i = 1:TotWallPoints
    for j = 1:TotObjPoints
        for k = 1:TotWallImPoints
            for l = 1:TotLensPoints
                LIm(i,j,k,l)= EIm(i,j,k)*...
                    (1/(2*pi*SigmaWall^2*cos(WallImGlintAngle(j,k,l))^3))*...
                    exp(-tan(WallImGlintAngle(j,k,l)^2)/(2* SigmaWall^2));
            end
        end
    end
end

%---------------------------------------------------------------------
% This section models the Imaged Wall Radiance

ELens= zeros(TotWallPoints,TotObjPoints,TotWallImPoints,...
    TotLensPoints);

for i = 1:TotWallPoints
    for j = 1:TotObjPoints
        for k = 1:TotWallImPoints
            for l = 1:TotLensPoints
                ELens(i,j,k,l)= LIm(i,j,k,l)* ...
                    CosThetaWallImPrime(k,l)*CosThetaLens(k,l)/...
                    DistToLens(k,l)^2;
            end
        end
    end
end
```

```matlab
clear ('WallImGlintAngle','EIm','CosThetaWallImPrime','CosThetaLens',...
    'DistToLens','LIm')

clear ('GlintVec','GlintVecHat','IncRay','IncRayHat','IncVect',...
    'IncVectHat')

%-----------------------------------------------------------------------
% This section creates a 2D dual image of the center point object

DualImage2D = zeros(21,21);

for x = 3:23

    xSlideEdgePlus = x+2;
    xSlideEdgeMinus = x-2;

    for z = 3:23

        zSlideEdgePlus = z+2;
        zSlideEdgeMinus = z-2;

        Slide = zeros(xNumObjPoints,zNumObjPoints);

        Slide(x,z)=1;

        FlatSlide = squeeze(reshape(Slide,1,TotObjPoints));

        for i = 1:TotWallPoints
            illum = 1;
            switch i
                case 2
                    illum = 3;
                case 4
                    illum = 3;
                case 5
                    illum = 5;
                case 6
                    illum = 3;
                case 8
                    illum = 3;
            end
            for j1 = 11:13
                for j2 = 12:14
                    j = 25*j1+j2;
                    for k = 1:TotWallImPoints
                        for l = (TotLensPoints+1)/2:(TotLensPoints+1)/2
                            temp = ELens(i,j,k,l)*FlatSlide(j);
                            DualImage2D(x-2,z-2)=...
                                DualImage2D(x-2,z-2)+temp;
                        end
                    end
                end
```

108

```matlab
        end
      end

  end
end

DPoint = DualImage2D;

%------------------------------------------------------------------------
% This section creates a 2D indirect image of the center point object

IndirectImage2D = zeros(21,21);

for x = 3:23

  xSlideEdgePlus = x+2;
  xSlideEdgeMinus = x-2;

  for z = 3:23

    zSlideEdgePlus = z+2;
    zSlideEdgeMinus = z-2;

    Slide = zeros(xNumObjPoints,zNumObjPoints);

    Slide(x,z)=1;

    FlatSlide = squeeze(reshape(Slide,1,TotObjPoints));

    for i = 1:TotWallPoints
      illum = 1;
      switch i
        case 2
          illum = 3;
        case 4
          illum = 3;
        case 5
          illum = 5;
        case 6
          illum = 3;
        case 8
          illum = 3;
      end
      for j = 1:TotObjPoints
        for k = 1:TotWallImPoints
          for l = (TotLensPoints+1)/2:(TotLensPoints+1)/2
            temp = ELens(i,j,k,l)*FlatSlide(j);
            IndirectImage2D(x-2,z-2)=...
                IndirectImage2D(x-2,z-2)+temp;
          end
        end
```

```matlab
        end

      end

    end
end


IPoint = IndirectImage2D;




%----------------------------------------------------------------------
% This section creates a 2D dual image of the two squares

DualImage2D = zeros(21,21);

for x = 3:23

    xSlideEdgePlus = x+2;
    xSlideEdgeMinus = x-2;

    for z = 3:23

        zSlideEdgePlus = z+2;
        zSlideEdgeMinus = z-2;

        Slide = zeros(xNumObjPoints,zNumObjPoints);

        Slide(x-1,z-1)=1;
        Slide(x+1,z+1)=1;

        FlatSlide = squeeze(reshape(Slide,1,TotObjPoints));

        for i = 1:TotWallPoints
            illum = 1;
            switch i
                case 2
                    illum = 3;
                case 4
                    illum = 3;
                case 5
                    illum = 5;
                case 6
                    illum = 3;
                case 8
                    illum = 3;
            end
            for j1 = 11:13
                for j2 = 12:14
                    j = 25*j1+j2;
```

```matlab
                for k = 1:TotWallImPoints
                    for l = (TotLensPoints+1)/2:(TotLensPoints+1)/2
                        temp = ELens(i,j,k,l)*FlatSlide(j);
                        DualImage2D(x-2,z-2)=...
                            DualImage2D(x-2,z-2)+temp;
                    end
                end
            end

        end
    end

  end
end

D2Point = DualImage2D;

%---------------------------------------------------------------------
% This section creates a 2D indirect image of the two squares

IndirectImage2D = zeros(21,21);

for x = 3:23

  xSlideEdgePlus = x+2;
  xSlideEdgeMinus = x-2;

  for z = 3:23

    zSlideEdgePlus = z+2;
    zSlideEdgeMinus = z-2;

    Slide = zeros(xNumObjPoints,zNumObjPoints);

    Slide(x-1,z-1)=1;
    Slide(x+1,z+1)=1;

    FlatSlide = squeeze(reshape(Slide,1,TotObjPoints));

    for i = 1:TotWallPoints
        illum = 1;
        switch i
            case 2
                illum = 3;
            case 4
                illum = 3;
            case 5
                illum = 5;
            case 6
                illum = 3;
            case 8
                illum = 3;
```

111

```matlab
            end
        for j = 1:TotObjPoints
            for k = 1:TotWallImPoints
                for l = (TotLensPoints+1)/2:(TotLensPoints+1)/2
                    temp = ELens(i,j,k,l)*FlatSlide(j);
                    IndirectImage2D(x-2,z-2)=...
                        IndirectImage2D(x-2,z-2)+temp;
                end
            end
        end

        end

    end
end

I2Point = IndirectImage2D;
```

Appendix C. Reflector BRDF measurements

Figure 62 shows the measured BRDF from the semi-gloss reflector resulting from 633nm HeNe laser and a 45 degree incident angle. In this graph, the 'X' axis is the angle difference from the specular reflection *i.e.* 0 on the 'X' axis represents specular reflect, positive angles are away from the surface normal and negative angles are back toward the surface normal and the incident irradiance. The gap in the data at -90 degrees comes from the sensor blocking the incident irradiance. The data was gathered from three different locations to validate the assumption the reflector was homogenous. In one of the measurements, the sample was rotated 90 degrees, to validate the isotropic assumption.
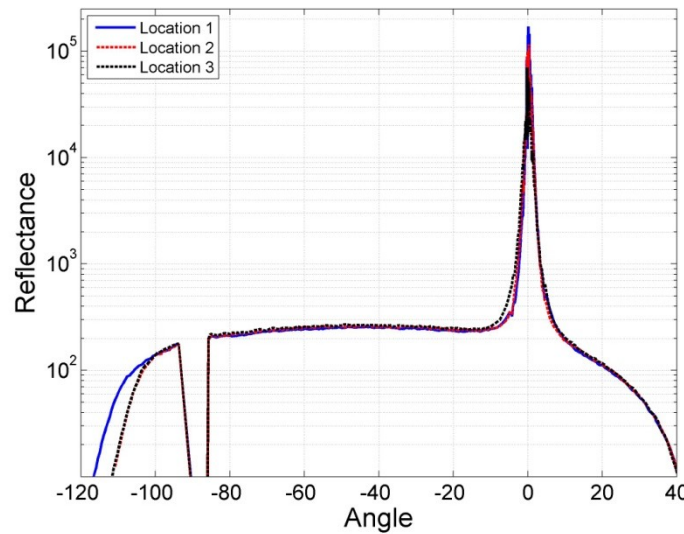
Figure 62. Measured semi-gloss reflector BRDF

Figure 63 shows the measured BRDF from the semi-gloss reflector resulting from 633nm HeNe laser and a 45 degree incident angle.
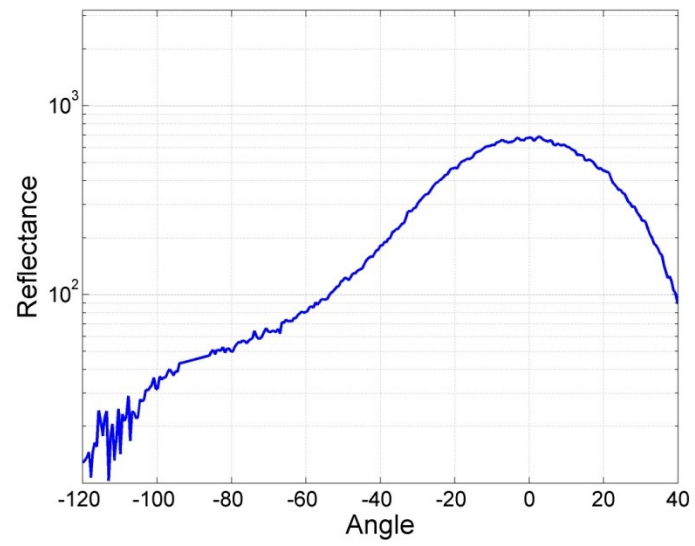
Figure 63. Measured flat white reflector BRDF

Appendix D. Semi-gloss reflector 1-D images

Figure 32, repeated here as Figure 64, shows the MTF created from the 1-D experiment using the semi-gloss imaged reflector. The raw and deconvolved dual and indirect images as well as the Fourier transforms used to create the MTF are shown in Figure 65 through 69.
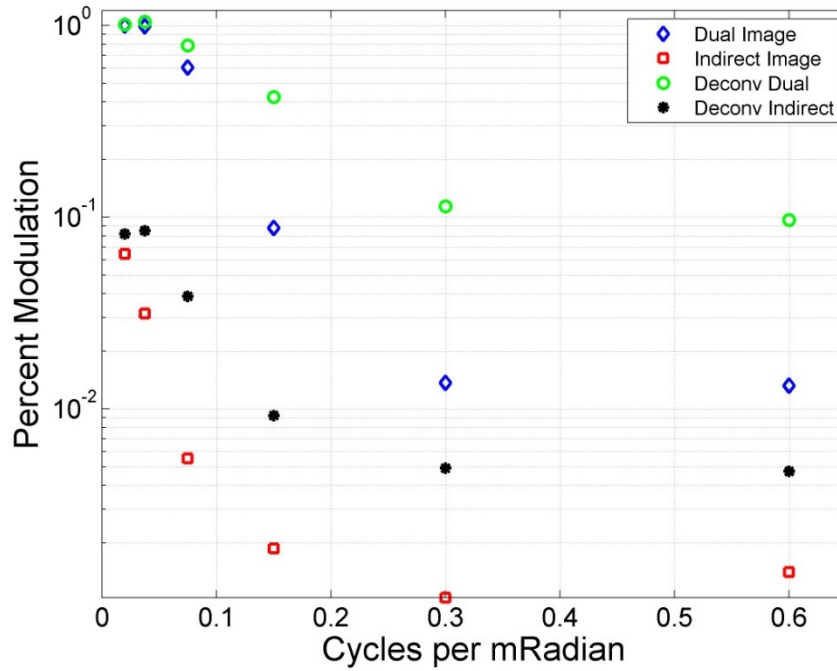
Figure 64. 1-D Semi-gloss MTF

Figure 65 shows the dual images created using the semi-gloss imaged reflector of the following slides: (a) 0.1 cycles/mm, (b) 0.2 cycles/mm, (c) 0.5 cycles./mm, (d) 1.0 cycles/mm, (e) 2.0 cycles/mm and (f) 3.0 cycle/mm. Figure 65 (g), (h) and (i) show an expanded view of (d), (e) and (f) respectively. Figure 66 shows the 1-D indirect images created using the semi-gloss imaged reflector of the following slides: (a) 0.1 cycles/mm, (b) 0.2 cycles/mm, (c) 0.5 cycles/mm, (d) 1.0 cycles/mm, (e) 2.0 cycles/mm and (f) 3.0

cycle/mm. Figure 66 (g), (h) and (i) show an expanded view of (d), (e) and (f) respectively. Figure 67 shows the deconvolved images overlaid on the raw images, (a) through (f) are the dual images while (g) through (l) are the indirect images. The individual images are as follows: (a) and (g) 0.1 cycles/mm, (b) and (h) 0.2 cycles/mm, (c) and (i) 0.5 cycles/mm, (d) and (j) expanded view of 1.0 cycles/mm, (e) and (k) expanded view of 2.0 cycles/mm, (f) and (l) expanded view of the 3.0 cycle/mm. Figure 68 (a) through (l) shows the Fourier transforms of the dual images shown in Figure 67 (a) through (l), while Figure 69(a) through (l) shows the Fourier transforms of the indirect images of Figure 67 (a) through (l).
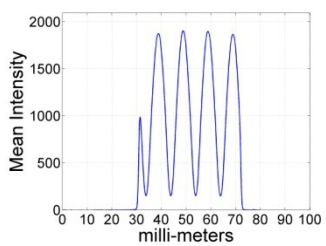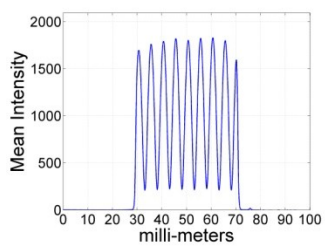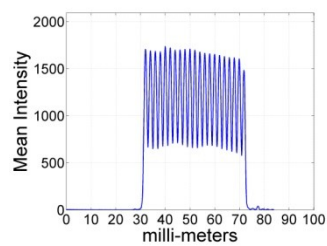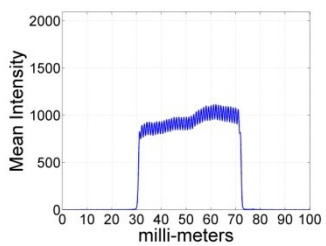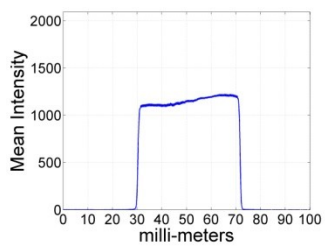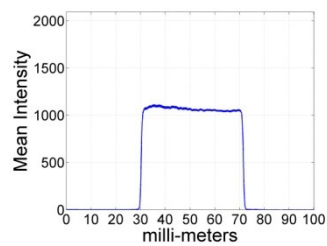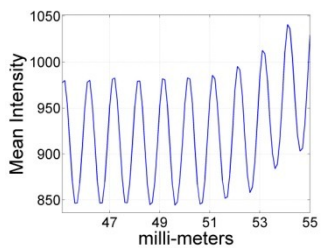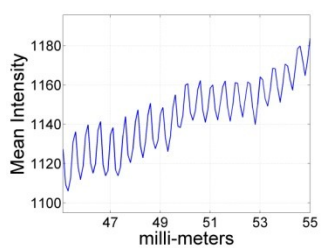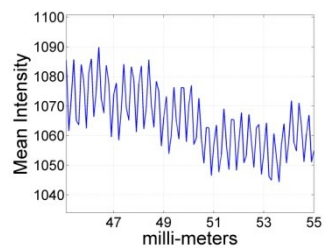
Figure 65. 1-D Semi-gloss dual images
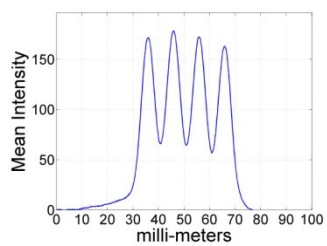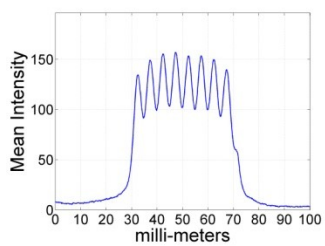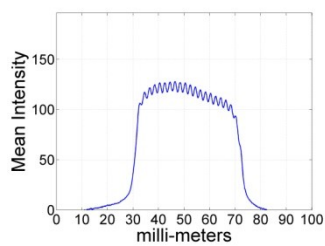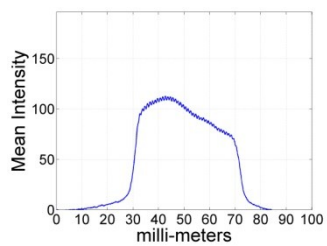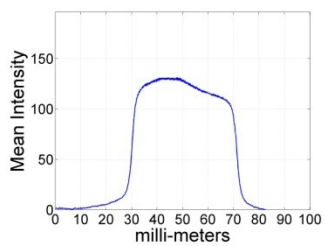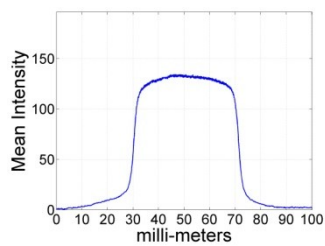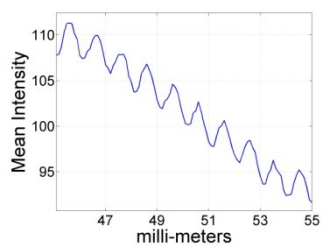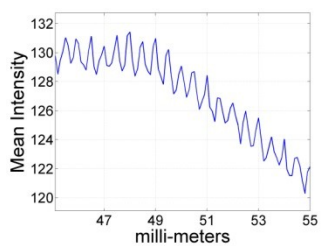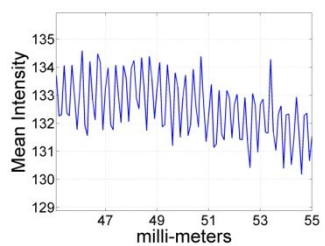
Figure 66. 1-D Semi-gloss indirect images

(a) (b) (c)
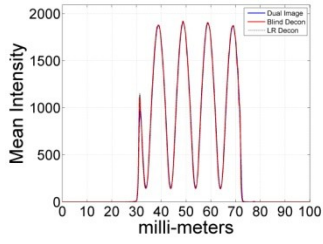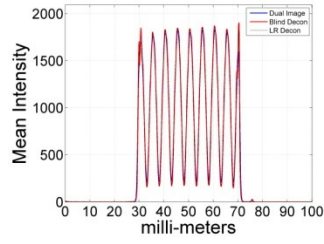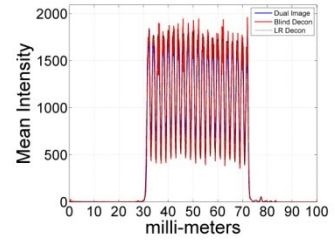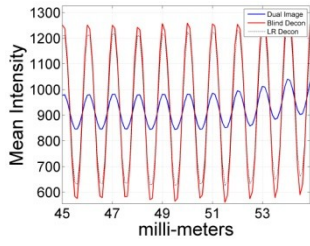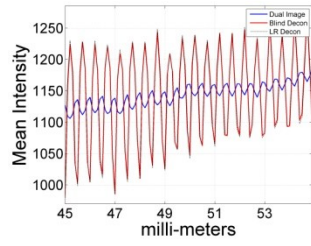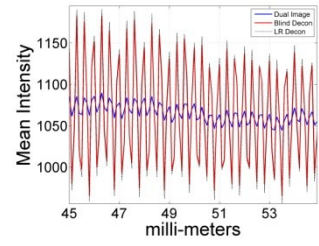
(d) (e) (f)
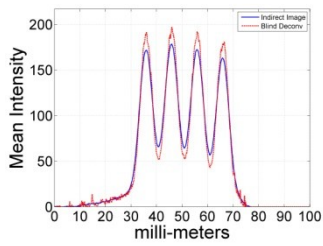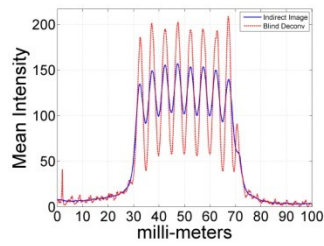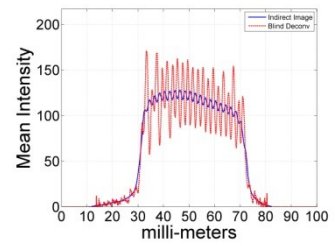
(g) (h) (i)
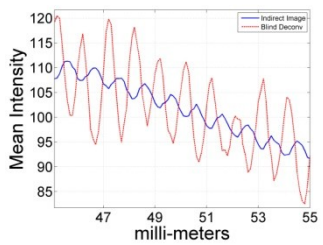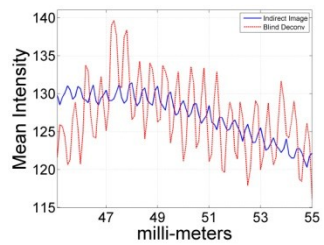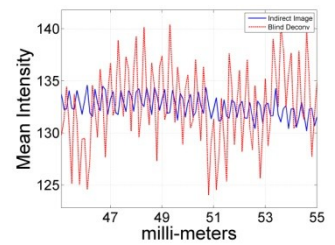
(j) (k) (l)

Figure 67. 1-D Semi-gloss dual and indirect deconvolved images
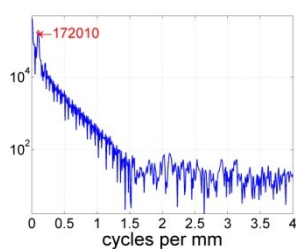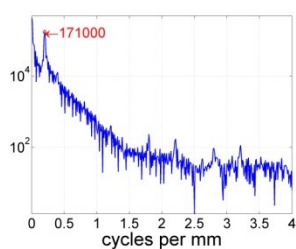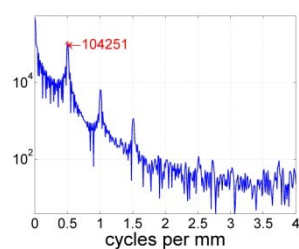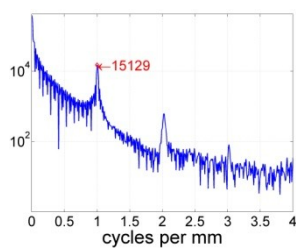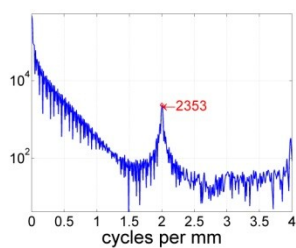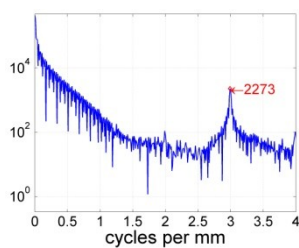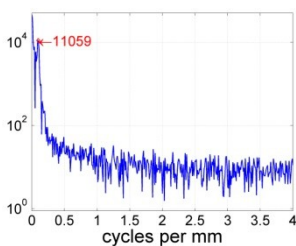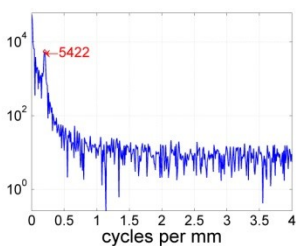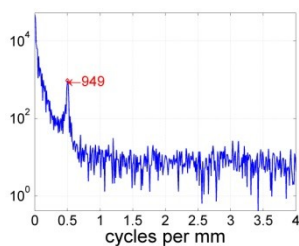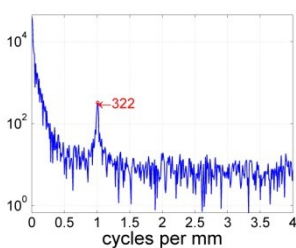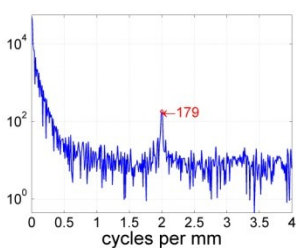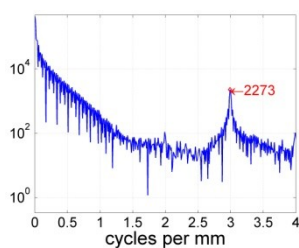
Figure 68. 1-D Semi-gloss dual and indirect image Fourier transforms

120
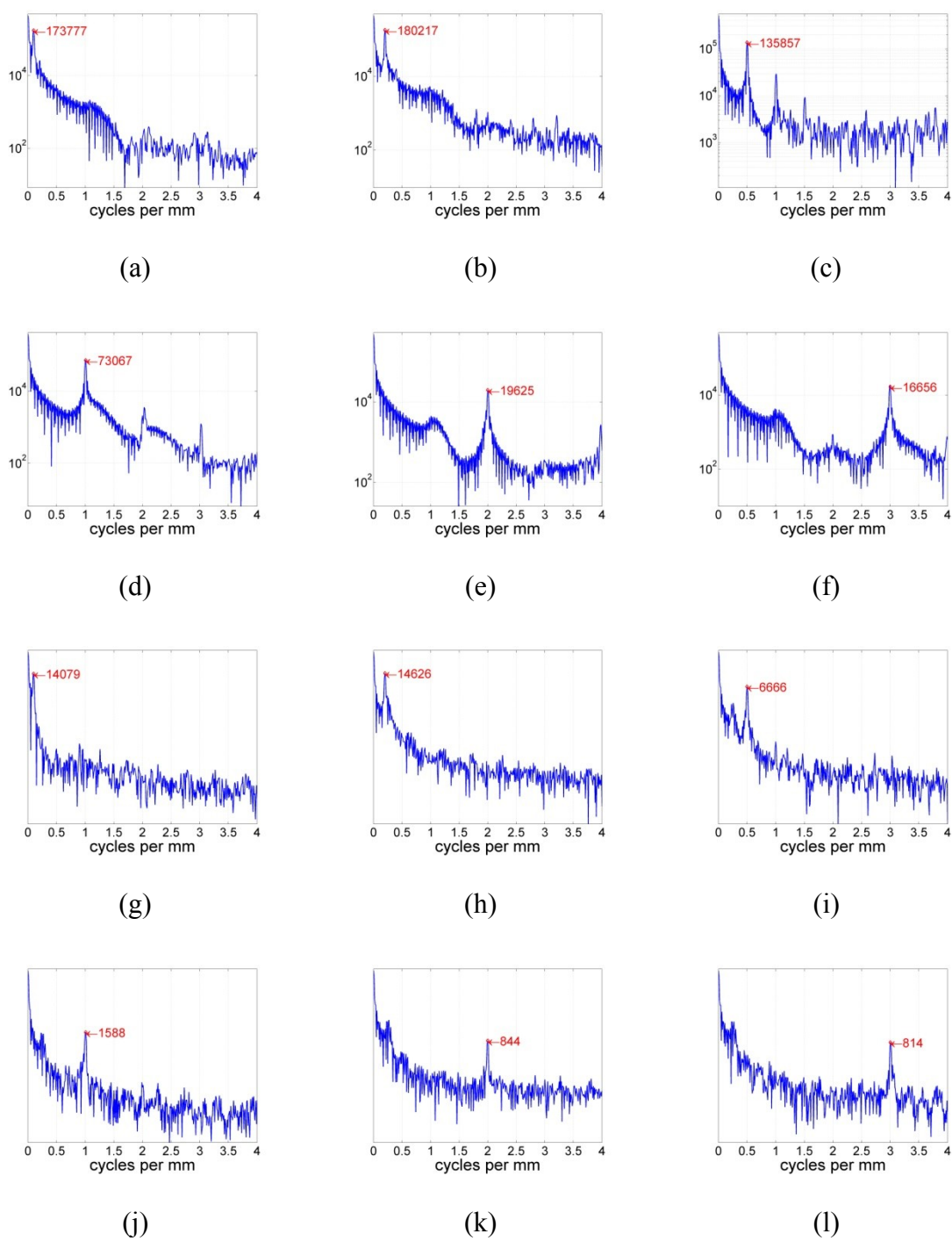
Figure 69. 1-D Semi-gloss deconvolved dual and indirect image Fourier transforms

121

Appendix E. Flat White reflector 1-D images

Figure 33, repeated here as Figure 70, shows the MTF created from the 1-D experiment using the flat white imaged reflector. The raw and deconvolved dual and indirect images as well as the Fourier transforms used to create the MTF are shown in Figure 71 through 75.
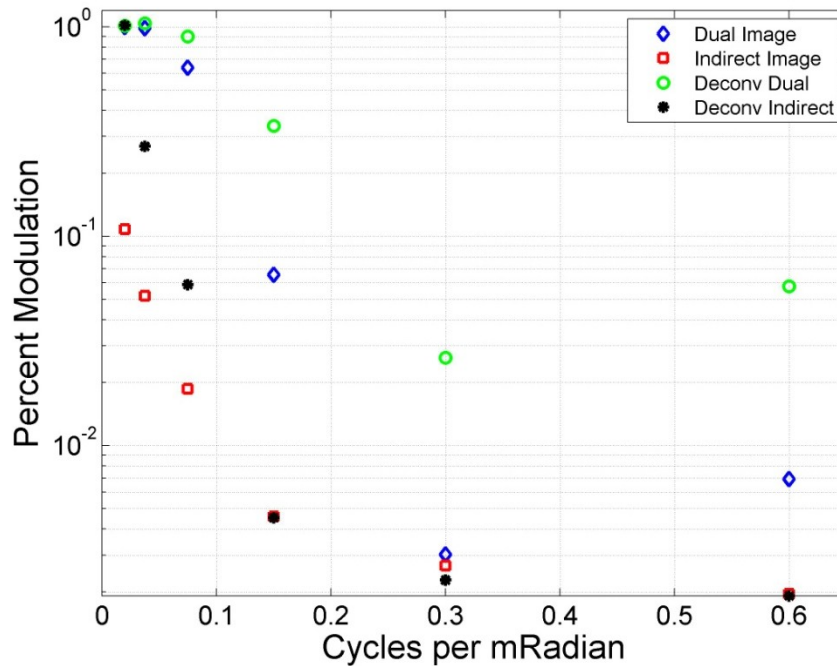
Figure 70. 1-D Flat white MTF

Figure 71 shows the dual images created using the flat white imaged reflector of the following slides: (a) 0.1 cycles/mm, (b) 0.2 cycles/mm, (c) 0.5 cycles./mm, (d) 1.0 cycles/mm, (e) 2.0 cycles/mm and (f) 3.0 cycle/mm. Figure 71 (g), (h) and (i) show an expanded view of (d), (e) and (f) respectively. Figure 72 shows the 1-D indirect images created using the flat white imaged reflector of the following slides: (a) 0.1 cycles/mm, (b) 0.2 cycles/mm, (c) 0.5 cycles/mm, (d) 1.0 cycles/mm, (e) 2.0 cycles/mm and (f) 3.0

cycle/mm. Figure 72 (g), (h) and (i) show an expanded view of (d), (e) and (f) respectively. Figure 73 shows the deconvolved images overlaid on the raw images (a) through (f) are the dual images while (g) through (l) are the indirect images. The individual images are as follows: (a) and (g) 0.1 cycles/mm, (b) and (h) 0.2 cycles/mm, (c) and (i) 0.5 cycles/mm, (d) and (j) expanded view of 1.0 cycles/mm, (e) and (k) expanded view of 2.0 cycles/mm, (f) and (l) expanded view of the 3.0 cycle/mm. Figure 74 (a) through (l) shows the Fourier transforms of the dual images shown in Figure 73 (a) through (l), while Figure 75(a) through (l) shows the Fourier transforms of the indirect images of Figure 73 (a) through (l).
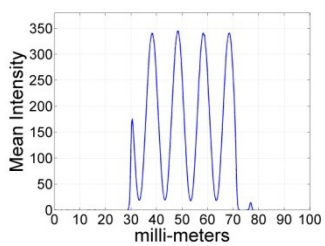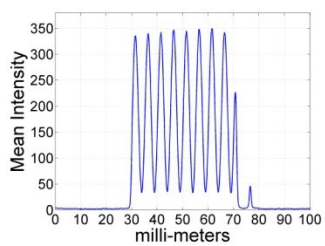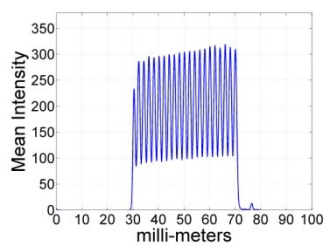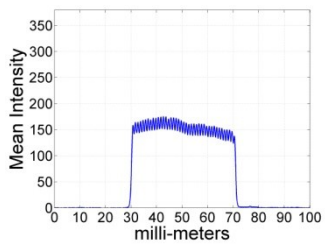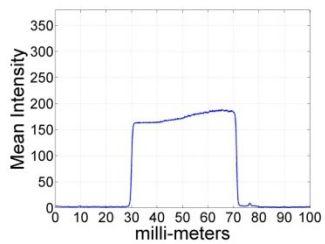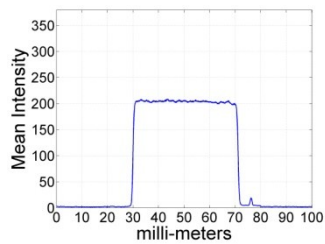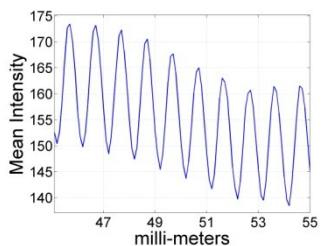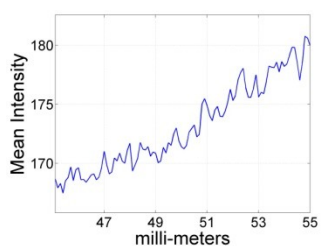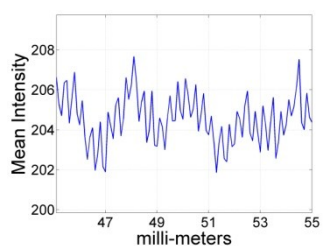
Figure 71. 1-D Flat white dual images
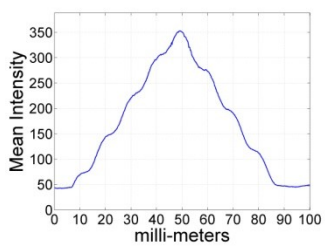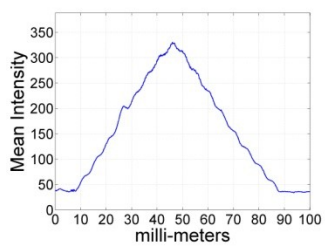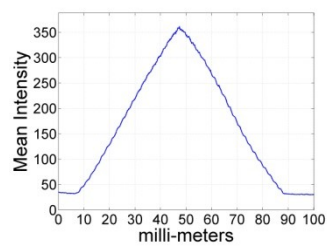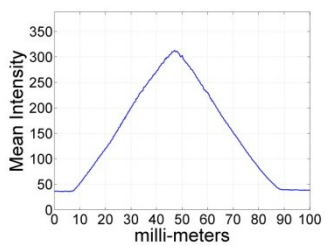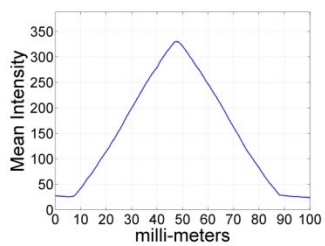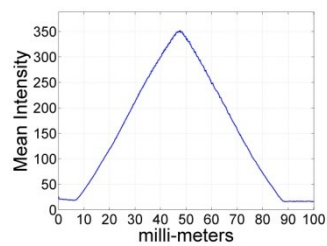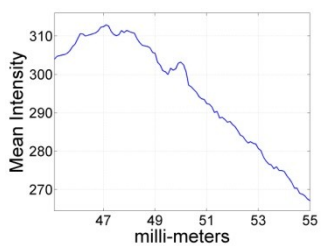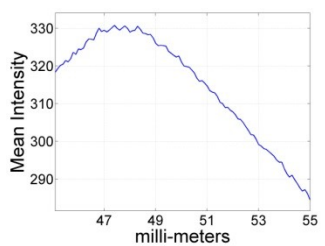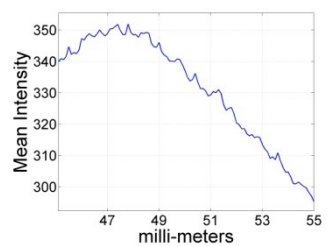
Figure 72. 1-D Flat white indirect images
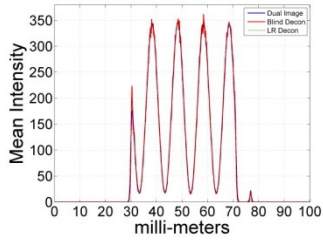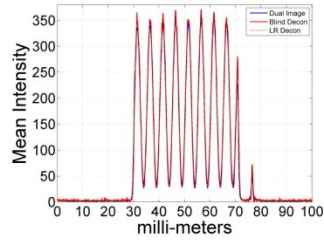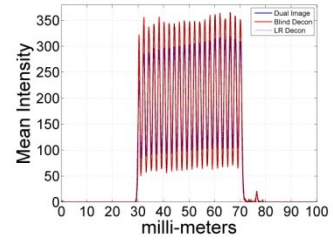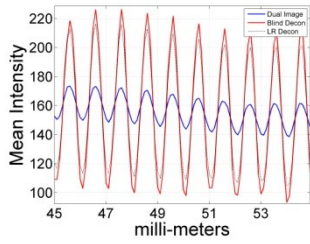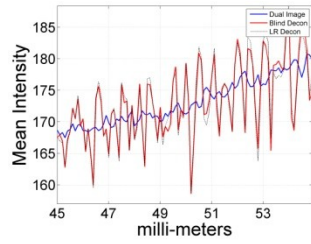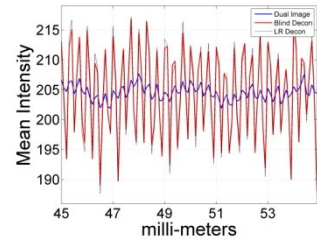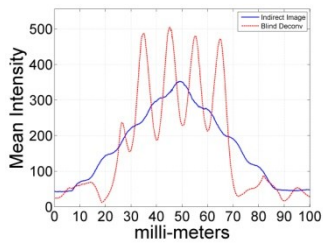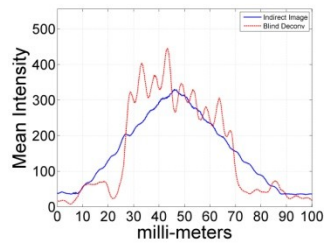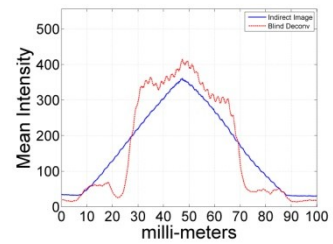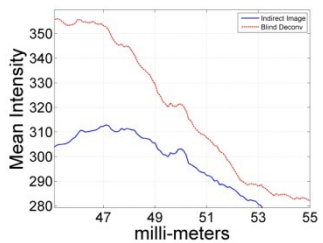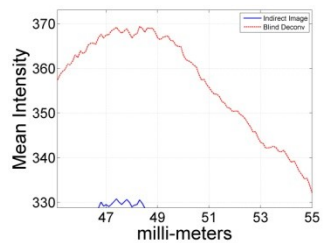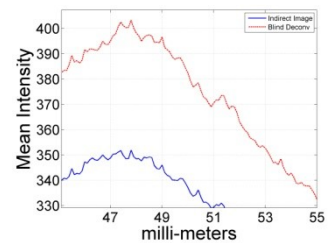
Figure 73. 1-D Flat white dual and indirect deconvolved images

126
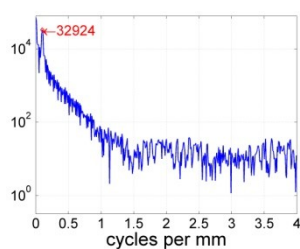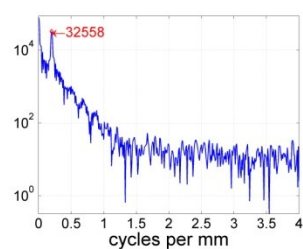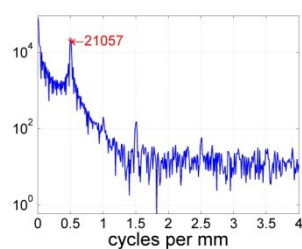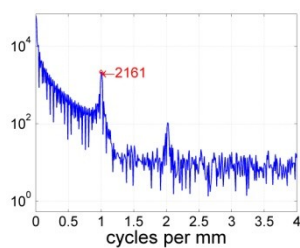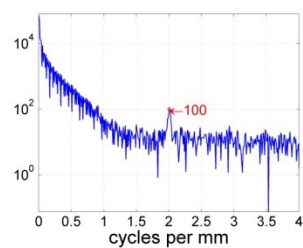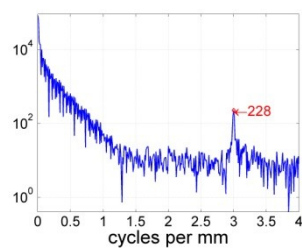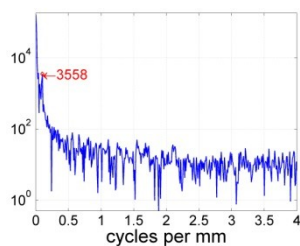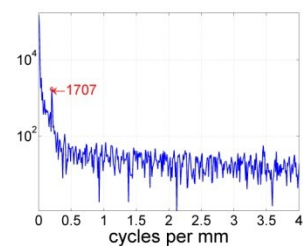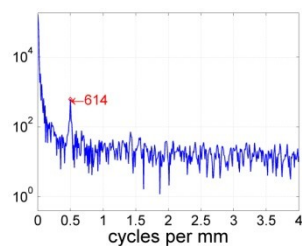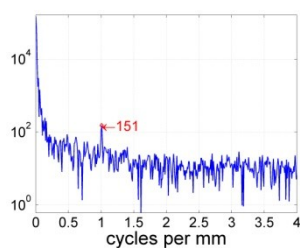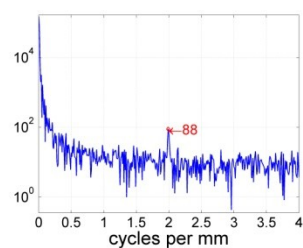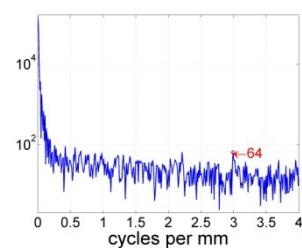
Figure 74. 1-D Flat white dual and indirect image Fourier transforms
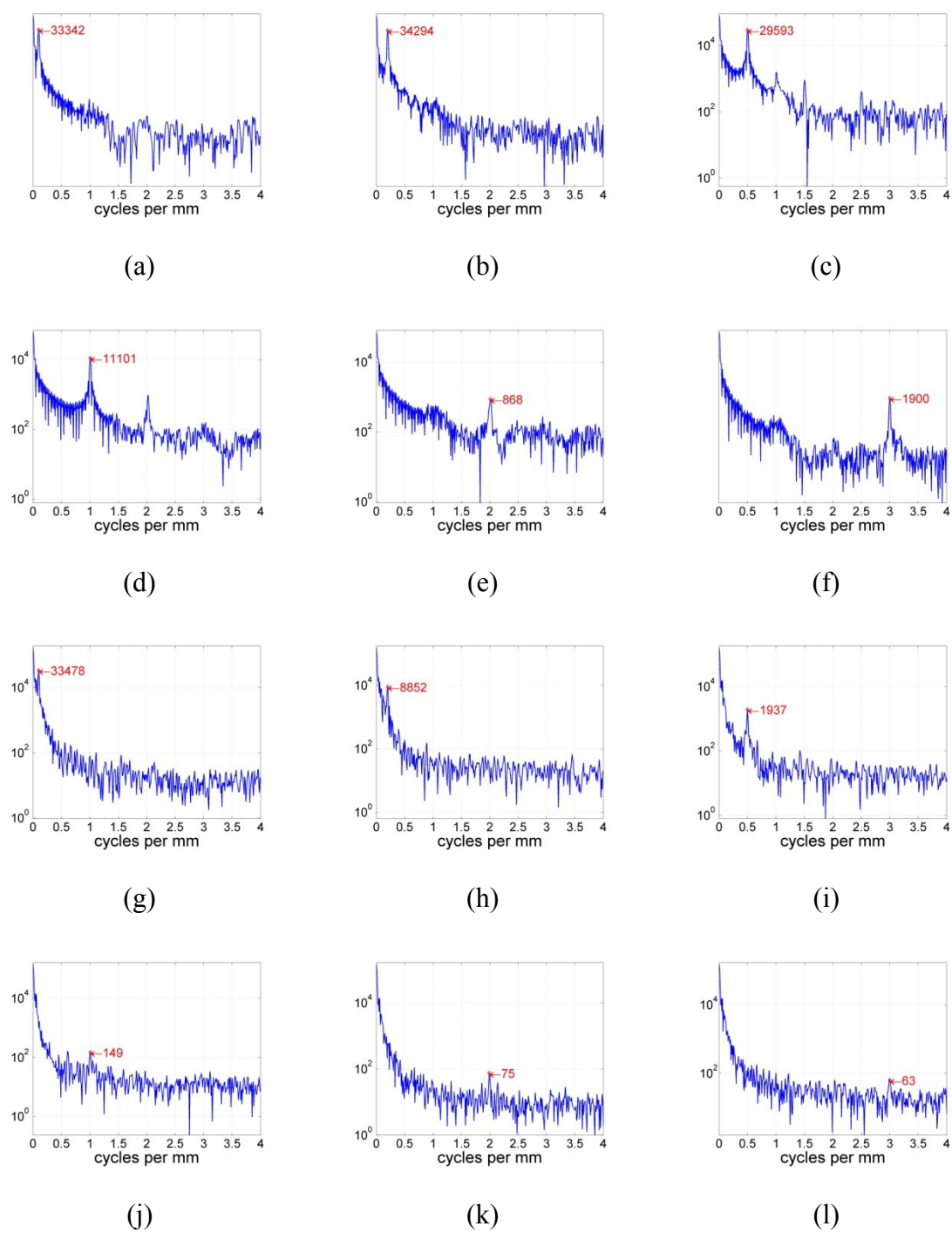
Figure 75. 1-D Flat white deconvolved dual and indirect image Fourier transforms

Appendix F. Unpainted reflector 1-D images

Figure 34, repeated here as Figure 76, shows the MTF created from 1-D experiment using the unpainted imaged reflector. The raw and deconvolved dual and indirect images as well as the Fourier transforms used to create the MTF are shown in Figure 77 through 81.
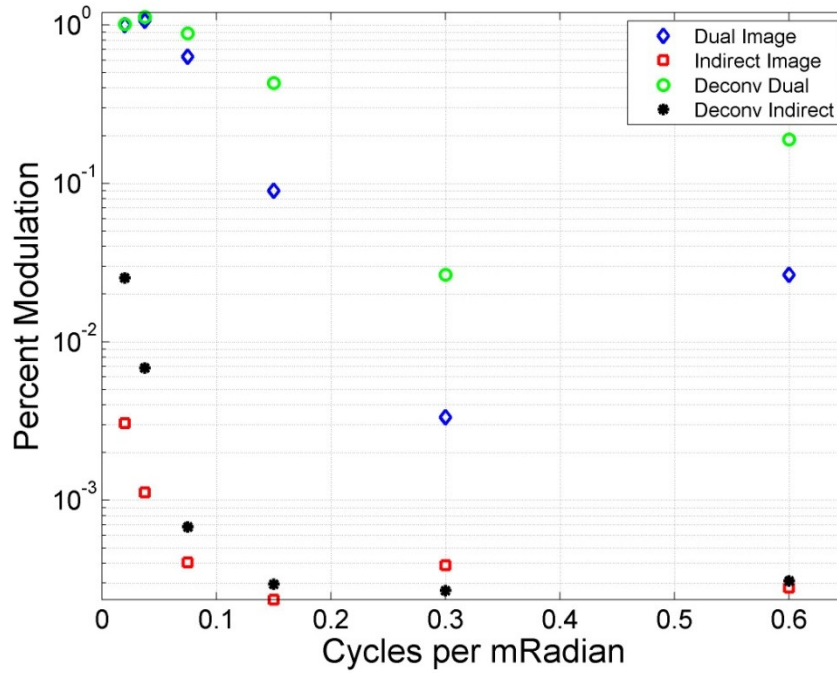
Figure 76. 1-D Unpainted MTF

Figure 77 shows the dual images created using the unpainted imaged reflector of the following slides: (a) 0.1 cycles/mm, (b) 0.2 cycles/mm, (c) 0.5 cycles./mm, (d) 1.0 cycles/mm, (e) 2.0 cycles/mm and (f) 3.0 cycle/mm. Figure 65 (g), (h) and (i) show an expanded view of (d), (e) and (f) respectively. Figure 78 shows the 1-D indirect images created using the unpainted imaged reflector of the following slides: (a) 0.1 cycles/mm, (b) 0.2 cycles/mm, (c) 0.5 cycles/mm, (d) 1.0 cycles/mm, (e) 2.0 cycles/mm and (f) 3.0

129

cycle/mm. Figure 78 (g), (h) and (i) show an expanded view of (d), (e) and (f) respectively. Figure 79 shows the deconvolved images overlaid on the raw images, (a) through (f) are the dual images while (g) through (l) are the indirect images. The individual images are as follows: (a) and (g) 0.1 cycles/mm, (b) and (h) 0.2 cycles/mm, (c) and (i) 0.5 cycles/mm, (d) and (j) expanded view of 1.0 cycles/mm, (e) and (k) expanded view of 2.0 cycles/mm, (f) and (l) expanded view of the 3.0 cycle/mm. Figure 80 (a) through (l) shows the Fourier transforms of the dual images shown in Figure 79 (a) through (l), while Figure 81(a) through (l) shows the Fourier transforms of the indirect images of Figure 79 (a) through (l).
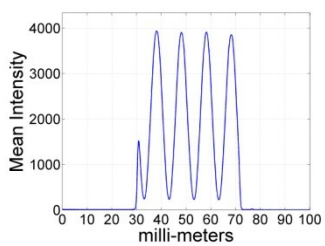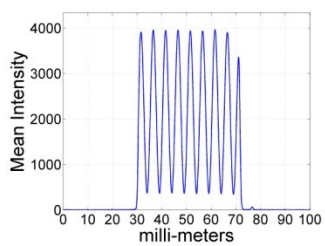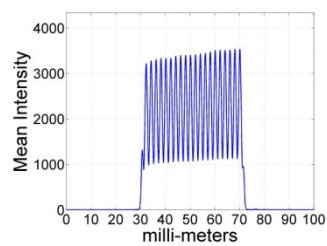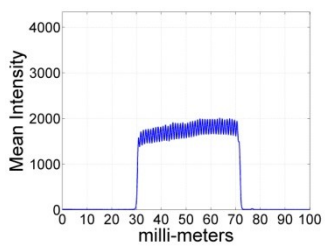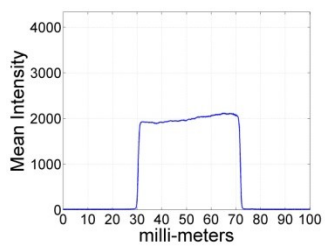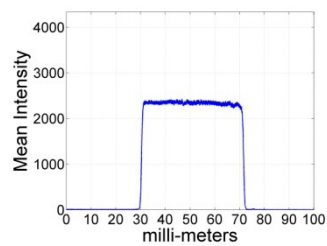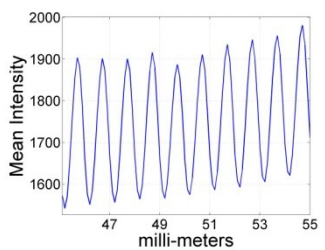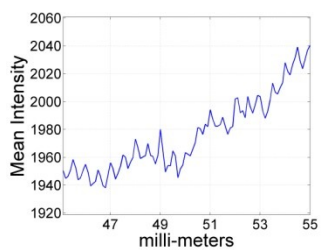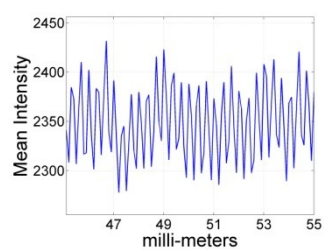
Figure 77. 1-D Unpainted dual images
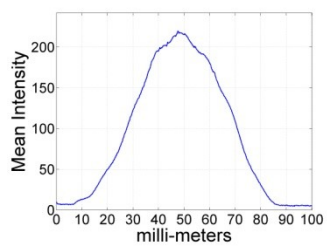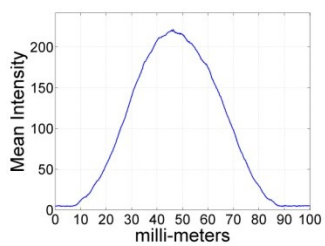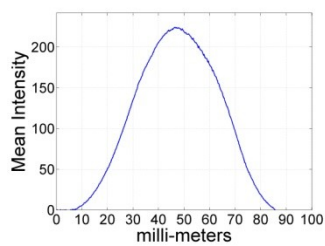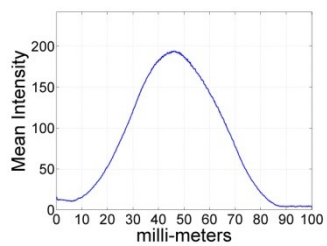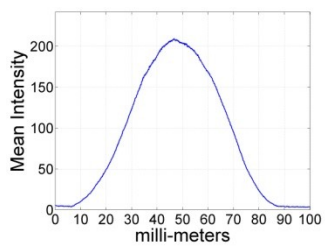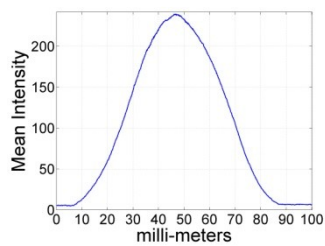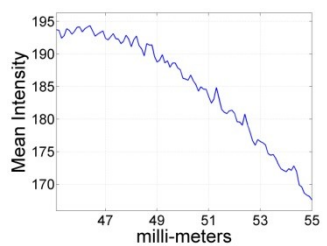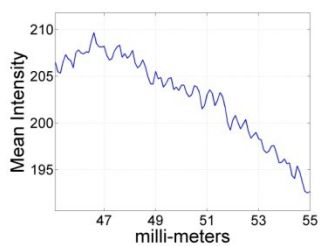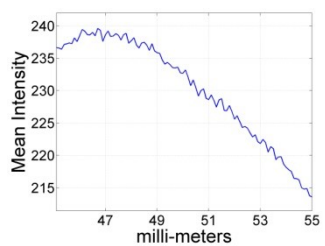
Figure 78. 1-D Unpainted indirect images

132

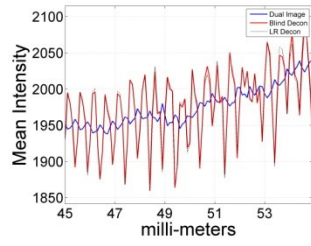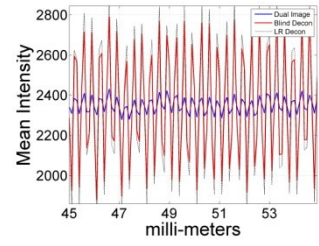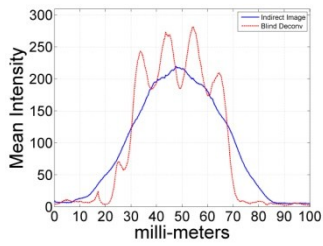(a)   (b)   (c)
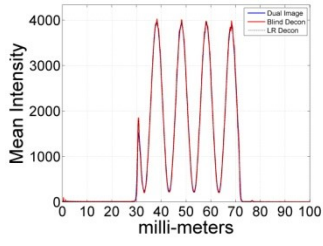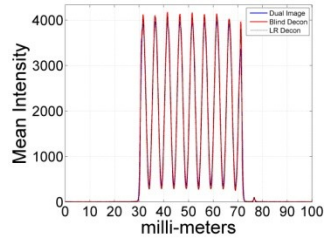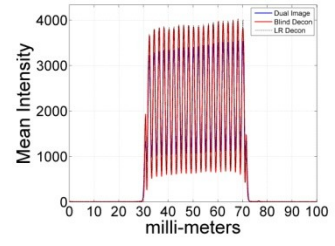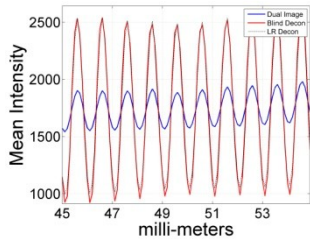
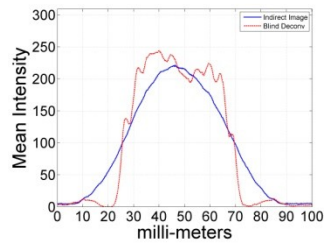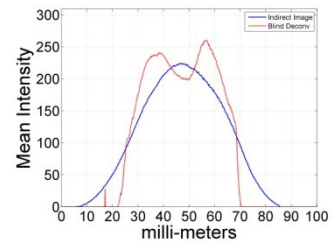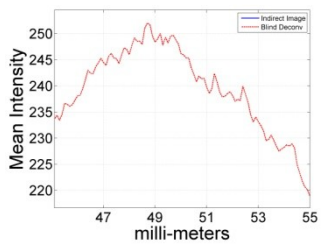(d)   (e)   (f)

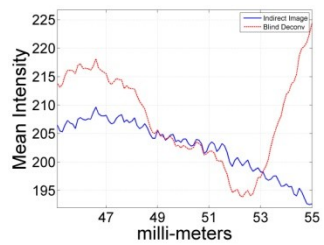(g)   (h)   (i)
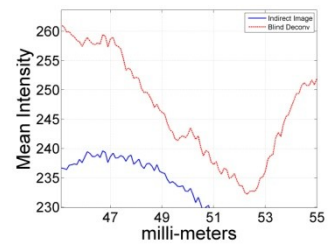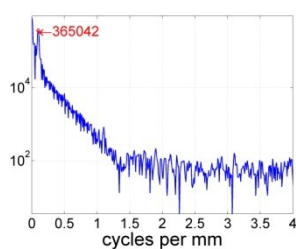
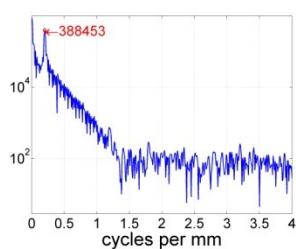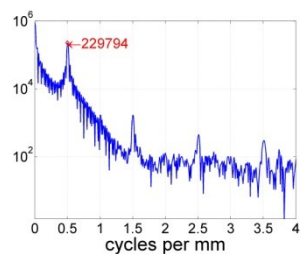(j)   (k)   (l)
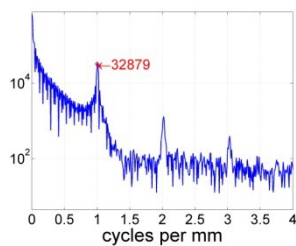
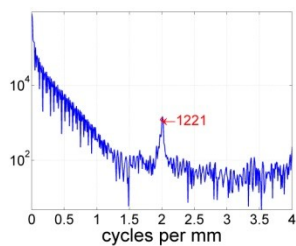**Figure 79. 1-D Unpainted dual and indirect deconvolved images**
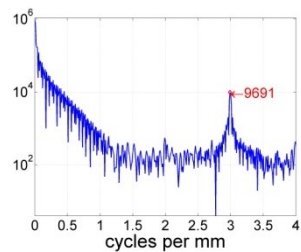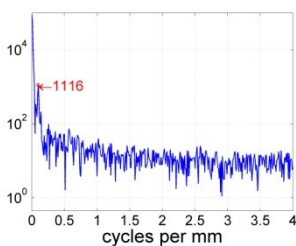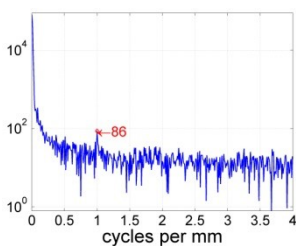
133
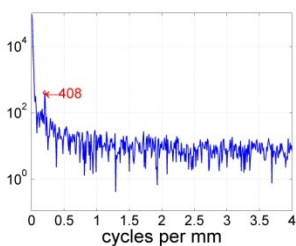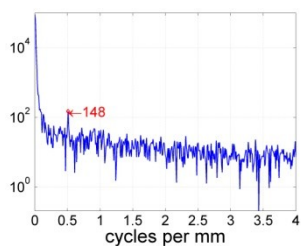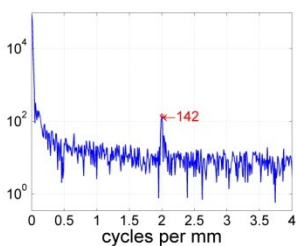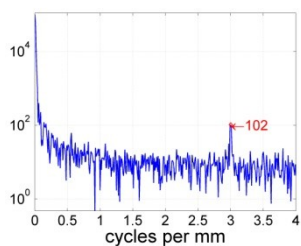
Figure 80. 1-D Unpainted dual and indirect image Fourier transforms
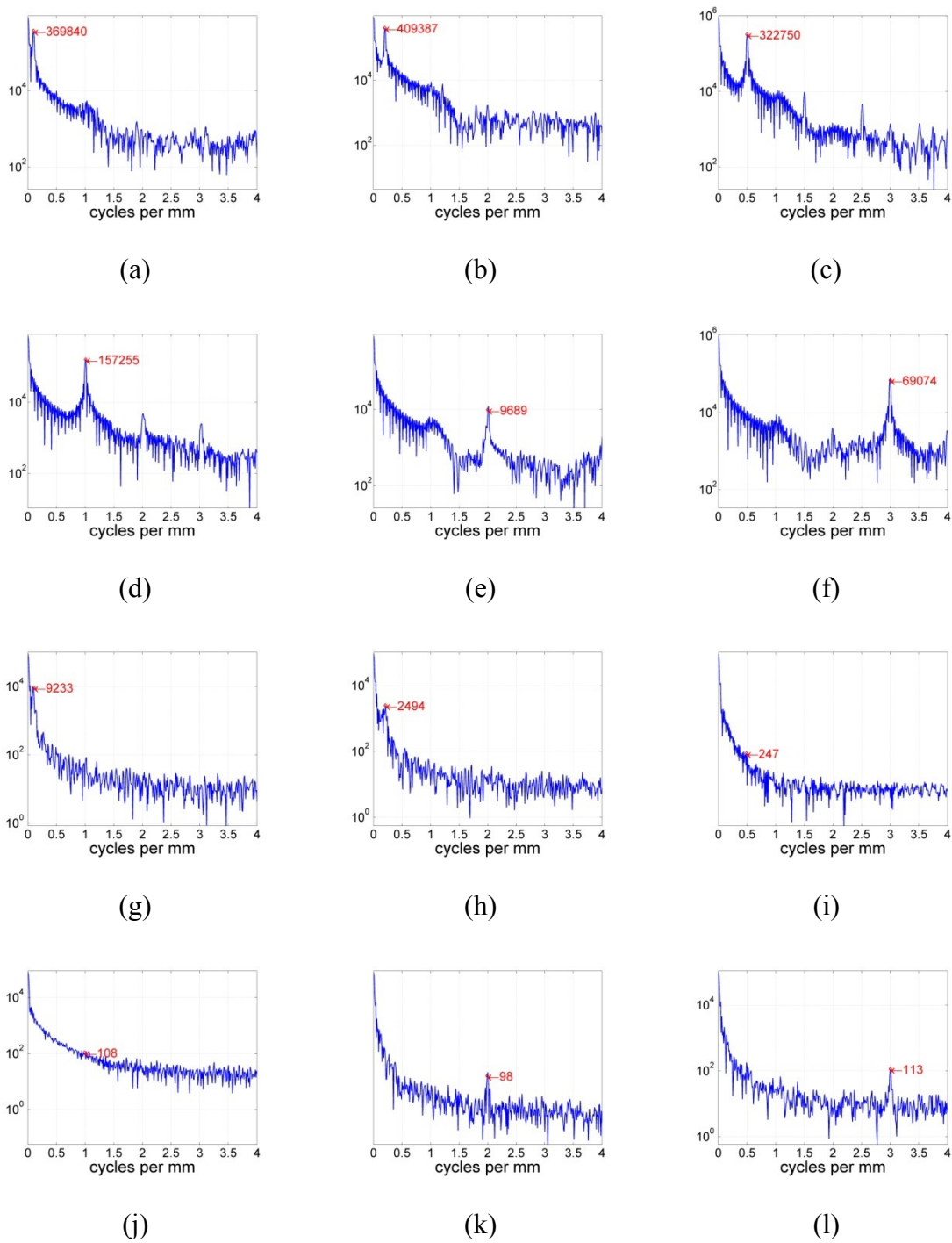
Figure 81. 1-D Unpainted deconvolved dual and indirect image Fourier transforms

135

Bibliography

Balling, B. C. (2008). *A comparative study of bi-directional reflectance distribution function of several sufacesas a mid-wave infrared diffuse reflectance standard.* Masters Thesis, AFIT.

Beard, J., & Maxwell, J. R. (1973). Technical Reorpt Number AFAL-TR-73-303.

Bickel, W. S., & Videen, G. (1991). Stokes vectors, Mueller matrices and polarized scatted light: expeimental applications to optical surfaces adn all other scatterers. SPIE Vol 1530 .

Boas, M. L. (1983). *Mathematical methods in the physical sciences.* Hoboken, NJ: Wiley & Sons.

Dereniak, E. L., & Boreman, G. D. (1996). *Infrared Detectors and Systems.* New York, NY: John Wiley & Suns.

Driggers, R. G., Cox, P., & Edwards, T. (1999). *Introduction to Infrared and Electro-Optical Systems.* Boston, MA: Artech House.

Gaskill, J. D. (1978). *Linear Systems, Fourier Transforms and Optics.* New York, NY: John Wiley & Sons.

Gonzalez, R. C., Woods, R. E., & Eddins, S. L. (2004). *Digital Image Processing using MATLAB.* Upper Saddle River, NJ: Prentice Hall.

Goodman, J. W. (2005). *Introduction to Fourier Optics.* Roberts and Company.

Hace, R. A., & Johnson, C. R. (1991). *Topix in Matrix Analysis.* New York, NY: Cambridge University Press.

Hecht, E. (2002). *Optics.* San Francisco, CA: Addison Wesley.

Hoelscher, M. G., & Marciniak, M. A. (2011). Indirect Photography - a novel approach for the remote sensing of hidden objects. *Optics Express* .

Hoelscher, M. G., & Marciniak, M. A. (2010). Restoration of scene information reflected from a non-specular surface. *SPIE 7792, 77920L* .

136

Hoffman, K., & Kunze, R. (1971). *Linear Algebra.* Upper Saddle River, NJ: Prentice Hall.

Hogban, L., Brualdi, R., Greenbaum, A., & Mathias, R. (2003). *Handbook of Linear Algebra.* Boca Raton, FL: Chapman & Hack/CRC.

Holmes, T. J. (1992). Blind deconvolution of quantum-limited incoherent imagery: maximum-likelihood approach. *J. Opt Soc. Am. A Vol 9, No. 7 ,* 1052-1061.

Lucy, L. B. (1974). An iterative technique for the rectification of observer distributions. *Astron. J. 79 ,* 745-765.

Max, B., & Emil, W. (2006). *Principles of Optics.* Cambridge, UK: University Press.

Nicodeums, F. E., Richmond, J. C., Limperis, T., Ginsberg, W., & HSIA, J. J. (1977). *Geometrical considerations adn nomenclature for reflectance.* Washington, DC: National Bureau of Standards.

Pezzaniti, J. L., Chipman, R. A., & McClain, S. C. (1994). Polarization BRDF. SPIE Vol. 2260.

Pradeep Sen, B. C. (2005). Dual Photography. *ACM SIGGRAPH ,* Conference Proceedings: 1-11.

Priest, R. G., & Meier, S. R. (2002). Polarimetrics microfacet scattering theory with applications to absorptive and reflective surfaces. *Optical Engineering , 41* (5).

Rayleigh, J., & Strutt, W. (1900). On the law of reciprocity in diffuse reflection. *Philosophical Magazine , 324-325.*

Richardson, W. H. (1972). Bayesian-based iterative method of image restoration. *J. Opt. Soc Am. 62 ,* 55-59.

Sen, P., & Shheil, D. (2009). Compressive Dual Photography. *Eurographics , 28* (2).

Sen, P., Chen, B., Bauave, G., Marschner, S. R., Horowitz, M., Levoy, M., et al. (2005). Dual Photography. (pp. Conference Proceedings: 1-11). AMC Siggraph.

Stover, J. C. (1995). *Optical Scattering.* Bellingham, Washington: SPIE Optical Engineering Press.

Sundberg, R. L., Gruninger, J., Nosek, M., Burks, J., & Fontaine, E. (1997). Quick image display (QUID) model for rapid real-time target imagery and spectral signatures. *SPIE Technologies for Synthetic Environments.*

Torrance, K. E., & Sparrow, E. M. (1967). Theory for off-specular reflection from roughedned surfaces. *J. Opt Soc Am , 57.*

Veach, E. (1998). Robust Monte Carl Methods for Light Transport. *PhD thesis, Standford University .*

von Helmholtz, H., & Southall, J. P. (1962). Helmholtz Treatise on Physiological Optics. Dover.

Wolfe, W. L., & Zissis, G. J. (1993). *The Infrared Handbook.* Washington, DC: Office of Naval Research, Department of the Navy.

REPORT DOCUMENTATION PAGE	*Form Approved* *OMB No. 074-0188*

The public reporting burden for this collection of information is estimated to average 1 hour per response, including the time for reviewing instructions, searching existing data sources, gathering and maintaining the data needed, and completing and reviewing the collection of information. Send comments regarding this burden estimate or any other aspect of the collection of information, including suggestions for reducing this burden to Department of Defense, Washington Headquarters Services, Directorate for Information Operations and Reports (0704-0188), 1215 Jefferson Davis Highway, Suite 1204, Arlington, VA 22202-4302. Respondents should be aware that notwithstanding any other provision of law, no person shall be subject to an penalty for failing to comply with a collection of information if it does not display a currently valid OMB control number.
PLEASE DO NOT RETURN YOUR FORM TO THE ABOVE ADDRESS.

1. REPORT DATE *(DD-MM-YYYY)* 24-03-2011	**2. REPORT TYPE** PhD Dissertation	**3. DATES COVERED** *(From – To)* Sept 2007 – March 2011
TITLE AND SUBTITLE Restoration of scene information reflected from non-specular media		**5a. CONTRACT NUMBER** N/A
		5b. GRANT NUMBER N/A
		5c. PROGRAM ELEMENT NUMBER N/A
6. AUTHOR(S) Hoelscher, Mark G. Lt Col, USAF		**5d. PROJECT NUMBER** N/A
		5e. TASK NUMBER N/A
		5f. WORK UNIT NUMBER N/A
7. PERFORMING ORGANIZATION NAMES(S) AND ADDRESS(S) Air Force Institute of Technology Graduate School of Engineering and Management (AFIT/ENY) 2950 Hobson Way, Building 640 WPAFB OH 45433-8865		**8. PERFORMING ORGANIZATION REPORT NUMBER** AFIT/DS/ENP/11-M03
9. SPONSORING/MONITORING AGENCY NAME(S) AND ADDRESS(ES) N/A		**10. SPONSOR/MONITOR'S ACRONYM(S)** N/A
		11. SPONSOR/MONITOR'S REPORT NUMBER(S) N/A

12. DISTRIBUTION/AVAILABILITY STATEMENT
  APPROVED FOR PUBLIC RELEASE; DISTRIBUTION UNLIMITED.

13. SUPPLEMENTARY NOTES

14. ABSTRACT

A recently published experiment called "dual photography" exploits Helmholtz reciprocity by illuminating a scene with a pixilated light source and imaging other parts of that scene with a camera so that light transport between every pair of source-to-camera pixels is measured. The positions of the source and camera are then computationally interchanged to generate a "dual image" of the scene from the viewpoint of the source illuminated from the position of the camera. Although information from parts of the scene normally hidden from the camera are made available, this technique is rather contrived and therefore limited in practical applications since it requires access to the path from the source to the scene for the pixilated illumination.

By radiometrically modeling the experiment described above and expanding it to the concept of *indirect photography*, it has been shown theoretically, by simulation and through experimentation that information in parts of the scene not directly visible to either the camera or the controlling light source can be recovered. To that end, the camera and light source (now a laser) have been collocated. The laser is reflected from a visible surface in the scene onto hidden surfaces in the scene and the camera images collect how the light is reflected from the hidden surfaces back to the visible surface. The camera images are then used to reconstruct information from the hidden surfaces in the scene. This document discusses the theory of indirect photography, describes the simulation and experiment and used to verify the theory and describes techniques used to improve the image quality, as measured by modified modulation transfer function.

15. SUBJECT TERMS
Bidirectional Reflectance Distribution Function, BRDF, Remote Sensing

16. SECURITY CLASSIFICATION OF:			**17. LIMITATION OF ABSTRACT**	**18. NUMBER OF PAGES**	**19a. NAME OF RESPONSIBLE PERSON** Michael A. Marciniak ADVISOR
a. REPORT	**b. ABSTRACT**	**c. THIS PAGE**	UU	156	**19b. TELEPHONE NUMBER** *(Include area code)* (937) 255-6565, ext 7510 (michael.marciniak@afit.edu)
U	U	U			

Standard Form 298 (Rev. 8-98)
Prescribed by ANSI Std. Z39-18